University of Alberta

Conversion of Propane to Propylene in a Proton-Conducting Fuel Cell

by

Yu Feng

A thesis submitted to the Faculty of Graduate Studies and Research
in partial fulfillment of the requirements for the degree of **Doctor of Philosophy** in
Chemical Engineering

Department of Chemical & Materials Engineering

Edmonton, Alberta
Spring 2008

Library and Archives Canada

Published Heritage Branch

395 Wellington Street
Ottawa ON K1A 0N4
Canada

Bibliothèque et Archives Canada

Direction du Patrimoine de l'édition

395, rue Wellington
Ottawa ON K1A 0N4
Canada

Your file Votre référence
ISBN: 978-0-494-45425-1
Our file Notre référence
ISBN: 978-0-494-45425-1

NOTICE:
The author has granted a non-exclusive license allowing Library and Archives Canada to reproduce, publish, archive, preserve, conserve, communicate to the public by telecommunication or on the Internet, loan, distribute and sell theses worldwide, for commercial or non-commercial purposes, in microform, paper, electronic and/or any other formats.

The author retains copyright ownership and moral rights in this thesis. Neither the thesis nor substantial extracts from it may be printed or otherwise reproduced without the author's permission.

AVIS:
L'auteur a accordé une licence non exclusive permettant à la Bibliothèque et Archives Canada de reproduire, publier, archiver, sauvegarder, conserver, transmettre au public par télécommunication ou par l'Internet, prêter, distribuer et vendre des thèses partout dans le monde, à des fins commerciales ou autres, sur support microforme, papier, électronique et/ou autres formats.

L'auteur conserve la propriété du droit d'auteur et des droits moraux qui protège cette thèse. Ni la thèse ni des extraits substantiels de celle-ci ne doivent être imprimés ou autrement reproduits sans son autorisation.

In compliance with the Canadian Privacy Act some supporting forms may have been removed from this thesis.

While these forms may be included in the document page count, their removal does not represent any loss of content from the thesis.

Conformément à la loi canadienne sur la protection de la vie privée, quelques formulaires secondaires ont été enlevés de cette thèse.

Bien que ces formulaires aient inclus dans la pagination, il n'y aura aucun contenu manquant.

Canada

ABSTRACT

Using proton-conducting fuel cells for propane dehydrogenation to produce propylene is a novel process having many interesting characteristics, which combines the continuous chemical process to produce value-added propylene with electrical power generation. Although a lot of efforts have been made to demonstrate this process experimentally, no success has been achieved because of challenges in finding suitable proton-conducting electrolytes and compatible electrodes operating at intermediate temperatures (<800°C). In this thesis, the feasibility of conversion of propane to propylene in a proton-conducting fuel cell was studied by developing suitable fuel cell components.

$LiNaSO_4$ and the perovskite type of oxide, Y-doped $BaCeO_3$, was investigated for use as proton conducting electrolyte in the fuel cells. Thermodynamic analysis and experimental results indicated $LiNaSO_4$ was not stable in the fuel cell for propane dehydrogenation and the proton conductivity of $LiNaSO_4$ only accounts for 5-10% of total ion conductivity. Y-doped $BaCeO_3$ presents high proton conductivity and good chemical stability over 120 h tests coupled with suitable fuel cell set-up design. Thus, the feasibility of conversion of propane to propylene in a fuel cell based on this perovskite oxide with platinum as anode and cathode catalysts was investigated. The feasibility was proven with high product selectivity to propylene and good fuel cell performances. It was also showed that the electrochemical reaction of propane dehydrogenation was in competition with other side reactions caused by the gas species (H_2, C_2H_6, C_2H_4 etc.), which were the products of non-electrochemical reactions (e.g. thermal cracking) in the

anode chamber. The hydrogen oxidation reaction was a predominant side electrochemical reaction.

Chromium (III) oxide synthesized by sol-gel method showed high activity for electrochemical propane dehydrogenation, and the maximum power density of about 110 mW/cm^2 was achieved at 700°C as well as propylene selectivity up to 95%.

Carbon deposition during the process of propane dehydrogenation in the fuel cell was a problem, as the carbon poisoned the anode catalysts leading to deactivation of anode catalysts and deterioration of the product distribution. Compared to open circuit conditions, carbon deposition can be dramatically reduced with a local electrical field on the anode catalyst under the current flow conditions.

ACKNOWLEDGMENTS

I wish to express my sincere and deep thanks to my supervisors, Prof. Jingli Luo and Prof. Karl T. Chuang, for their guidance, help, encouragement and support during the four-year period of my Ph.D. program.

I am grateful to Prof. Krishnaswamy Nandakumar (supervisor committee member), Prof. Biao Huang, Prof. Andre McDonald (Mechanical Engineering) and Prof. Gu Xu (external examiner from McMaster University), for being the members of my dissertation committee and spending their invaluable time reviewing this work.

Special thanks to my past and present group mates at Fuel Cell Research Group. I enjoyed and benefited greatly from my daily and dynamic interaction with all of them. In particular, I thank Mrs. Weizhu An, Dr. Shouyan Wang, Dr. Juri Melnik and Dr. Li Zhong for their assistance and stimulating discussion during the early stage of my dissertation.

I would also like to thank Andrew Stewart Memorial Graduate Prize, DB Robinson Graduate Scholarship in Chemical and Materials Engineering, Captain Thomas Farrell Greenhalgh Memorial Graduate Scholarship and J Gordon Kaplan Graduate Student Award at the University of Alberta.

Especially, I would like to express my deepest gratitude to my parents. With their deeply love and endless support over my advancement path, I have been able to accomplish what may once have been envisioned as just a dream. Last but certainly not least, a deep gratitude to my dear wife, Haiyan Yin, for her love, understanding and

support, both in the research and at home, through my four-year of Ph.D. life.

TABLE OF CONTENTS

CHAPTER 1 INTRODUCTION 1

1.1 Introduction 1

1.2 Background of propylene production 4

1.2.1 Steam pyrolysis of hydrocarbons 4

1.2.2 Fluidized catalytic cracking 6

1.2.3 Propane dehydrogenation 7

1.2.3.1 Commercial dehydrogenation of propane 7

1.2.3.2 Oxidative dehydrogenation of propane 12

1.3 Objectives 13

1.4 Organization of thesis 14

References 17

CHAPTER 2 INVESTIGATION OF $LiNaSO_4$ AS PROTON-CONDUCTING ELECTROLYTE IN FUEL CELLS 22

2.1 Introduction 22

2.2 Stability of $LiNaSO_4$ in hydrogen 24

2.2.1 Thermodynamic analysis 24

2.2.2 Experimental 27

2.2.2.1 Materials 27

2.2.2.2 Fuel cell system fabrication 28

2.2.2.3 Fuel cell tests 29

2.2.3 Results and discussion 30

2.2.3.1 Materials 30

2.2.3.2 Fuel cell performance 31

2.2.3.3 Chemical stability of $LiNaSO_4$ in hydrogen 36

2.3 Proton conductivity of $LiNaSO_4$ under fuel cell conditions 38

2.3.1 Principles of the method 38

2.3.2 Experimental 40

2.3.2.1 Sandwich disk preparation 40

2.3.2.2 Chemical and mechanical compatibility 43

2.3.2.3 Conductivity measurements 44

2.3.3 Results and discussion 45

2.4 Conclusions 51

References 52

CHAPTER 3 CONVERSION OF PROPANE TO PROPYLENE IN A PROTON-CONDUCTING FUEL CELL USING Y-DOPED $BaCeO_3$ AS ELECTROLYTE 57

3.1 Introduction 57

3.2 Experimental 59

3.2.1 Electrolyte 59

3.2.2 Electrodes 60

3.2.3 Fuel cell system fabrication 60

3.2.4 Electrical measurements and gas analysis 61

3.3 Results and discussion 64

3.3.1 BCY15 Electrolyte 64
3.3.1.1 Properties 64
3.3.1.2 Stability tests of the electrolyte, and analysis 66
3.3.1.3 New fuel cell set-up designs 71
3.3.1.4 Stability of Y-doped $BaCeO_3$ electrolyte using the revised fuel cell design 75
3.3.2 Analysis of anode outlet gas 77
3.3.2.1 Open circuit conditions 77
3.3.2.2 Discharging fuel cells 79
3.3.3 Fuel cell performance 82
3.4 Conclusions 84
References 85
CHAPTER 4 THE PROCESS OF PROPANE DEHYDROGENATION IN A PROTON-CONDUCTING FUEL CELL 91
4.1 Introduction 91
4.2 Experimental 92
4.2.1 Materials 92
4.2.2 Fuel cell system design 92
4.2.3 Electrical measurements and gas analysis 93
4.3 Results and discussion 93
4.3.1 Non-electrochemical reactions in the fuel cell system 93
4.3.2 Open circuit voltage 98
4.3.3 Fuel cell performances 106

4.3.4 Gas products analysis 110

4.4 Conclusions 116

References 116

CHAPTER 5 Cr_2O_3 BASED ANODE CATALYSTS FOR PROPANE DEHYDROGENATION IN A PROTON-CONDUCTING FUEL CELL 120

5.1 Introduction 120

5.2 Experimental 122

5.2.1 Synthesis of chromium (III) oxide based anode catalyst 122

5.2.2 Fuel cell system 123

5.2.3 Characterization of anode catalysts, fuel cell performance and gas products 123

5.3 Results and discussion 124

5.3.1 Materials 124

5.3.2 Fuel cell performances 126

5.3.3 Gas products analysis 132

5.3.4 Stability test of chromium (III) oxide based anode catalyst 134

5.4 Conclusions 136

References 136

CHAPTER 6 CARBON DEPOSITION DURING PROPANE DEHYDROGENATION IN A FUEL CELL 141

6.1 Introduction 141

6.2 Experimental 142

6.2.1 Fuel cell system 142
6.2.2 Electrolyte 142
6.2.3 Electrodes 143
6.2.4 Characterization of anode catalysts 143
6.3 Results and discussion 144
6.3.1 Carbon deposition under open circuit conditions 144
6.3.2 Carbon deposition under fuel cell operation conditions 150
6.4 Conclusions 153
References 154
CHAPTER 7 SUMMARY 157
7.1 General conclusions 157
7.2 Claim for original research 160
7.3 Prospect of future work 161
APPENDIX-A 163
APPENDIX-B 165

LIST OF TABLES

Table 1-1 Reaction equilibrium constants for industrial propane dehydrogenation and propane dehydrogenation in fuel cells 2

Table 1-2 Free radicals mechanism of molecular reactions of hydrocarbon pyrolysis... 5

Table 1-3 Commercial dehydrogenation processes 8

Table 2-1 Conductivities of $LiNaSO_4$ and BCY15 at 600-680°C. 49

Table 2-2 Comparison of performances of fuel cells with $LiNaSO_4$ and BCY as electrolytes. 50

Table 3-1 Calibration with a standard gas 63

Table 4-1 The calculated EMF values from Nernst Equation for reactions (4-21), (4-23) and (4-24), as well as partial pressures of the gas species and standard potential (HSC Chemistry Software, Version 5.1, Outokunpu Research).. 100

Table 4-2 Comparison of measured OCV values of $C_3H_8 - O_2$ fuel cell and the calculated EMFs for different possible electrochemical reactions in $C_3H_8 - O_2$ fuel cell at different temperatures with propane flow rate of 100 mL/min 105

LIST OF FIGURES

Figure 1-1 Schematic of propane dehydrogenation in a proton conducting fuel cell....3

Figure 1-2 Schematic of Oleflex process for propane dehydrogenation (Adapted from ref.29).....9

Figure 1-3 Schematic of Catofin process for propane dehydrogenation (Adapted from ref.32).....11

Figure 2-1 Gibbs free energy changes of possible reactions for Li_2SO_4 at different temperatures.....26

Figure 2-2 Gibbs free energy changes of possible reactions for Na_2SO_4 at different temperatures.....27

Figure 2-3 Schematic of fuel cell set-up using $LiNaSO_4$ as electrolyte 29

Figure 2-4 Phase diagram of binary system of Li_2SO_4-Na_2SO_4 (Reprinted with permission of The American Ceramic Society).....31

Figure 2-5 I-V curves of H_2-O_2 fuel cell with $LiNaSO_4$–Al_2O_3 at different temperatures.....33

Figure 2-6 OCV-time curve of the cell with electrolyte of $LiNaSO_4$–Al_2O_3 and anode feed of nitrogen (before switch to hydrogen) at 600°C 33

Figure 2-7 OCV-time curve of H_2-O_2 fuel cell with $LiNaSO_4$–Al_2O_3 at 600°C 34

Figure 2-8 Impedance spectra of H_2-O_2 fuel cell with $LiNaSO_4$–Al_2O_3 at 600°C and different time under open circuit conditions.....35

Figure 2-9 XRD profiles of $LiNaSO_4$ after heated in H_2 at 600°C for 10 h 37

Figure 2-10 XRD profiles of $LiNaSO_4$ without processing with H_2 37

Figure 2-11 Configuration of sandwich disk to measure proton conductivity of $LiNaSO_4$ 40

Figure 2-12 Sandwich disk sintered at 800°C. (a) Perspective view of the sandwich disk. (b) Cross-section of the sandwich disk 42

Figure 2-13 XRD profiles of the mixture of BCY and $LiNaSO_4$ powder before and after sintered at 800°C for 8 h 43

Figure 2-14 Microstructure of cross section of $LiNaSO_4$/BCY layers interface 44

Figure 2-15 Conductivities measurement for the cell with electrolyte of sandwich disk at 600°C using current interruption method. (a) Interruption of current. (b) Response of the voltage. 47

Figure 2-16 Impedance spectra for the cells with electrolyte of BCY disk at 600°C under open circuit conditions. 48

Figure 2-17 Equivalent circuit for the sandwich disk in fuel cells. 49

Figure 3-1 Illustration of proton migration "hopping" in a perovskite type oxide 59

Figure 3-2 Schematic of high temperature fuel cell set-up with ceramic sealant (Aremco 503). 61

Figure 3-3 XRD of $BaCe_{0.85}Y_{0.15}O_{3-\alpha}$ powder after sintering at 1600°C 65

Figure 3-4 SEM of surface of BCY15 electrolyte. 65

Figure 3-5 Temperature dependence of conductivity in BCY15 in C_3H_8-O_2 fuel cell.....66

Figure 3-6 Conductivity as a function of exposure time under open circuit conditions at 650°C with propane flow rate 80 mL/min. 67

Figure 3-7 Microstructures of anode side surface of Y-doped $BaCeO_3$ electrolyte after 120 h test. 68

Figure 3-8 EDX profiles of anode side surface of Y-doped $BaCeO_3$ electrolyte after 120 h test (corresponding to Figure 5-7). (a) Point 1; (b) Point 2). 69

Figure 3-9 XRD profiles of electrolyte BCY15 disk before and after test in propane for 120 h. 70

Figure 3-10 Microstructures of ceramic sealant (Aremco 503) after sintering at 650°C in the fuel cell.....71

Figure 3-11 Microstructure of glass sealant after sintering at 650°C in the fuel cell. ...72

Figure 3-12 Schematic diagram of revised high temperature fuel cell set-up with vertical design 73

Figure 3-13 Schematic of revised horizontal high temperature fuel cell set-up.....74

Figure 3-14 AC impedance spectra of C_3H_8–O_2 fuel cell based on Y-doped $BaCeO_3$ electrolyte.....76

Figure 3-15 Microstructure of anode side surface of Y-doped $BaCeO_3$ electrolyte after 120 h test in revised fuel cell design. 76

Figure 3-16 Propane conversion and selectivities to C_3H_6 and $CH_4 + C_2H_4$ at different operating temperatures under open circuit conditions (propane flow rate: 20 mL/min) 78

Figure 3-17 Propane conversion and selectivities to C_3H_6 and $CH_4 + C_2H_4$ at different propane flow rates under open circuit conditions (600°C). 79

Figure 3-18 Propane conversion and selectivities of C_3H_6 and $CH_4 + C_2H_4$ at different discharging current density (600°C, propane flow rate: 10 mL/min and effective electrode area: 0.7 cm^2) 80

Figure 3-19 Propylene yield by electro-catalytic dehydrogenation at different discharging current density (600°C, propane flow rate: 10 mL/min and effective electrode area: 0.7 cm^2) 82

Figure 3-20 Discharge properties of C_3H_8-O_2 fuel cell using BCY15 electrolyte at 600°C and 650°C with propane flow rate of 10 mL/min (thickness of electrolyte: 0.7 mm). 83

Figure 3-21 Discharge properties of C_3H_8-O_2 fuel cell using BCY15 electrolyte at 600°C with propane flow rate of 10 and 30 mL/min (thickness of electrolyte: 0.7 mm). 84

Figure 4-1 Reaction equilibrium constants of the non-electrochemical reactions in $C_3H_8 - O_2$ fuel cell at different temperatures. 97

Figure 4-2 Mechanistic of propane reaction on the platinum catalyst 97

Figure 4-3 Reaction equilibrium constant for carbon formation reaction (4-6) from hydrocarbon species in the gas products 98

Figure 4-4 Open circuit voltage of H_2–O_2 fuel cell using Y-doped $BaCeO_3$ as electrolyte with pure hydrogen as anode feed and water saturated oxygen as cathode gas at 650°C.....102

Figure 4-5 Fuel cell performances using pure propane (flow rate: 100 mL/min) and 3.7% hydrogen (balance with argon) as anode feed respectively, with the same electrolyte of Y-doped $BaCeO_3$ and electrodes of Pt at 650°C. 107

Figure 4-6 Maximal power density at different propane flow rate obtained from C_3H_8–O_2 fuel cell at 650°C. 108

Figure 4-7 Maximal power density at different propane flow rate obtained from C_3H_8–O_2 fuel cell at 700°C. 109

Figure 4-8 Propylene and hydrogen concentration changes in anode chamber effluent at 650°C during discharging C_3H_8–O_2 fuel cell with Y-doped $BaCeO_3$ as electrolyte and platinum as electrodes at propane flow rate 100 mL/min.....111

Figure 4-9 Propylene selectivity at different discharging current of C_3H_8–O_2 fuel cell at 650°C.....112

Figure 4-10 Propylene and hydrogen concentration changes in anode chamber effluent at 700°C during discharging C_3H_8–O_2 fuel cell with Y-doped $BaCeO_3$ as electrolyte and platinum as electrodes at propane flow rate 100 mL/min.....114

Figure 4-11 Propylene selectivity at different discharging current of C_3H_8–O_2 fuel cell at 700°C.....115

Figure 4-12 Schematic of proposed electrochemistry reactions utilizing propane (Adapted from ref.3). 115

Figure 5-1 Catalytic mechanism for alkane dehydrogenation over Cr_2O_3/Al_2O_3 catalysts. 121

Figure 5-2 Microstructure of synthesized chromium oxide powder. 125

Figure 5-3 SEM micrograph of cross section of a BCY15/Cr_2O_3 anode catalyst interface 125

Figure 5-4 XRD profiles of the anode Cr_2O_3+Ag before and after test in fuel cell at 700°C for 24 h. 126

Figure 5-5 Impedance spectra of C_3H_8-O_2 fuel cell with the anode catalyst Cr_2O_3+Ag. 128

Figure 5-6 Impedance spectra of C_3H_8-O_2 fuel cell with the anode catalyst Cr_2O_3+Fe. 128

Figure 5-7 Fuel cell performances with the anode catalyst Cr_2O_3+Ag at propane flow rate of 100 mL/min. 130

Figure 5-8 Fuel cell performances with the anode catalyst Cr_2O_3+Fe at propane flow rate of 100 mL/min. 131

Figure 5-9 Fuel cell performances with the anode catalyst Cr_2O_3+Fe at different propane flow rates (700°C). 132

Figure 5-10 Propylene selectivity obtained from electrochemical reaction process using the Cr_2O_3 based anode catalysts (700°C; propane flow rate: 100 mL/min). 133

Figure 5-11 Hydrogen yield obtained using the Cr_2O_3 based anode catalysts under current flow conditions (700°C; propane flow rate: 100 mL/min). 134

Figure 5-12 Influence of carbon deposition on fuel cell performance using Cr_2O_3+Fe with time on stream (700°C; propane flow rate: 100 mL/min).....135

Figure 5-13 Binding energy peak of C1s in the anode Cr_2O_3+Ag after 24 h fuel cell test. 135

Figure 6-1 Different reaction zones in the anode chamber of fuel cell under open circuit conditions.....145

Figure 6-2 Carbon selectivity from thermal cracking of propane in the fuel cell chamber.....146

Figure 6-3 Comparison of binding energy peak of C1s for different catalysts after 10 h fuel cell operation. 148

Figure 6-4 Microstructure of commercial platinum paste (Heraeus CL11-5100).....149

Figure 6-5 Microstructure of synthesized platinum anode catalyst supported on silver. 149

Figure 6-6 Comparison of binding energy peaks for C1s of carbon deposited on catalysts used under open circuit condition and at discharging current of 50 mA during 10 h fuel cell tests. 152

Figure 6-7 EDX analyses comparing carbon deposition on anode catalyst Cr_2O_3+Ag under open circuit condition and at a current of 50 mA during 10 h fuel cell tests.....152

Figure 6-8 Propane conversion and selectivities of carbon and propylene as a function of current density (600°C, propane flow rate: 50 mL/min). 153

CHAPTER 1

INTRODUCTION

1.1 Introduction

Propylene is a major industrial chemical used as a feedstock in the production of polypropylene, acrolein, propylene oxide, glycerine, isopropanol, refinery feed stock to improve the octane rating of gasoline [1,2,3,4,5,6] and other chemicals. Propane dehydrogenation to produce propylene is an important industrial process because propylene is economically more essential than propane. Currently there are four different commercial technologies that can be licensed for propane dehydrogenation [7,8,9,10,11,12]. These routes differ primarily in the types of catalyst, the reactor designs, and the methods used to increase the conversion, but they involve same reaction:

$$C_3H_8 \rightarrow C_3H_6 + H_2 \qquad \Delta H_f^\circ = 103.8 kJ \cdot mol^{-1} \qquad (1\text{-}1)$$

Because this reaction is equilibrium-limited (Table 1-1) and higher temperatures are usually needed [10,11,12,13]. Unfortunately, at these temperatures hydrocarbon cracking and coke formation are also favored.

Table 1-1. Reaction equilibrium constants for industrial propane dehydrogenation and propane dehydrogenation in fuel cells

Temperature / °C	Reaction equilibrium constant for industrial propane dehydrogenation $C_3H_8 \rightarrow C_3H_6 + H_2$	Reaction equilibrium constant for propane dehydrogenation in fuel cells $C_3H_8 + \frac{1}{2}O_2 \rightarrow C_3H_6 + H_2O$
100	1.94E-11	6.43E+20
200	1.04E-07	2.23E+17
300	2.93E-05	1.26E+15
400	1.59E-03	3.31E+13
500	3.15E-02	2.24E+12
600	3.18E-01	2.80E+11
700	2.00E+00	5.33E+10
800	8.98E+00	1.38E+10
900	3.11E+01	4.43E+09
1000	8.83E+01	1.70E+09

(The data in this Table was calculated from HSC Chemistry Software, Version 5.1, Outokunpu Research)

A novel method for producing propylene is electro-catalytic dehydrogenation of propane in proton conducting fuel cells. Studies have shown that dehydrogenation of propane to propylene occurs through a dissociative chemisorption process on catalyst surface [13,14]. So in principle, use of fuel cells overcomes equilibrium limitations as hydrogen atoms from dehydrogenation chemisorb at the catalyst surface, and are then rapidly conducted through the proton conducting electrolytes in proton form to the cathode side, where they recombine with oxygen and electrons to produce water (Figure 1-1).

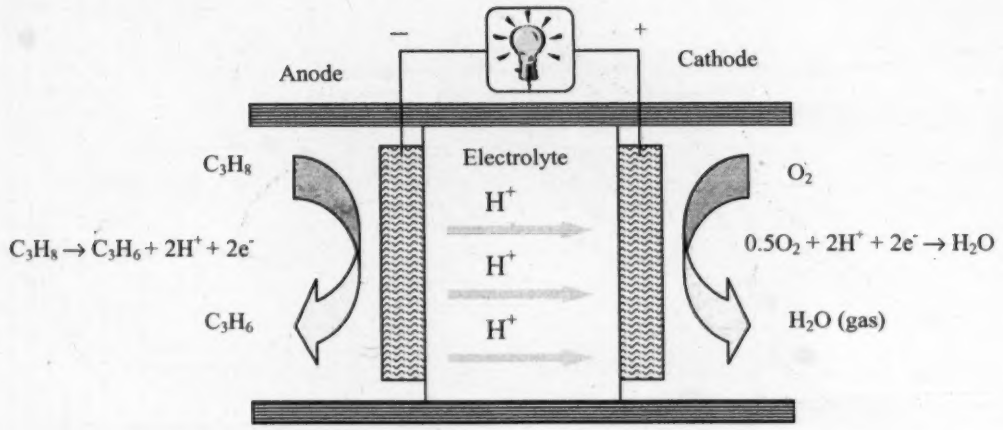

Figure 1-1. Schematic of propane dehydrogenation in a proton conducting fuel cell.

The proposed transport mechanism ensures the continuous production of propylene from propane, and the reaction of oxidative dehydrogenation of propane in the electrochemical system is not equilibrium limited (Table 1-1). Further, proton-conducting fuel cells for propane dehydrogenation separate the proton removal and oxidation steps into separate compartments, thus enabling high selectivity for conversion of propane feed to propylene as a valuable product, as no oxygen is available for further reactions of the product at the anode (Figure 1-1). This proton-conducting fuel cell process combines the continuous chemical process to produce value-added propylene with electrical power generation, and thus has the unique advantage of obtaining value-added product propylene and electricity power simultaneously. In addition, compared to hydrocarbon conversion in oxide ion conducting fuel cells [9,15,16,17,18], there is no emission of greenhouse gas (CO_2) or other pollutant gases.

Although some researchers have mentioned the idea of dehydrogenation of paraffin to olefin in a fuel cell [19,20,21], very little work was done to develop the process, especially for dehydrogenation of propane. The Fuel Cells Group at the University of Alberta is developing fuel cells for highly selective dehydrogenation of propane. Early modes that used H_3PO_4 doped polybenzimidazole (PBI) polymer as proton conductor in C_3H_8-O_2 fuel cells operating at 200-250°C showed that formation of very stable intermediate species on the surface of noble metal catalysts blocks propylene production, and very small and unsustainable current flow was obtained [14]. The results also indicated that high temperature fuel cells are more suitable for generating larger current flow and producing propylene. So, it was necessary to investigate propane dehydrogenation in a proton-conducting fuel cell that can be operated at relatively high temperatures.

1.2 Background of Propylene Production

Generally there are three major processes for the manufacture of propylene. They are steam pyrolysis (cracking) of hydrocarbons (~70%), fluidized catalytic cracking (28%), and dehydrogenation of propane (2%) [22].

1.2.1 Steam pyrolysis of hydrocarbons

In the steam cracking process, a mixture of hydrocarbons and steam is first preheated to 870 K in the convective section of a pyrolysis furnace, and then further heated in the radiant section of furnace to as high as 1170 K. The presence of steam reduces the products hydrocarbon partial pressure in the reactor and, thereby shifts the equilibrium to enhance the hydrocarbon conversion. An additional advantage of steam is

that it suppresses carbon formation [7]. The cracking process yields propylene and a large variety of by-products, ranging from mainly ethylene to hydrogen and fuel oil. The proportion of these components in the furnace effluent depends on the feedstock, but the constituents in the effluent are almost the same for all hydrocarbon feedstocks [9].

The hydrocarbon mixture undergoes reactions involving free radicals and these mechanisms have been generalized to include the molecular reactions shown in Table 1-2 [23]. The total number of reactions depends on the number of constituents present in the hydrocarbon feedstock. As many as 2000 reactions can occur simultaneously.

Table 1-2. Free radical mechanism of molecular reactions of hydrocarbon pyrolysis (Adapted from ref. 23).

Chain initiation reactions	$R-R' \rightarrow R^{\bullet} + R^{\bullet}$
Hydrogen-abstraction reactions	$R^{\bullet} + R'H \rightarrow R'^{\bullet} + RH$
Radical-decomposition reactions	$R^{\bullet} \rightarrow R'^{\bullet} + RH$
Radical-addition reactions to unsaturated molecules	$R'^{\bullet} + RH \rightarrow R''^{\bullet}$
Chain-termination reactions	$R'^{\bullet} + R^{\bullet} \rightarrow R-R'$
Molecular reactions	$R'H + RH \rightarrow R''H + R'''H$
Radical-isomerization reactions	$R^{\bullet} \rightarrow R'^{\bullet}$

The yield of propylene produced in a pyrolysis furnace is a function of the feedstock and the operating severity of the pyrolysis. The optimized propylene yield can reach a maximum of approximately 18% by weight [24]. The lack of selectivity for propylene is the most obvious disadvantage for its production by steam cracking. In

addition, product separation by distillation is a complicated and costly process, in which propylene is produced as the overhead distillation product. Two grades of propylene are commonly produced: a chemical grade, which consists of 92–94 wt% propylene, and a polymer-grade with less than 90% wt propylene [9].

1.2.2 Fluidized catalytic cracking

Fluidized catalytic cracking offers a higher selectivity toward propylene as well as butane [25]. This process is similar to steam cracking, except solid acid catalysts are used and the reaction is run without steam. In fluid catalytic cracking, a partially vaporized gas oil or even heavy oil is placed in contact with zeolite catalysts (aluminosilicates). Contact time varies from 5 sec–2 min; pressure usually is in the range of 250–400 kPa, depending on the design of the unit; reaction temperatures are 720–850 K [9]. The main products are gasoline-boiling-range hydrocarbons, C_4 and lighter gas, and coke. Propylene is achieved as a by-product, and the yield varies, depending on reaction conditions. Yields of 2–5% based on feedstock are common [26,27].

The solid acid catalysts are poisoned by feedstock contaminants-metals and various nitrogen and sulfur compounds, as well as by coke formation [26]. Organic compounds containing nitrogen and sulfur yield hydrogen cyanide, ammonia, hydrogen sulfide and other compounds when cracked [28]. So, the feedstocks need to be treated to prevent environmental pollution, incurring additional cost. However, coke formation in this process proves to be beneficial, as the heat balance between the reactor and catalyst regenerator can be reached by combusting the coke deposited catalysts in the regenerator, a highly exothermic process. The heat produced during catalysts regeneration is recovered by recycling the catalysts to the reactor section. Propylene is recovered at the

vapor-recovery unit with wet gas passing through an absorber, where it contacts a hydrocarbon liquid, usually a heavy naphtha, which extracts heavier molecules and allows the lighter components (hydrogen, methane, etc.) to pass through. Subsequently the absorbent is then passed to a stripper, in which dissolved hydrocarbons are removed, and the lean oil is recycled to the absorber. Finally, the absorbate is passed to a depropanizer where a propane–propylene stream is taken as the overhead.

1.2.3 Propane dehydrogenation

1.2.3.1 Commercial dehydrogenation of propane

Currently, there are four different kinds of commercial processes for propane dehydrogenation. These are CATOFIN from ABB Lummus, OLEFLEX from UOP, Fluidized Bed Dehydrogenation from Snamprogetti, and Steam Active Reforming (STAR) from Phillips Petroleum [9]. Although involved in the same reaction of propane dehydrogenation, these technologies differ in the type of catalyst, the reactor design, operating conditions as well as methods used to increase the conversion and solve deactivation of the catalysts. Due to thermodynamic equilibrium limitation for propane conversion, high temperatures (700~900 K) are usually used. These technologies are summarized in Table 1-3.

Table 1-3. Commercial dehydrogenation processes

Process	Oleflex	Catofin	STAR (Steam Active Reforming)	Snamprogetti
Catalyst	supported platinum	supported chromium oxide	supported platinum	supported chromium oxide
Reactor system	moving bed	fixed bed	fixed bed	fluidized bed
License	UOP	ABB Lummus	Philips Petroleum	Snamprogetti-Yarsintez

The UOP Oleflex process can be separated into three different sections: the reactor section, the product recovery section, and the catalyst regeneration section (Figure 1-2) [29]. The reactor section of the Oleflex process consists of four side-by-side, radial flow, moving-bed reactors connected in series, charge and interstage heaters, and a reactor feed-effluent heat exchanger. The heat of reaction is supplied by preheated feed and interstage heaters, and the gas-phase reaction is carried out over a catalyst, platinum supported over alumina, under very near isothermal conditions [9]. In the product recovery section, the reactor effluent is cooled, compressed, dried, and sent to a cryogenic system to separate hydrogen from hydrocarbon. Separator liquid is sent to a selective hydrogenation unit to eliminate diolefins and acetylenes, and then the liquid goes to a deethanizer and propanepropylene splitter to produce propylene product [30]. Unconverted propane is recycled to the reactor section.

The first commercial installation of this technology was made in 1990 by the National Petrochemical Corporation in Thailand, with an annual capacity of 100,000 tons, and it became the first commercial scale propane dehydrogenation unit. A second unit, at 245,000 tons capacity was built in South Korea by the ISU Chemical Company [31].

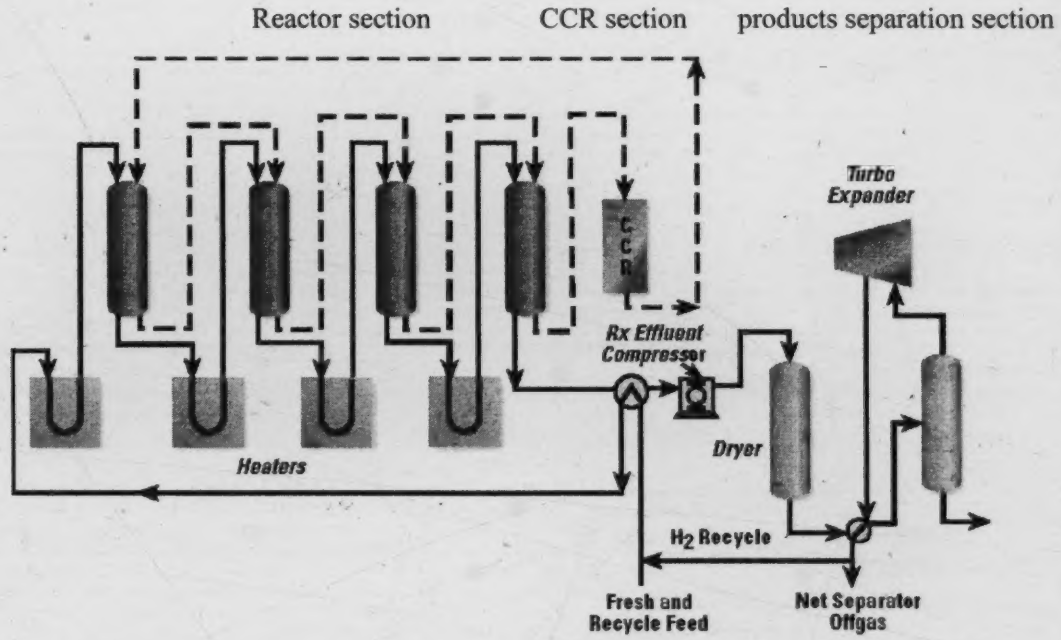

Figure 1-2. Schematic of Oleflex process for propane dehydrogenation (Adapted from ref.29).

Catofin dehydrogenation is a continuous process using a relatively inexpensive and durable chromium oxide–alumina as catalyst. The catalyst can be easily and rapidly regenerated without loss in activity. A vacuum was employed to improve propylene selectivity and to increase the propane conversion. Dehydrogenation is typically carried out over fixed beds with five reactors, two of which are on-stream, while another two are being regenerated and one is being purged. Figure 1-3 shows the schematic of the process

operation [32]. First, fresh feed and recycle feed are vaporized by exchange with various process streams and then raised to reaction temperature in the charge heater. The reactor effluent is routed through a high pressure steam generator, feed-effluent exchanger, and trim cooler to the compressor [33]. The compressor discharge is cooled, dried and routed to the low temperature recovery section to reject light ends. Recovered liquids from the low temperature recovery section, along with the effluent flash drum liquid, are fed to distillation facilities unit for product recovery. The reactors are cycled between the reaction and the reheat/regeneration modes, and the thermal inertia of the catalyst controls the cycle time, which is typically less than 10 minutes [34].

This technology was first commercialized in 1986 for the production of isobutylene, and the first plant to use this technology for propylene production was built at Antwerp by North Sea Petrochemicals [9]. Currently, there are two Catofin units having been licensed to produce 675,000 MTA of propylene, with the other one built in Morelos, Mexico by Pemex [9,34].

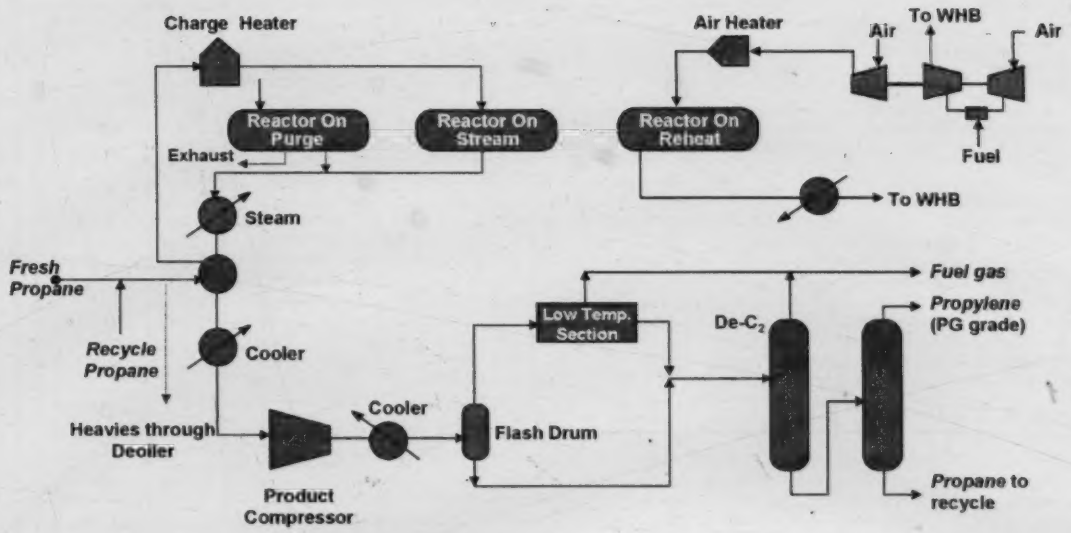

Figure 1-3. Schematic of Catofin process for propane dehydrogenation (Adapted from ref.32).

Steam-activated reforming technology uses a fixed-bed reactor with platinum supported catalyst in. In this process, steam is added to the hydrocarbon feed to suppress coke formation and to increase the equilibrium conversion by lowering partial pressures of hydrogen and propane. Typically the reaction is carried out in multiple fired tube reactors in parallel operating under isothermal conditions and at pressures of 50–60 psig.

Fluidized bed dehydrogenation technology resembles conventional fluidized catalytic cracking technology used in the petroleum refining industry. The catalyst of chromium oxide on alumina is used in this technology and is recirculated from the reactor to the regeneration section on a 30–60-min cycle. This continuous fluidized-bed dehydrogenation technology is mostly prevalent in the former Soviet Union [9,31].

Due to equilibrium limitation for propane dehydrogenation, per-pass propylene yield in all of these commercial processes is not high. Concurrent efforts are also directed at removing hydrogen in this process [35,36].

1.2.3.2 Oxidative dehydrogenation of propane

To overcome the equilibrium limitation for propane dehydrogenation, oxidative dehydrogenation of propane was proposed and has been extensively studied [37,35,38,39,40,41]. Oxidative dehydrogenation occurs under milder conditions in the presence of a hydrogen acceptor (oxygen), converting a highly exothermic process into an exothermic reaction:

$$C_3H_8 + \frac{1}{2}O_2 \rightarrow C_3H_6 + H_2O \qquad \Delta H_f^o = -117.1kJ \cdot mol^{-1} \qquad (1\text{-}2)$$

The main reaction by-products are carbon monoxide and carbon dioxide, the thermodynamically more stable products.

$$C_3H_8 + \frac{7}{2}O_2 \rightarrow 3CO + 4H_2O \qquad \Delta H_f^o = -1194.9kJ \cdot mol^{-1} \qquad (1\text{-}3)$$

$$C_3H_8 + 5O_2 \rightarrow 3CO_2 + 4H_2O \qquad \Delta H_f^o = -2043.9kJ \cdot mol^{-1} \qquad (1\text{-}4)$$

Advantages of the oxidative dehydrogenation of propane are that the process is exothermic, proceeds at lower temperatures, and overcomes the equilibrium limit. However, this process is complex and suffers from several limitations:

(i) Thermodynamics favors the complete oxidation of propane.

(ii) The C-H bonds in propane are stronger than those in propylene, making propylene prone to further oxidation.

(iii) All oxidation reactions are exothermic, so excess heat must be removed to prevent over oxidation and catalyst damage.

In addition to oxygen, oxidizing agents can include halogens, nitrous oxides, carbon dioxide and other compounds. There are a wide range of oxides investigated as catalysts for oxidative dehydrogenation of propane, which are reviewed and analyzed in the literature [38,39,40,41,42]. They can be classified into three categories: (1) catalysts based on alkali or alkaline earth oxides; (2) catalysts based on reducible transition metal oxides; and (3) other catalysts such as B/P oxides, Ga/zeolite, LaF_3/SmO. Although intensive studies have been conducted on this oxidative dehydrogenation technology, many challenges exist. These include development of a method to increase the selectivity to propylene and identifying the reaction mechanism that is need before proceeding to commercialization.

1.3 Objectives

The objectives of this work are to investigate the feasibility of the process of propane dehydrogenation in proton-conducting fuel cell that can be operated at high temperatures (600-700°C), by developing the suitable materials for protonic electrolyte, anode and cathode. Since this has not been extensively studied, the feasibility of protonic electrolyte capable of providing high proton conductivity and good stability will be examined. A suitable anode catalyst will developed and examined that exhibits high electro-catalytic activity toward propane dehydrogenation and high stability in fuel cell systems.

In addition, the reaction process of propane dehydrogenation in the proton-conducting fuel cell will be studied to advance current knowledge of the combination of the chemical process of propane dehydrogenation with fuel cell technology.

Consequently, the findings of these investigations can provide an overall understanding and more insight into the process of electrochemical reaction of propane dehydrogenation in the fuel cell, thereby providing guide for the dehydrogenation of other alkanes (e.g. ethane and butane) in a fuel cell.

1.4 Organization of thesis

The thesis is the summary and condensation of the results from the following 8 papers published, submitted, and/or presented at conferences during the Ph. D program.

1. Y. Feng, J. Luo and K.T. Chuang, "Propane Dehydrogenation in a Proton-Conducting Fuel Cell ", submitted to ***Journal of Physical Chemistry, C*** (Aug. 2007).

2. Y. Feng, J. Luo and K.T. Chuang, "Proton Conducting Materials and Their Application in Solid Oxide Fuel Cell as Electrolytes", submitted to ***Journal of Fuel Cell technology***, (Aug. 2006).

3. Y. Feng, J. Luo and K.T. Chuang, "Analysis and Improvement of Chemical Stability of Y-Doped $BaCeO_3$ as Proton-Conducting Electrolytes in $C_3H_8 - O_2$ Fuel Cells", ***Journal of New Materials for Electrochemical Systems***, 10 (3), 147-152 (2007).

4. Y. Feng, J. Luo and K.T. Chuang, "Carbon Deposition During Propane Dehydrogenation in a Fuel Cell", ***Journal of Power Sources***, 167 (2), 486-490 (2007).

5. Y. Feng, J. Luo and K.T. Chuang, "A Method to Measure the Proton Conductivity of $LiNaSO_4$ under Fuel Cell Conditions", ***Journal of the Electrochemical Society,*** 153 (6), A1049-A1052 (2006).

6. Y. Feng, J. Luo and K.T. Chuang, "Chemical Stability of $LiNaSO_4$ Electrolyte during Operation in a H_2-O_2 Fuel Cell", ***Journal of the Electrochemical Society***, 153 (5), A865-A868 (2006).

7. Y. Feng, J. Luo and K.T. Chuang, "Conversion of Propane to Propylene in a Proton-Conducting Solid Oxide Fuel Cell", ***Fuel,*** 86, 123-128, 2006.

8. Y. Feng, J. Luo, S. Wang, J. Melnik and K.T. Chuang, "Investigation of Y-doped $BaCeO_3$ as Electrolyte in Propane Fueled Proton Conducting Solid Oxide Fuel Cell", ***Proceedings of the International Symposium on Fuel Cell and Hydrogen Technologies***, 1st, Calgary, AB, Canada, 461-471(2005).

In chapter two, solid sulfate $LiNaSO_4$ is studied as the protonic electrolyte in the fuel cell for propane dehydrogenation. The feasibility of such a material is examined in detail by studying its chemical stability in the fuel cell with hydrogen-containing atmosphere and measuring its proton conductivity under fuel cell conditions by developing a new method.

Chapter three presents a study of Y-doped $BaCeO_3$ as a protonic electrolyte in the fuel cell and methods to enhance the suitability of this perovskite material in the fuel cell set-up by developing a new fuel cell system. In addition, the feasibility of conversion of propane to propylene in the proton-conducting fuel cell based on Y-doped $BaCeO_3$ as the electrolyte and platinum as electrodes was investigated.

Chapter four concerns the reaction process of propane dehydrogenation in the proton-conducting fuel cell. The side electrochemical reactions competing with the desired reaction of propane dehydrogenation during this process are identified. It is also shown that the operating conditions influence the competition of all these electrochemical reactions.

In chapter five, chromium oxide based anode catalysts are synthesized by the sol-gel method and their electro-catalytic activity for propane dehydrogenation and selectivity to propylene are studied in the fuel cell.

Chapter six analyzes the behavior of carbon deposition during propane dehydrogenation in the fuel cell system under different operating conditions. A comparison of carbon deposited on anode catalysts was made between open circuit conditions and current flow conductions. Some strategies to suppress carbon deposition are also discussed.

The general conclusions are given in chapter seven.

References:

[1] K. Chen, E. Iglesia, A.T. Bell, "Isotopic Tracer Studies of Reaction Pathways for Propane Oxidative Dehydrogenation on Molybdenum Oxide Catalysts", *Journal of. Physical Chemistry B*. 105, 646-653 (2001).

[2] Z. Xu, "State-of-the-art catalytic cracking processes for maximizing propylene production", *Lianyou Jishu Yu Gongcheng*, 36 (8), 4-8 (2006).

[3] J. Liu, Y. Hou, "Application of LOSA-1 to increased propylene production with FCC", *Zhongwai Nengyuan*, 11 (1), 73-77 (2006).

[4] A. Corma, F.V. Melo, L. Sauvanaud,F. Ortega, "Light cracked naphtha processing: Controlling chemistry for maximum propylene production", *Catalysis Today*, 107-108, 699-706 (2005).

[5] J. Verstraete, V. Coupard, C. Thomazeau, P. Etienne, "Study of direct and indirect naphtha recycling to a riser FCC unit for maximum propylene production", *Catalysis Today*, 106, 62-71 (2005).

[6] G. Parkinson, "Propylene production", *Chemical Engineering Progress*, 100 (3), 8-11 (2004).

[7] J.D. Pless, "Oxidative dehydrogenation of propane over magnesium vanadates and molybdates", *Ph.D. Dissertation*, Northwest University, pp.5-15 (2003).

[8] L.E. Chambers, W.S. Potter, "Design ethylene furnaces. 2. Maximum olefins", *Hydrocarbon Process* 53, 121-6 (1974).

[9] N. Calamur, M. Carrera, *Kirk-Othmer Encyclopedia of Chemical Technology (online)* (2006).

[10] X. Yang, E. Bai, "Application of combinatorial catalysis in development of petrochemical catalysts", *Huagong Jinzhan*, 25 (2), 121-125 (2006).

[11] G. Deo, M. Cherian, T.V.M. Rao, "Oxidative dehydrogenation (ODH) of alkanes over metal oxide catalysts", *Chemical Industries (Boca Raton, FL, United States)*, 108, 491-516 (2006).

[12] H. You, "Kinetics of propane oxidative dehydrogenation to propylene", *Petroleum Science and Technology*, 23 (11-12), 1441-1452 (2005).

[13] S.Y. Yu, "Coupling alkane dehydrogenation reactions with hydrogenation reactions on cation-modified H-ZSM5", *Ph.D. Dissertation*, University of California, Berkeley (2001), p.8-p.30.

[14] C.K. Cheng, "Application of PBI membrane polymer fuel cell for conversion of hydrocarbon", *Masters Thesis*, University of Alberta, pp.120-129 (2004).

[15] C. Lu, W. L. Worrell, C. Wang, S. Park, H. Kim, J. M. Vohs and R. J. Gorte, "Development of solid oxide fuel cells for the direct oxidation of hydrocarbon fuels", *Solid State Ionics*, 152-153, 393-397 (2002).

[16] K. Eguchi, H. Kojo, T. Takeguchi, R. Kikuchi, K. Sasaki, "Fuel flexibility in power generation by solid oxide fuel cells", *Solid State Ionics*, 152-153, 411-416 (2002).

[17] C. Lu, W.L. Worrell, C. Wang, S. Park, H. Kim, J.M. Vohs, R.J. Gorte, "Development of solid oxide fuel cells for the direct oxidation of hydrocarbon fuels", *Solid State Ionics*, 152-153, 393-397 (2002).

[18] S.A. Barnett, J. Liu, B.D. Madsen, Z. Zhan, "Direct hydrocarbon solid oxide fuel cells", *Proceedings - Electrochemical Society*, 53-65 (2003).

[19] J.H. White, M. Schwartz, A.F. Sammells, "Solid state proton and electron mediating membrane and use in catalytic membrane reactors", *United States Patent*, No. 6,281,403 B1, 28 Aug. 2001.

[20] W.G. Barker, B.S. Berland, M. Schwaartz, L. Simpson, J. Armstrong, "Apparatus and method for the design and manufacture of thin-film electrochemical devices", *United States Patent*, No. 6,772,501 B2, 10 Aug. 2004.

[21] D.J. Edllund, D.T. Friesen, "Hydrogen-permeable composite metal membrane and uses thereof", *United States Patent*, No.5, 217,506, 08 Jun. 1993.

[22] H. McCurdy, www.cmaiglobal.com/news/files/wpss/pdf , May 2003.

[23] A.G. Goosens, M. Dente, E. Ranzi, "Improve steam cracker operation", *Hydrocarbon Process*, 57 (9), 227-236 (1978).

[24] L.E. Chambers, W.S. Potter, "Design ethylene furnaces 1. maximum ethylene", *Hydrocarbon Process*, 53, 121-126 (1974).

[25] B.S. Greensfelder, H.H. Voge, G.M. Good "Catalytic and thermal cracking of pure hydrocarbons-mechanisms of reaction", 41 (11), 2573-2584 (1949).

[26] E. G. Wollaston, W. J. Haflin, and W. D. Ford, "What influences cat cracking", *Hydrocarbon Process*, 54 (9), 93-100 (1975).

[27] R.B. Ewell, G. Gadmer, "Design cat crackers by computer", *Hydrocarbon Process*, 57 (4), 125-134 (1978).

[28] R. Sadeghbeigi, *Fluid Catalytic Cracking Handbook: Design, Operation, and Troubleshooting of FCC Facilities*, Gulf Publishing Company, 1995.

[29] http://www.uop.com/lightolefins/5031.html

[30] http://www.uop.com/lightolefins/5030.html

[31] E. Chang, "Alkane dehydrogenation and aromatization", *Process Economics Program*, SRI International, Menlo Park, California, 1992.

[32] http://www.ipqa.org.ar/Congreso3/presentaciones_pdf/p1a/barros.pdf.

[33] http://www.abb.com/Industries/db0003db001876/3204d71984e4f143c1257 1f7006505fa.aspx

[34] S. Gussow, D.C. Spence, E.A. White, "Dehydrogenation links LPG to octanes", *Oil & Gas Journal*, 78 (49), 96-101 (1980).

[35] Z.D. Ziaka, R.G. Minet, T.T. Tsotsis, "Propane dehydrogenation in a packed-bed membrane reactor", *AIChE Journal*, 39 (3), 526-529 (1993).

[36] J. Shu, B.P.A. Grandjean, A. VanNete, S. Kaliaguine, "Catalytic palladium based membrane reactors-a review", *Canadian Journal of Chemical Engineering*, 69 (5), 1036-1060 (1991).

[37] M.A. Banares, "Supported metal oxide and other catalysts for ethane conversion: a review", *Catalysis Today*, 51(2), 319-348 (1999).

[38] F. Cavani, F. Trifiro, "The oxidative dehydrogenation of ethane and propane as an alternative way for the production of light olefins", *Catalysis Today*, 24 (3), 307-313, (1995).

[39] S.T. Oyama, G.A. Somorajai, "Effect of structure in selective oxide catalysis – oxidation reactions of ethanol and ethane on vanadium-oxide", *Journal of Physical Chemistry*, 94 (12), 5022-5028 (1990).

[40] E.A. Mamedov, V.C. Corberán, "Oxidative dehydrogenation of lower alkanes on vanadium oxide-based catalysts. The present state of the art and outlooks", *Applied Catalysis A: General*, 27 (1-2), 1-40 (1995).

[41] E. Morales, J.H. Lunsford, "Oxidative dehydrogenation of ethane over a lithium-promoted magnesium-oxide catalyst", *Journal of Catalysis*, 118 (1), 255-265 (1989).

[42] F. Cavani, N. Ballarinia, A. Cericola, "Oxidative dehydrogenation of ethane and propane: How far from commercial implementation?", *Catalysis Today*, 27 (4), 113-131 (2007).

CHAPTER 2

INVESTIGATION OF $LiNaSO_4$ AS PROTON-CONDUCTING ELECTROLYTE IN FUEL CELLS

2.1 Introduction

Typically solid oxide fuel cells (SOFCs) using oxide ion conducting electrolytes such as yttrium stabilized zirconia (YSZ) require operating temperatures as high as 900-1000°C for optimum performance. The requirement for operation under such strenuous conditions places stringent requirements on the materials used for interconnection, sealing, and construction. To avoid problems associated with operation at very high temperatures, efforts have been made to develop fuel cells using proton-conducting electrolytes, since proton conduction can be thermally activated at lower temperatures than oxide ion conduction [1,2]. Compared to the conventional oxide ion conductors, protonic electrolytes for fuel cells have exclusive advantages [1,2,3,4,5]. For example, fuel can be recycled without dewatering in proton-conducting fuel cells because water is generated at the cathode. More importantly, separation of the proton removal and oxidation steps into separate compartments favours high selectivity for conversion of hydrocarbon feed to value-added products, as there is no oxygen available for further reactions of the product at the anode [3,4]. However, in view of the present intermediate temperature protonic electrolytes, whether polymers (e.g. Nafion) for proton exchange membrane fuel cells (PEFCs) at low temperature [6,7,8,9] or solid oxides (e.g. doped

$SrCeO_3$) for SOFCs operating at high temperature [10,11,12,13,14], there are very few highly conducting and stable proton conductors for operation at 300-700°C.

Lithium sodium sulfate ($LiNaSO_4$) is known to be a good super-ionic conductor at high temperature [15,16,17,18]. Total ionic conductivity of $LiNaSO_4$ is 10^{-1} $S.cm^{-1}$ at 550°C, about ten times higher than that of the perovskites Y-doped $BaCeO_3$ (BCY) or $SrCeO_3$ [19,20,21,22,23]. It undergoes a first order phase transition with the high temperature cubic phase exhibiting very high cationic conductivity. The cation mobility is enhanced by strong coupling to the rotation of the translationally immobile sulfate ions according to the so-called paddle-wheel mechanism [24,25,26]. When exposed to hydrogen, proton conduction in this material occurs with coordination of the proton to oxygen of the SO_4^{2-} tetrahedron, which is similar to proton solvation in water-containing systems. So, protons directly coordinate with SO_4 groups to form strong H-SO_4 bonds and fast rotation of sulfate groups strongly "pushes" Li^+, Na^+ and H^+ ions into motion. Tao, et al. [27,28] studied $LiNaSO_4$ as a proton conductor and found that it has high conductivity and good initial performance when using $LiNaSO_4$-Al_2O_3 composite electrolyte membranes in H_2-O_2 fuel cells. However, the performance is decreased rapidly with time. The same phenomenon was also found in our preliminary tests when using $LiNaSO_4$ as proton-conducting electrolytes in the fuel cell for propane dehydrogenation with platinum as electrodes (small amounts of hydrogen could be produced from propane thermal cracking under the fuel cell conditions). In addition, despite the high total conductivity of $LiNaSO_4$, the current densities and power densities obtained from fuel cells using $LiNaSO_4$ electrolyte were much lower than those from fuel cells employing BCY electrolyte during the same initial test time.

Based on these facts, there are speculations that the anion may be reduced by H_2, in a matter similar to the reduction of Li_2SO_4 [29]. The high conductivity of $LiNaSO_4$ may be attributed largely to metal cation (Li^+, Na^+) conduction under the fuel cell conditions. So, it is important to investigate the suitability of $LiNaSO_4$ as the proton-conducting electrolyte in fuel cells for propane dehydrogenation by studying its chemical stability in hydrogen-containing atmosphere, and also measuring accurately the proton conductivity in such materials, which can strongly contribute to fuel cell performance.

2.2 Stability of $LiNaSO_4$ in hydrogen

2.2.1 Thermodynamic Analysis

Knowledge of the thermodynamic properties of $LiNaSO_4$ is inadequate or even unavailable for this study, therefore we have to consider this issue from other aspects. Li_2SO_4 and Na_2SO_4 have the same structure as

$$M^+\left(O=\overset{\overset{O}{|}}{\underset{\underset{O}{||}}{S}}-O\right)^{2-}M^+$$

where, M = Li or Na

So, it is reasonable to believe that the thermodynamic properties of $LiNaSO_4$, such as Gibbs free energy, fall between those of Li_2SO_4 and Na_2SO_4.

For Li_2SO_4, the following reactions can be considered between Li_2SO_4 and H_2 [29].

$$H_2+Li_2SO_4=2Li+H_2SO_4 \qquad (2\text{-}1)$$

$$4H_2+Li_2SO_4=4H_2O+Li_2S \qquad (2\text{-}2)$$

$$4H_2+Li_2SO_4=2H_2O+2LiOH+H_2S \quad (2\text{-}3)$$

$$6H_2+2Li_2SO_4=4H_2O+4LiOH+S_2 \quad (2\text{-}4)$$

$$6H_2+2Li_2SO_4=4H_2O+4LiOH+2S \quad (2\text{-}5)$$

$$Li_2SO_4+2H_2O=2LiOH+H_2SO_4 \quad (2\text{-}6)$$

Similarly, for Na_2SO_4, the above reactions should be taken into account. In addition, reactions (2-13) and (2-14) are also included.

$$H_2+Na_2SO_4=2Na+H_2SO_4 \quad (2\text{-}7)$$

$$4H_2+Na_2SO_4=4H_2O+Na_2S \quad (2\text{-}8)$$

$$4H_2+Na_2SO_4=2H_2O+2NaOH+H_2S \quad (2\text{-}9)$$

$$6H_2+2Na_2SO_4=4H_2O+4NaOH+S_2 \quad (2\text{-}10)$$

$$6H_2+2Na_2SO_4=4H_2O+4NaOH+2S \quad (2\text{-}11)$$

$$Na_2SO_4+2H_2O=2NaOH+H_2SO_4 \quad (2\text{-}12)$$

$$H_2+Na_2SO_4= Na_2SO_3+ H_2O \quad (2\text{-}13)$$

$$4H_2+2Na_2SO_4=Na_2S_2O_3+2NaOH+3H_2O \quad (2\text{-}14)$$

Among these reactions, the ones possibly occurring in the present experiments can be identified from calculations of their Gibbs free energy changes. According to the thermodynamic data provided in reference [30], the calculated Gibbs free energy changes of all the reactions are shown in Figures 2-1 and 2-2. From these figures, it is obvious that only reactions (2-2), (2-3) and (2-8) are spontaneous over the range 100°C to 1000°C, and above 500°C reactions (2-4) and (2-9) are also possible. Based on the fact that Li_2SO_4 and Na_2SO_4 are both thermodynamically unstable in hydrogen, we can safely

come to conclusion that $LiNaSO_4$ is also not stable in hydrogen at high temperatures. Of course, in real experiments, the kinetics of such reactions have to be considered.

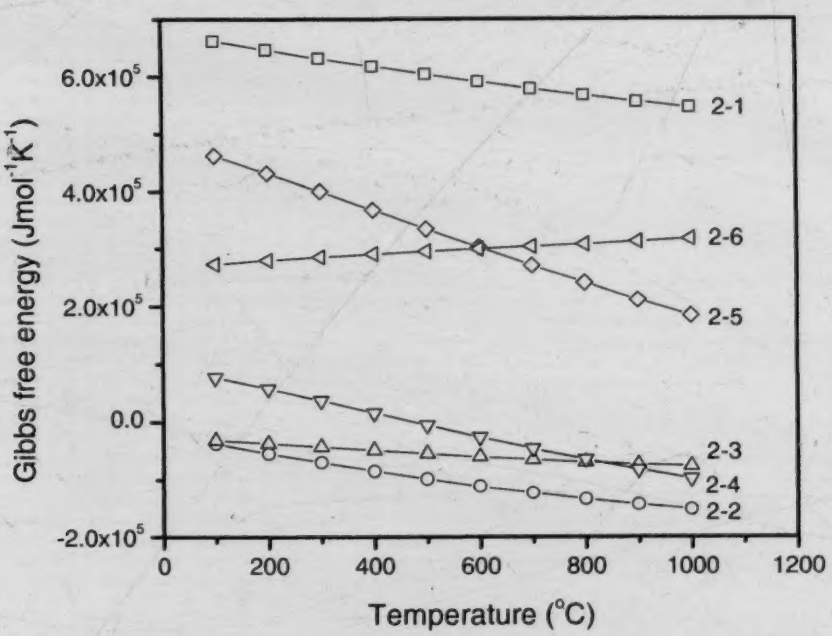

Figure 2-1. Gibbs free energy changes of possible reactions for Li_2SO_4 at different temperatures.

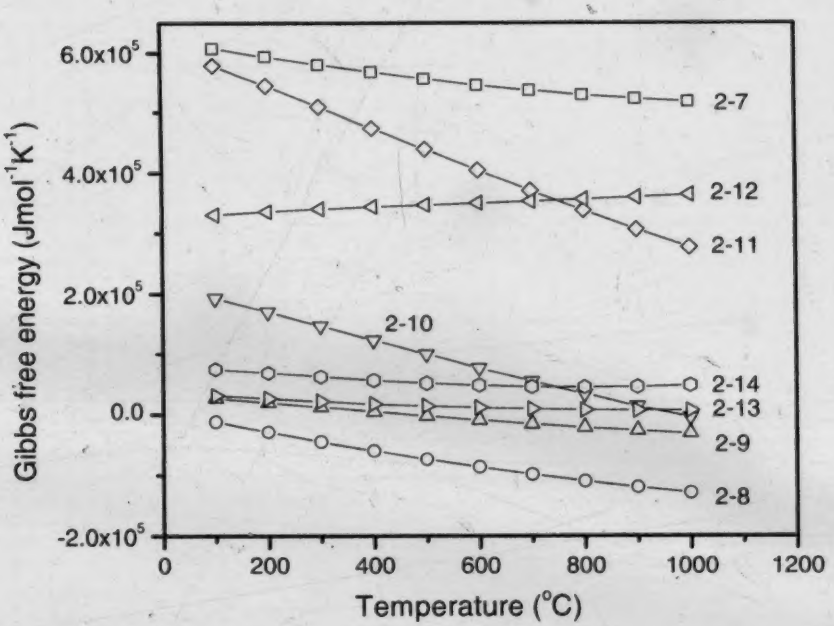

Figure 2-2. Gibbs free energy changes of possible reactions for Na_2SO_4 at different temperatures.

2.2.2 Experimental

2.2.2.1 Materials

The electrolyte $LiNaSO_4$ –Al_2O_3 was prepared as described in the literature [3]. A 1:1 molar mixture of analytically pure Li_2SO_4 (Alfa Aesar, 99.7%) and Na_2SO_4 (Alfa Aesar, 99.0%) was dissolved in deionized water with stirring by a Teflon-coated magnetic stir bar. The resulting aqueous solution was then heated to 150°C with continuous stirring and it was kept at 150°C until the water completely vaporized. The solid mixture was then calcined at 750°C for 10 h to synthesize $LiNaSO_4$ compound. XRD (Rigaku Rotaflex X-ray diffractometer) showed that the resulting powder was pure $LiNaSO_4$. A mixture of $LiNaSO_4$ and $Al(NO_3)_3{\cdot}9H_2O$ in a molar ratio of 6:8 was

dissolved in deionized water with stirring by a Teflon-coated magnetic stir bar and heated to 650°C for 15 h until all $Al(NO_3)_3 \cdot 9H_2O$ had decomposed to form Al_2O_3. The $LiNaSO_4$–Al_2O_3 powder was ground, sintered at 750°C for 20 h and then ground again. The fine powder (1-5 μm) was pressed into 2.54 cm diameter and 1.0 mm thick disks which were then sintered again at 700°C for 10 h.

Commercial platinum paste (Heraeus CL11-5100) was used as received to prepare the electrodes. The paste was screen printed on to opposed surfaces of the electrolyte disks and were dried in air at 120°C for 30 min to remove the organic solvent and to increase adhesion to the electrolyte.

Hydrogen (Praxair, PP 4.5) and oxygen (Praxair, grade 2.6) were used as anode and cathode gases, respectively. The fuel cell had the configuration:

$$H_2 | Pt | LiNaSO_4 - Al_2O_3 | Pt | O_2$$

2.2.2.2 Fuel cell system fabrication

A schematic diagram of the experimental H_2-O_2 fuel cell system with planar cell geometry is shown in Figure 2-3. The cell included a membrane electrode assembly (MEA) having anode and cathode compartments sealed to the respective faces of the MEA. The anode and cathode compartments were constructed using two co-axial alumina tubes. The inner tube (O.D.: 1.2 cm and I.D.: 1.0 cm) extended from outside the heated reaction zone to a position close to the respective electrode of the cell. The outer perimeter of each outer tube (O.D.: 2.84 cm and I.D.: 2.54 cm) was sealed to the membrane with a thin layer of ceramic sealant (Aremco 503). Platinum gauze (52 mesh) was applied as the current collector for both electrodes.

The assembled cell was placed in a tubular furnace (Thermolyne F79300) having a uniform temperature zone: ±0.6°C over the central 7.62 cm length of the cell and ±3.0°C to distances up to 7.62 cm each side of the MEA. To cure the sealant, the furnace temperature was increased at 0.5°C/min to 110°C, where it was kept for 2 h before being increased to 650°C for further heat treatment. During the period of increasing temperatures the cell was heated and there was nitrogen flowing in each chamber.

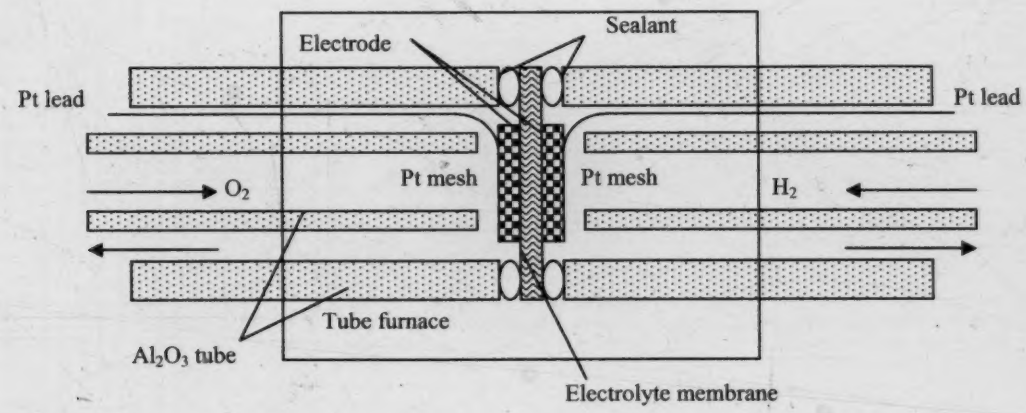

Figure 2-3. Schematic of fuel cell set-up using $LiNaSO_4$ as electrolyte.

2.2.2.3 Fuel cell tests

The fuel cell was heated in nitrogen to the desired operating temperature and, before the measurement of cell performances, anode feed was switched from nitrogen to pure hydrogen at the flow rate of 40 mL/min and cathode feed was switched from nitrogen to oxygen at the same flow rate. The cell I-V curve, OCV-time curve and impedance spectra of the fuel cell were recorded with a Gamry electrochemical

measurement system (PC4-750). Potentiodynamic mode was used when performing I-V measurements and the scanning rate was kept at 5 mV/s. Five data points were sampled per second to record each OCV-time curve. For electrochemical impedance spectroscopy (EIS), a 5 mV alternating potential signal was used with frequency ranging from 0.1 Hz to 100 kHz across the cell to measure the alternate current response. A complex impedance $Z(\omega)$ was determined and translated into a Nyquist plot, which is a plot of imaginary impedance (Y-axis) against the real impedance (X-axis) in a complex plane at different frequencies. The resistance of the cell was determined from the intercept with the X-axis of the Nyquist plot. To calculate the proton conductivity of the electrolyte, all external factors that could contribute to the overall measured resistance were eliminated [31].

2.2.3 Results and Discussion

2.2.3.1 Materials

$LiNaSO_4$ is the alkali double sulfate usually derived from Li_2SO_4 and Na_2SO_4 with a 1:1 molar ratio. From the phase diagram of the binary system Li_2SO_4-Na_2SO_4 (Figure 2-4), the solid $LiNaSO_4$ will melt above 610°C [32]. Consequently, the range of operating temperatures selected for testing was 550-650°C.

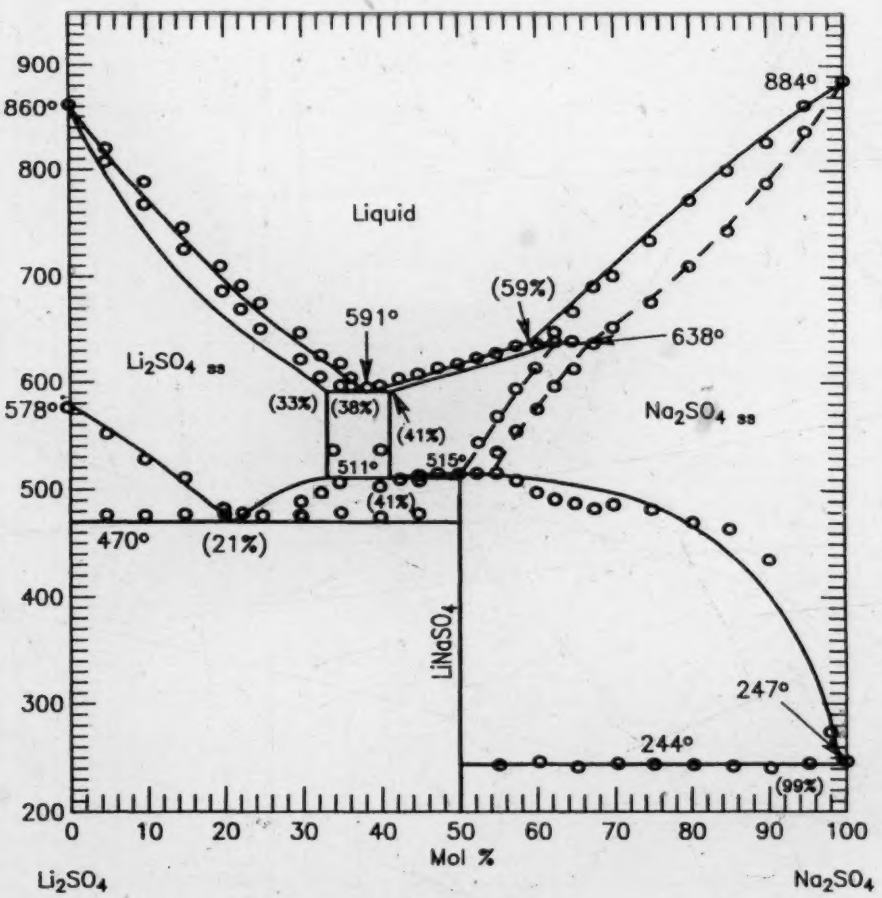

Figure 2-4. Phase diagram of binary system of Li_2SO_4-Na_2SO_4 (Reprinted with permission of The American Ceramic Society).

Usually, sintered tablets of pure inorganic salts have poor mechanical strength and are easy to crack when setting up the experiment. So, Al_2O_3 was added to $LiNaSO_4$ to form a composite electrolyte that had better mechanical strength.

2.2.3.2 Fuel cell performance

Figure 2-5 shows I-V characteristics for the fuel cell operating with 1 atm pure H_2 and O_2 at different temperatures. At 650°C, the maximum output current density was 112

mA/cm^2, while the OCV was about 1.5 V, a value that was even more than the theoretical EMF value calculated from the Nernst Equation for the pure H_2-O_2 fuel cell. Similar results were observed at 550°C and 600°C with the corresponding OCVs at 1.38 V and 1.41 V. It was inferred that there might have been some other reactions occurring in the fuel cell in addition to the electrochemical reaction:

$$H_2 + \frac{1}{2}O_2 \rightarrow H_2O \qquad (2\text{-}15)$$

Another test was conducted to measure the curves of OCV and conductivity of the fuel cell vs. time at 600°C with anode feeds before and after the switch to pure hydrogen, as shown in Figures 2-6, 2-7 and 2-8. The OCV of the cell before the switch to hydrogen was basically constant with time (Figure 2-6), while after the switch the OCV of the H_2-O_2 fuel cell depended on time with maximal value as high as 1.8 V and minimum near 0 V after about 100 min after switching from nitrogen to hydrogen, as shown in Figure 2-7. Corresponding to the test (Figure 2-7), the impedance spectroscopy was employed to determine the conductivities of $LiNaSO_4$–Al_2O_3 in the H_2-O_2 fuel cell with time (Figure 2-8). It can been deduced that the conductivity of $LiNaSO_4$–Al_2O_3 decreased with time and after 100 min the conductivity became two orders of magnitude lesser than that at 45 min after switching gases.

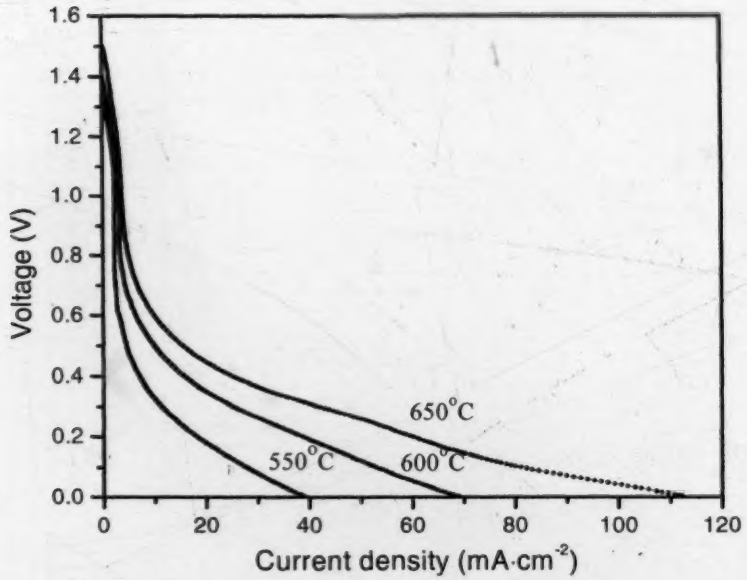

Figure 2-5. I-V curves of H_2-O_2 fuel cell with $LiNaSO_4$–Al_2O_3 at different temperatures.

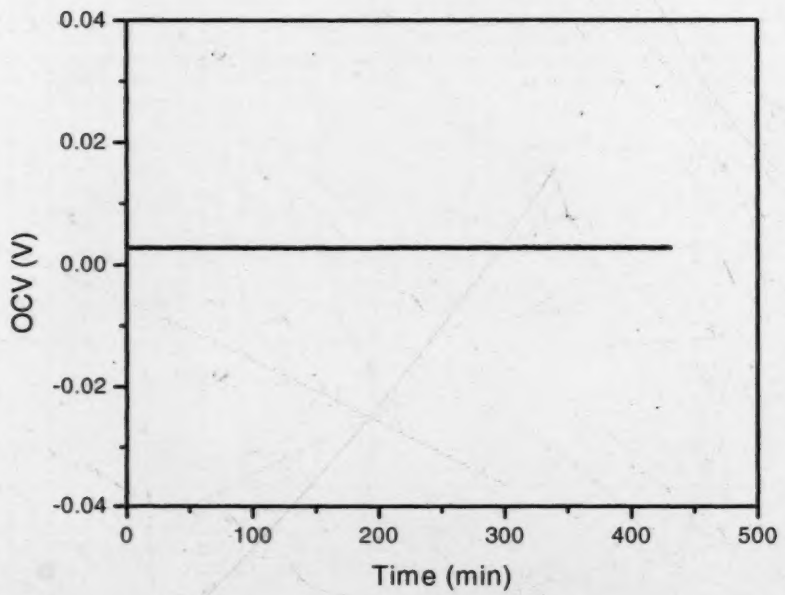

Figure 2-6. OCV-time curve of the cell with electrolyte of $LiNaSO_4$–Al_2O_3 and anode feed of nitrogen (before switch to hydrogen) at 600°C.

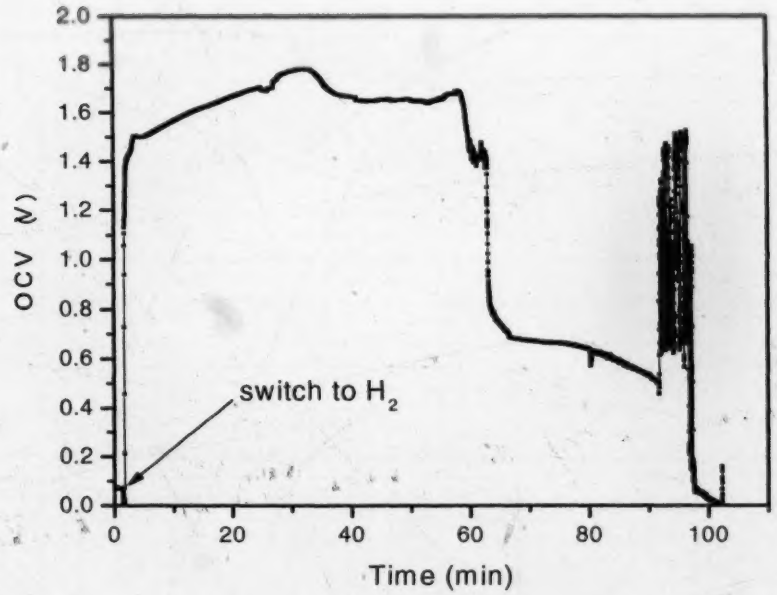

Figure 2-7. OCV-time curve of H_2-O_2 fuel cell with $LiNaSO_4$–Al_2O_3 at 600°C.

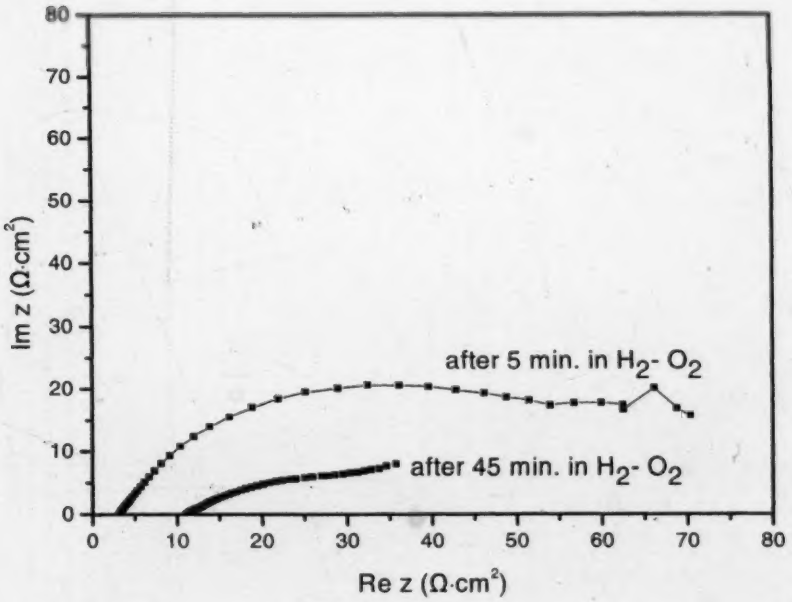

(a)

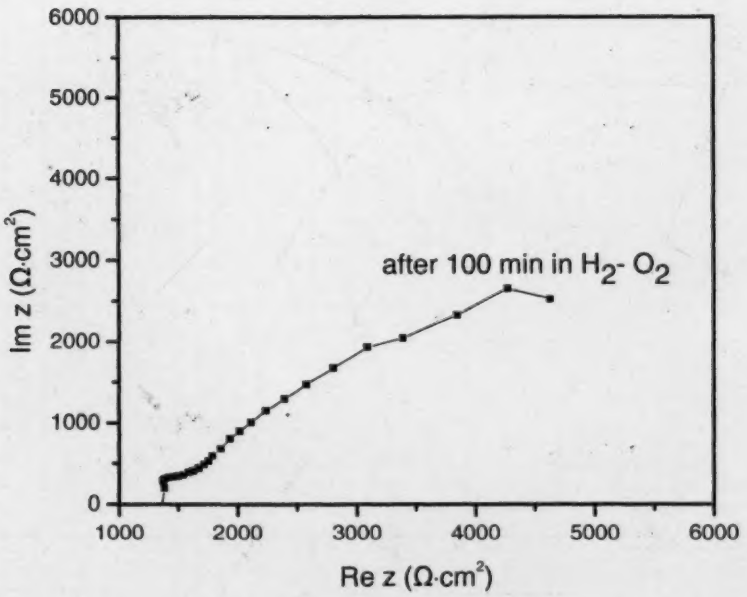

(b)

Figure 2-8. Impedance spectra of H_2-O_2 fuel cell with $LiNaSO_4$–Al_2O_3 at 600°C and different time under open circuit conditions.

Therefore, it can be concluded from the above results that the $LiNaSO_4$ may have reacted with hydrogen. Figure 2-6 excludes the possibilities of interaction among $LiNaSO_4$, Pt and O_2 under the fuel cell conditions. Although some researchers pointed out that decomposition of SO_4^{2-} ions in some sulfates was promoted by Pt catalyst [33,34], it showed no detectable effect on the decomposition for $LiNaSO_4$ under the fuel cell operating conditions. The conductivity of $LiNaSO_4$–Al_2O_3 in the cell with nitrogen as anode feed was monitored continuously for 8 h and there was no obvious change. The conclusion was also supported by gas chromatograph (GC) analysis, which showed that there were no gas products detected from decomposition of SO_4^{2-} ions, such as SO_3, SO_2 or O_2. In addition, the added Al_2O_3 only served as support for $LiNaSO_4$, and Tao, et al [27] demonstrated that there was no chemical reaction between Al_2O_3 and $LiNaSO_4$. Consequently, it was necessary to study the chemical stability of $LiNaSO_4$ in hydrogen.

2.2.3.3 Chemical stability of $LiNaSO_4$ in hydrogen

Pure $LiNaSO_4$ powder was heated in a quartz tube reactor flowing with pure hydrogen at 600°C for 10 h, and after that the products were tested by XRD, as shown in Figure 2-9. For comparison, the unprocessed $LiNaSO_4$ was also analyzed by XRD as shown in Figure 2-10. Comparing the two XRD profiles, it was obvious that there were some new phases produced from the products. From JCPDS cards, these peaks corresponded to $NaOH{\cdot}H_2O$, $3LiOH{\cdot}Li_2SO_4$ and $Na_2S{\cdot}5H_2O$.

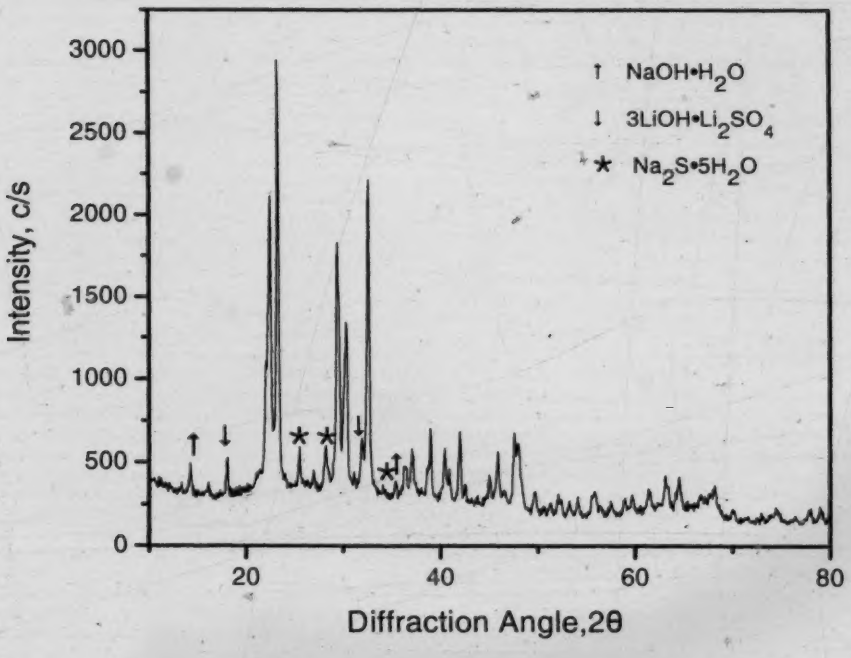

Figure 2-9. XRD profiles of $LiNaSO_4$ after heating in H_2 at 600°C for 10 h.

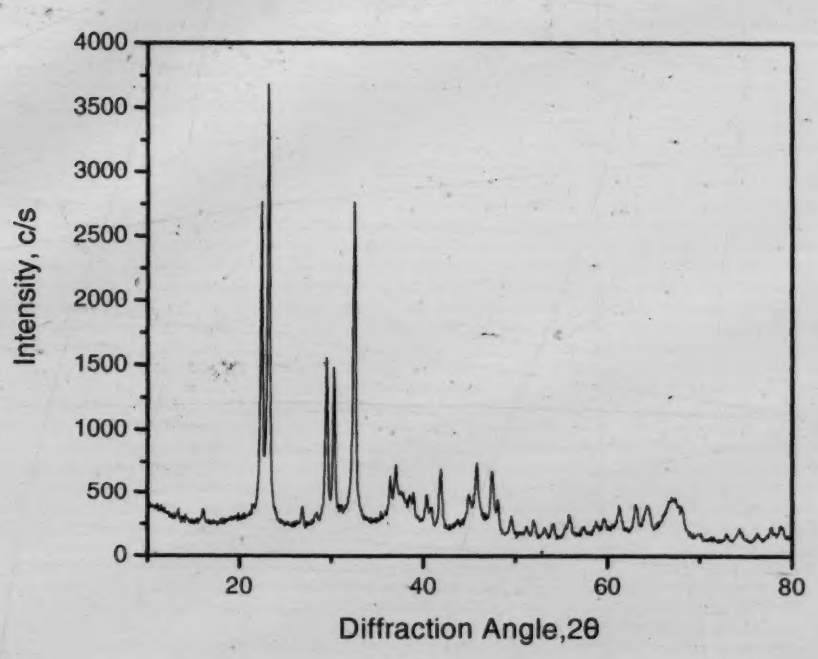

Figure 2-10. XRD profiles of $LiNaSO_4$ without processing with H_2.

In addition, during the experiment process, there was a foul gas produced in the outflow stream and, when it was fed into $CuSO_4$ solution, a black precipitate was produced. It was concluded that the pungent gas was H_2S and the black precipitate arose from the following reaction:

$$CuSO_4 + H_2S = CuS\downarrow + H_2SO_4 \qquad (2\text{-}16)$$

Based on the results, it can be seen that reactions (2-3), (2-8) and (2-9) actually occurred in the experiment, and other thermodynamically possible reactions (2-2) and (2-4) may also have had very low reaction rates under our experimental conditions. Therefore, $LiNaSO_4$ was not stable in hydrogen at high temperature, which was demonstrated by thermodynamic analysis and experiments.

2.3 Proton conductivity of $LiNaSO_4$ under fuel cell conditions

Normally, hydrogen concentration cells are used to determine the proton conductivities of electrolyte materials under fuel cell conditions. Unfortunately, hydrogen concentration cells cannot be used to determine the proton conductivity of $LiNaSO_4$ that is readily reduced in hydrogen at high temperatures, as just proved. Herein, the development of a new method by which the proton conductivity of reducible electrolytes can be determined under hydrogen at fuel cell conditions is presented.

2.3.1 Principles of the method

$LiNaSO_4$ is a mixed Li^+, Na^+ and H^+ ionic conducting material, and perhaps is also a weak O^{2-} conductor. Thus, to determine the proton conductivity it was necessary to restrict the conductivity of all ions, except protons.

To determine proton conductivity independently of all other ion conductivities, a non-reducible electrolyte that is substantially protonic was coated on both sides of the reducible electrolyte disk to form a sandwich. The proton conductor permitted only H^+ transport through the sandwich and prevented conduction of other ions, and also prevented exposure of the reducible electrolyte to hydrogen.

Full chemical and mechanical compatibility between the proton conductor and the electrolyte to be examined was required to ensure that there was good proton communication between the layers.

The proton conductivity of the non-reducible sandwiching electrolyte was determined separately from that of the sandwich. The proton conductivity of the reducible electrolyte was then determined.

In the present example, the proton conductivity of $LiNaSO_4$ under fuel cell conditions was determined using a sandwich disk in which that electrolyte was sandwiched between layers of the proton conducting perovskite $BaCeO_3$ (Figure 2-11). Some Y-doped oxides exhibit very high pure proton conductivity at high temperatures. At temperatures of 600-750°C, the proton transport number can be greater than 0.95 [15]. Thus, this kind of material is a good candidate for use as the proton conductor in a sandwich disk.

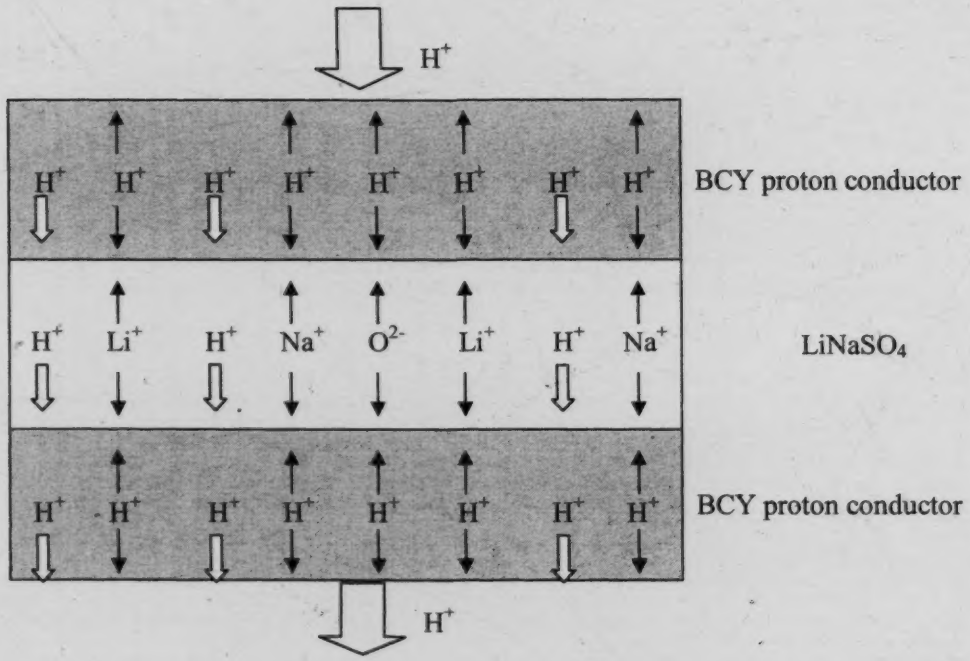

Figure 2-11. Configuration of sandwich disk to measure proton conductivity of $LiNaSO_4$.

2.3.2 Experimental

2.3.2.1 Sandwich disk preparation

There is a large difference between the thermal expansion coefficients of BCY and $LiNaSO_4$. Therefore, it was not possible to prepare a sandwich and then sinter the two materials simultaneously to make the disk. Instead, the difference of melting points of BCY and $LiNaSO_4$ was used to advantage. The melting point of $LiNaSO_4$ is near 610°C [32], while BCY does not melt below 1600°C. So, disks of BCY and $LiNaSO_4$ were

prepared separately and then sintered together in the sandwich configuration at 700°C, well above the melting point of $LiNaSO_4$.

Commercially available 15% Y-doped $BaCeO_3$ (BCY15; SCI Engineered Materials) powder was used to prepare the BCY disks. The powder was sequentially ground, pressed to form tablets, and sintered at 1550°C for 20 h. The tablets were then ground into disks 1.0 mm thick and 25 mm in diameter. $LiNaSO_4$ powder was synthesized as described previously. The powder was pressed into tablets that were sintered at 600°C for 10 h to form disks that were the same diameter as the BCY disks. The sandwich disk then was formed by heating together a sandwich comprising two BCY disks and one $LiNaSO_4$ disk at 800°C for 8 h (Figure 2-12). Pt paste (Heraeus CL11-5100) was screen-printed onto the surface of the electrolyte disk to prepare the anode and cathode catalysts.

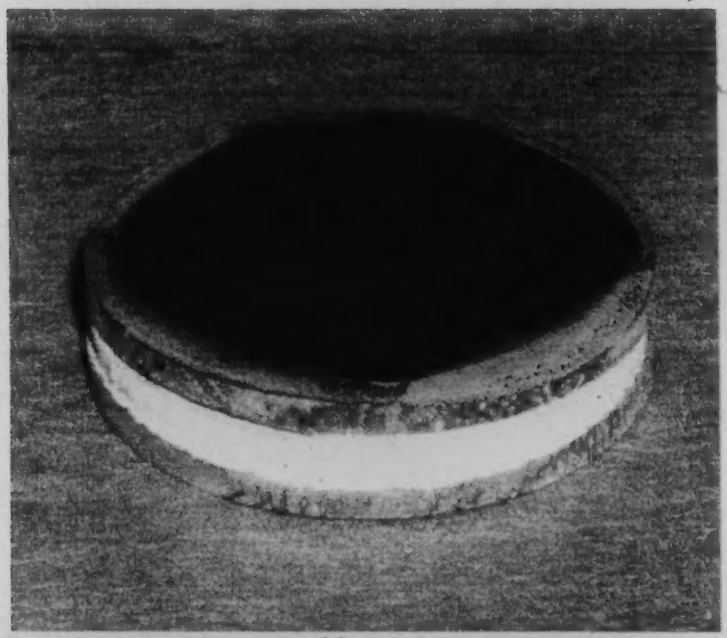

(a)

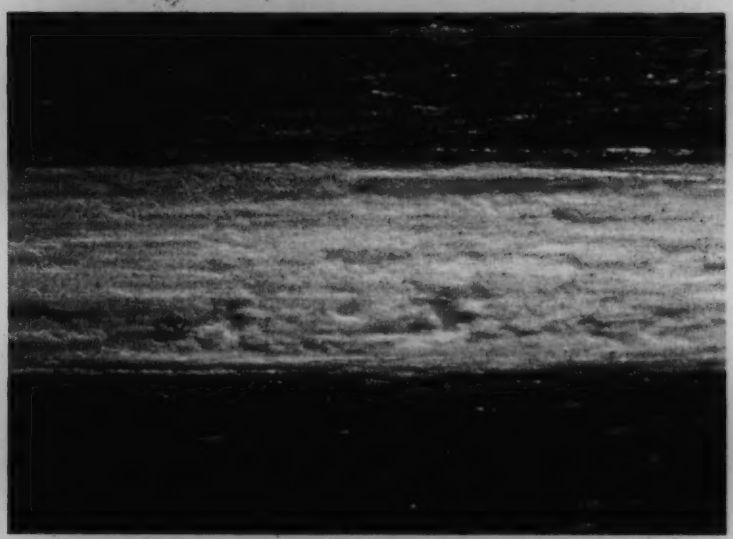

(b)

Figure 2-12. Sandwich disk sintered at 800°C. (a) Perspective view of the sandwich disk; (b) Cross-section of the sandwich disk

2.3.2.2 Chemical and mechanical compatibility

The chemical composition of an intimate mixture of BCY and $LiNaSO_4$ powders before and after sintering at 800°C was determined using XRD analysis (Figure 2-13). The microstructure of the BCY/$LiNaSO_4$ layers' interface in the sandwich disk was examined using a Hitachi S-2700 scanning electron microscope (Figure 2-14).

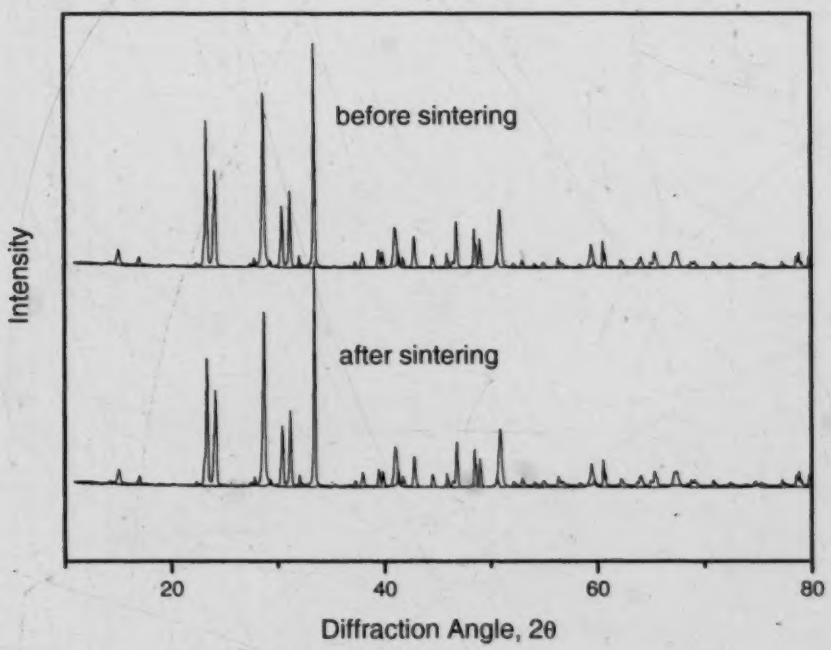

Figure 2-13. XRD profiles of the mixture of BCY and $LiNaSO_4$ powder before and after sintered at 800°C for 8 h.

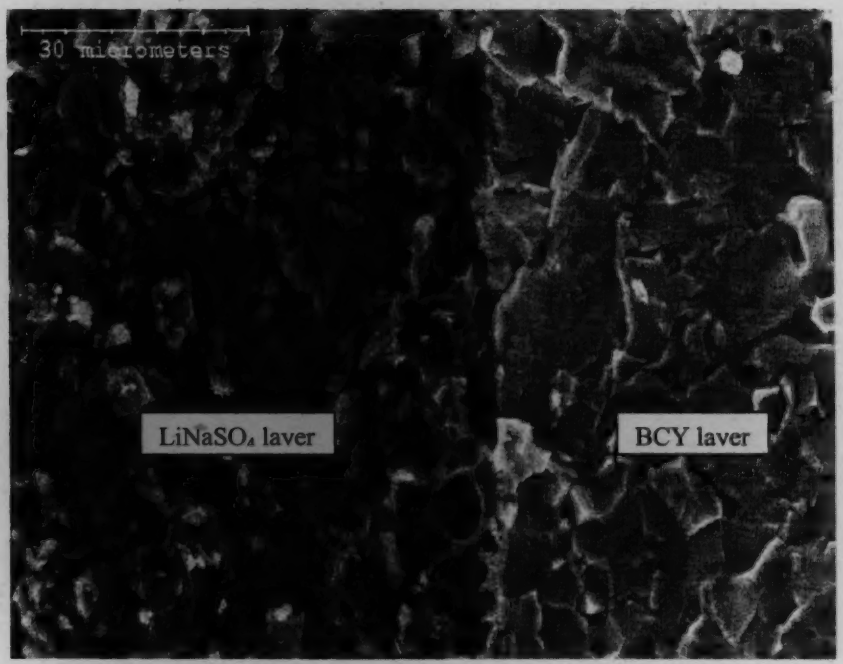

Figure 2-14. Microstructure of cross section of $LiNaSO_4$/BCY layers interface.

2.3.2.3 Conductivity measurements

Current interruption technique and electrochemical impedance spectroscopy (EIS) measurements [35] were performed to determine the conductivities of sandwich disks and BCY disks independently, using a Solartron electrochemical measurement system (SI-1287) in the following fuel cell configuration:

$$H_2|\ Pt\ |\ \text{electrolyte disk}\ |\ Pt\ |\ O_2$$

In EIS measurements, the frequency region was 0.1–100,000 Hz and a stimulating ac signal of 5 mV was imposed under OCV conditions. Current interruption technique was used to obtain the ohmic resistances of the electrolyte disks. The basic principle of the current interruption method is to interrupt the current and to observe the resulting voltage transient [36]. The ohmic part of the overpotentials is separated from the

electrochemical losses by taking advantage of the fact that the ohmic losses vanish faster than the electrochemical overpotentials when the current is interrupted [37]. The ohmic loss was the difference between the voltages immediately before and after the current interruption.

The fuel cell set-up system was the same as described previously (Figure 2-3).

2.3.3 Results and Discussion

XRD profiles of a well-mixed mixture of BCY and $LiNaSO_4$ powder before and after sintering in air at 800°C for 8 h (Figure 2-13) showed that there was no reaction between BCY and $LiNaSO_4$ at 800°C. Thus, the materials were stable and chemically compatible for use in the sandwich.

SEM micrograph (Figure 2-14) of fresh sandwich disks showed that the $LiNaSO_4$ layer was in strong and intimate contact with BCY across the entire interface between the layers. Thus, the three layers of BCY and $LiNaSO_4$ in the sandwich disk so prepared were physically compatible.

The BCY layers of the sandwich disk prevented direct exposure of $LiNaSO_4$ to hydrogen or oxygen, and so the $LiNaSO_4$ layer was stable during testing in a hydrogen concentration cell or operation in H_2-O_2 fuel cells at high temperatures [38].

The XRD spectra and SEM micrograph of used sandwich disks were identical to those of fresh disks, showing that there were no chemical or physical changes during testing. Thus, the materials did not react with each other or with hydrogen under testing conditions.

The proton conductivities of the sandwich disk and BCY disk were measured separately in the fuel cell using hydrogen as the fuel and Pt as the anode and cathode electrodes at operating temperatures in the range 600-680°C. Current interruption technique was used to determine the proton conductivities of sandwich disk because the $LiNaSO_4$ layer was a mixed ionic conductor and ac impedance spectroscopy cannot isolate conduction contribution by Li^+ and Na^+. Figure 2-15 shows the interruption of the current and immediately response of voltage at 600°C. The sharp change in voltage corresponds to the ohmic loss, and the slow change corresponds to non-ohmic polarization losses (activation and concentration). The proton conductivities (σ_1) of the sandwich disk in the fuel cell were then calculated from the ohmic losses obtained from the current interruption method. For measurements of proton conductivities of BCY disk, ac impedance spectroscopy could be used because the BCY disk was almost a pure proton conductor under the fuel cell conditions. Figure 2-16 shows the impedance spectra at 600°C under open circuit conditions and the conductivities of BCY (σ_2) were determined from data in Figure 3-6 and the respective dimensions of the disk.

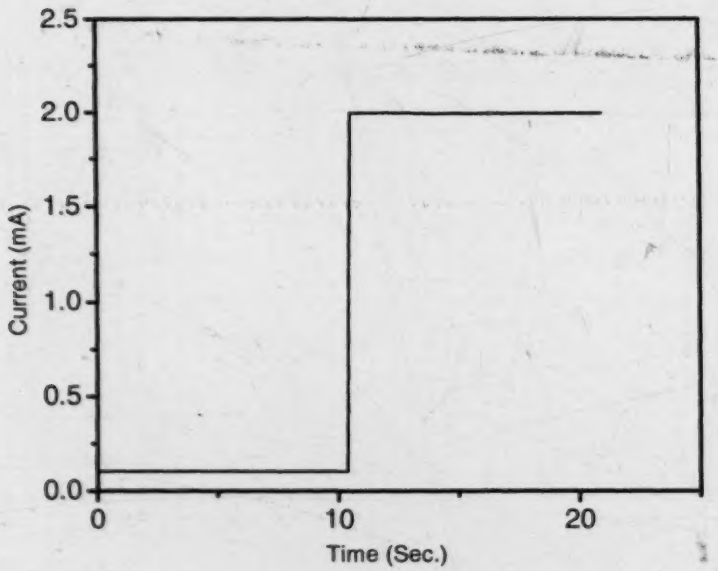

(a)

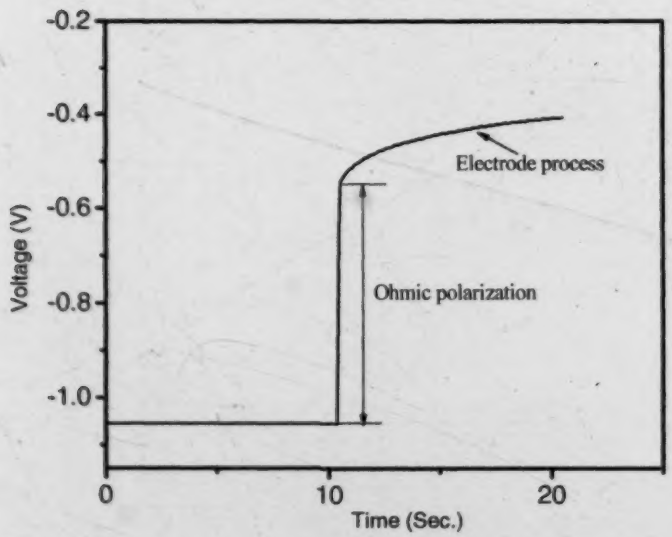

(b)

Figure 2-15. Conductivities measurement for the cell with electrolyte of sandwich disk at 600°C using current interruption method. (a) Interruption of current. (b) Response of the voltage.

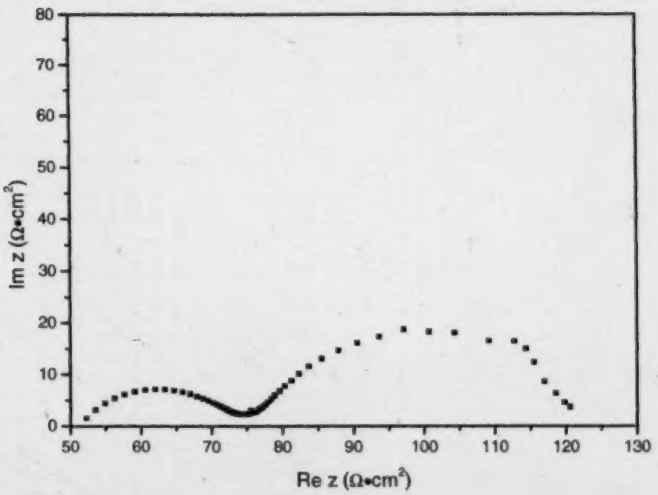

Figure 2-16. Impedance spectra for the cells with electrolyte of BCY disk at 600°C under open circuit conditions.

The sandwich disk was modeled as resistors in series (Figure 2-17) comprising two layers of BCY and one layer of $LiNaSO_4$ in the fuel cell circuit. R_1 was the resistance of proton mobility in the $LiNaSO_4$ layer and R_2 was the resistance in BCY layer in the sandwich disk. The value of R was obtained from the measured BCY layer resistance R_2 and the total resistance of the sandwich disk (R_2+R_1+R_2). The respective conductivities were then calculated from the corresponding resistances and cross-sectional areas. The proton conductivity of $LiNaSO_4$ σ was then calculated using formula (2-17),

$$\sigma = \frac{L_1 * \sigma_1 * \sigma_2}{\sigma_2 * (2 * L_2 + L_1) - 2 * L_2 * \sigma_1} \qquad (2\text{-}17)$$

where L_1 and L_2 are thicknesses of the $LiNaSO_4$ layer and BCY layer, respectively.

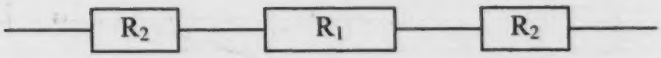

Figure 2-17. Equivalent circuit for the sandwich disk in fuel cells.

Calculated values of the proton conductivities of $LiNaSO_4$ and BCY at different temperatures are summarized (Table 2-1) and compared with literature values for the total conductivities of $LiNaSO_4$ [27]. At 600°C, the proton conductivity of $LiNaSO_4$ was about 7.01×10^{-3} $S \cdot cm^{-1}$, which is only about 5.6% of the total conductivity of $LiNaSO_4$ at 600°C (1.25×10^{-1} $S \cdot cm^{-1}$) and is lower than that of BCY (1.75×10^{-2} $S \cdot cm^{-1}$ [39]) at the same temperature. Thus, the total ionic conductivity of $LiNaSO_4$ is mostly attributable to conduction of Li^+ and Na^+, and proton conduction contributes a much smaller portion. It is clear that the proton conductivity of $LiNaSO_4$ in H_2-O_2 fuel cells is not more than 10% of the total ionic conductivity throughout the 600-680°C range.

Table 2-1. Conductivities of $LiNaSO_4$ and BCY15 at 600-680°C.

Temperature /°C	Total conductivity of $LiNaSO_4$ / $S \cdot cm^{-1}$ [8]	Proton conductivity of $LiNaSO_4$/ $S \cdot cm^{-1}$	Proton conductivity of BCY / $S \cdot cm^{-1}$
600	1.25×10^{-1}	7.01×10^{-3}	1.75×10^{-2}
650	1.30×10^{-1}	1.12×10^{-2}	2.00×10^{-2}
680	1.35×10^{-1}	1.23×10^{-2}	2.38×10^{-2}

The values for proton conductivity of $LiNaSO_4$ can explain the previous experimental results obtained using fuel cells with $LiNaSO_4$ and BCY as electrolytes [4,27,39]. When pure propane was the anode feed and was converted to propylene

through electrochemical dehydrogenation (Eqn. 2-18) at the fuel cell anode, the maximum power density and current density obtained at 600°C from fuel cells using $LiNaSO_4$ as electrolyte with Pt as electrodes were 10 $mW \cdot cm^{-2}$ and 25 $mA \cdot cm^{-2}$, respectively.

$$C_3H_8 \rightarrow C_3H_6 + 2H^+ + 2e^- \qquad (2\text{-}18)$$

However, under the same operating conditions the maximum power density and current density from fuel cells using BCY as electrolyte were 28 $mW \cdot cm^{-2}$ and 60 $mA \cdot cm^{-2}$, respectively (Table 2-2), even though the total ionic conductivity of $LiNaSO_4$ was almost seven times higher than the conductivity of BCY under those fuel cell operating conditions. Although the total ionic conductivity of $LiNaSO_4$ was higher than that of BCY, its proton conductivity was considerably lower than that of BCY under the same fuel cell conditions. Thus, the reduced performance of the fuel cell with $LiNaSO_4$ as electrolyte compared to that with BCY as electrolyte is due to the difference in proton conductivity.

Table 2-2. Comparison of performances of fuel cells with $LiNaSO_4$ and BCY as electrolytes.

Electrolyte	Electrodes	Ionic conductivity / $S \cdot cm^{-1}$	Fuel	T/°C	Max. power density /$mA \cdot cm^{-2}$	Max. current density /$mA \cdot cm^{-2}$
$LiNaSO_4$	Pt, Pt	1.25×10^{-1}	C_3H_8	600	10	25
BCY15	Pt, Pt	1.75×10^{-2}	C_3H_8	600	28	60

2.4 Conclusions

A time dependence of the OCV and conductivity of $LiNaSO_4$ was found when $LiNaSO_4$ was employed as solid electrolyte in a H_2-O_2 fuel cell at intermediate temperatures. Thermodynamic analysis indicated that $LiNaSO_4$ was not chemically stable in hydrogen at high temperature, which was confirmed by XRD analysis. $LiNaSO_4$ reacted with H_2 at the fuel cell operating temperature, and Na_2S, LiOH and NaOH were produced. Therefore, $LiNaSO_4$ is not chemically stable in the hydrogen-containing atmosphere at high temperatures, and thus is not suitable as a proton-conducting electrolyte in the fuel cell for propane dehydrogenation.

A method has been developed for measuring the proton conductivity of reducible electrolytes, and in particular $LiNaSO_4$, using fuel cells. A sandwich disk is prepared in which the outer layers are a non-reducible proton conductor. The outer layers block Li^+ and Na^+ conduction in $LiNaSO_4$ and allow only H^+ transport through the disk. SEM and XRD analysis showed that there was good chemical and mechanical compatibility between materials in sandwiches comprising two layers of BCY and an interposed layer of $LiNaSO_4$. The proton conductivity of $LiNaSO_4$ in H_2-O_2 fuel cells contributed only 5-10% to total ionic conductivity at 600-680°C. These data are consistent with experimental results that fuel cells using $LiNaSO_4$ as electrolyte have much lower current and power density when compared with fuel cells using proton conducting electrolytes such as BCY under the same conditions, even though the total ionic conductivity of $LiNaSO_4$ is much higher.

References:

[1] K.D. Kreuer, "Proton-conducting oxides", *Annual Review of Materials Research*, 33, 333-336 (2003).

[2] B. Zhu, X. Liu and T. Schober, "Novel hybrid conductors based on doped ceria and BCY20 for ITSOFC applications", *Electrochemical Communication*, 6, 379-383 (2004).

[3] B. Zhu, I. Albinsson, B.E. Mellander and G.Y. Meng, "Intermediate-temperature proton-conducting fuel cells - present experience and future opportunities", *Solid State Ionics*, 125, 439-446 (1999).

[4] B. Heed, B. Zhu, B.E. Mellander and A. Lundén, "Proton conductivity in fuel cells with solid sulfate electrolytes", *Solid State Ionics*, 46, 121-125 (1991).

[5] A. Demin and P. Tsiakaras, "Thermodynamic analysis of a hydrogen fed solid oxide fuel cell based on a proton conductor", *International Journal of Hydrogen Energy*, 26, 1106-1108 (2001).

[6] M. Schulze, M. Lorenz, N. Wagner, and E. Gulzow. "XPS analysis of the degradation of Nafion", *Fresenius' Journal of Analytical Chemistry*, 365, 106-113 (1999).

[7] D.E. Moilanen, I.R. Piletic, M.D. Fayer, "Water dynamics in Nafion fuel cell membranes: the effects of confinement and structural changes on the hydrogen bond network", *Journal of Physical Chemistry C*, 111 (25), 8884-8891 (2007).

[8] R.B. Lin, S.M. Shih, "Cyclic voltammetric measurement of catalyst surface area for Pt-black/ Nafion electrodes", *Journal of the Chinese Institute of Chemical Engineers*, 37 (4), 311-319 (2006).

[9] M.P. Godino, V.M. Barragan, J.P.G. Villaluenga, C. Ruiz-Bauza, B. Seoane, "Water and methanol transport in Nafion membranes with different cationic forms", *Journal of Power Sources*, 160 (1), 181-186 (2006).

[10] T. Hibino, A. Hashimoto, M. Suzuki, M. Sano, "A solid oxide fuel cell using Y-doped $BaCeO_3$ with Pd-loaded FeO anode and $Ba_{0.5}Pr_{0.5}CoO_3$ cathode at low temperatures", *Journal of Electrochemical Society*, 149, A1503-A1507 (2002).

[11] H. Iwahara, H. Uchida, K. Morimoto, S. Hosogi, "High-temperature C1-gas fuel cells using proton-conducting solid electrolytes", *Journal of Applied Electrochemistry*, 19 (3), 448-52 (1989).

[12] H. Iwahara, H. Uchida, S. Tanaka, "High temperature-type proton conductive solid oxide fuel cells using various fuels", *Journal of Applied Electrochemistry*, 16 (5), 663-8 (1986).

[13] H. Iwahara, H.Uchida, N.Maeda, "High-temperature fuel and steam electrolysis cells using proton conductive solid electrolytes", *Journal of Power Sources*, 7 (3), 293-301 (1982).

[14] D. Hassan, S.Janes, R.Clasen, "Proton-conducting ceramics as electrode/electrolyte materials for SOFC's - Part I: preparation, mechanical and thermal properties of sintered bodies", *Journal of the European Ceramic Society*, 23 (2), 221-228 (2002).

[15] A. Lunden, "Enhancement of cation mobility in some sulfate phases due to a paddle-wheel mechanism", *Solid State Ionics*, 28-30, 163-167 (1988).

[16] M. Zhang, A. Putnis, E.H. Salje, "Infrared spectroscopy of superionic conductor LiNaSO4. Vibrational modes and thermodynamics", *Solid State Ionics*, 177 (1-2), 37-43 (2006).

[17] H. Feldmann, R.E. Lechner, D. Wilmer, "Unusual fast cation conduction in the high-temperature phase of lithium sodium sulfate", *Materials Research Society Symposium Proceedings*, 756, 81-86 (2003).

[18] B.M. Suleiman, A. Lunden, E. Karawacki, "Heat transfer and ion migration in the system Li_2SO_4-Na_2SO_4", *Solid State Ionics*, 136-137, 325-330 (2000).

[19] H. Iwahara, "High temperature proton conductors based on perovskite-type oxides", *Chemistry of Solid State Materials*, 2, 122-137 (1992).

[20] K.S. Knight, N. Bonanos, "The crystal structures of some doped and undoped alkaline earth cerate perovskites", *Materials Research Bulletin*, 30 (3), 347-56 (1995).

[21] W. Suksamai, I.S. Metcalfe, "Measurement of proton and oxide ion fluxes in a working Y-doped $BaCeO_3$ SOFC", *Solid State Ionics*, 178 (7-10), 627-634 (2007).

[22] R. Haugsrud, T. Norby, "Proton conduction in rare-earth ortho-niobates and ortho-tantalates", *Nature Materials*, 5 (3), 193-196 (2006).

[23] A. Tomita, T. Hibino, M. Sano, "Surface modification of a doped $BaCeO_3$ to function as an electrolyte and as an anode for SOFCs", *Electrochemical and Solid-State Letters*, 8 (7), A333-A336 (2005).

[24] A. Lunden, "Evidence for and against the paddle-wheel mechanism of ion transport in superionic sulfate phases", *Solid State Communications*, 65 (10), 1237-40 (1988).

[25] E.A. Secco, "Ion transport in sulfates: percolation mechanism versus paddle-wheel mechanism", *Solid State Communications*, 66 (9), 921-923 (1988).

[26] A. Lunden, "Ionic conduction in sulfates", *Applied Sciences*, 250, 181-201 (1993).

[27] S.W. Tao, B. Zhu, D.K. Peng, G.Y. Meng, "Investigation on $LiNaSO_4$-Al_2O_3 ceramics as electrolytes for H_2/O_2 fuel cells", *Materials Research Bulletin*, 34, 1651-1659 (1999).

[28] S.W. Tao, Q.Y. Wu, D.K. Peng, G.Y. Meng, "Electrode materials for intermediate temperature proton-conducting fuel cells", *Journal of Applied Electrochemistry*, 30, 153-157 (2000).

[29] S.W. Tao, Z.L Zhan, P.Wang, G.Y. Meng, "Chemical stability study of Li_2SO_4 on the operation condition of a H_2/O_2 fuel cell", *Solid State Ionics*, 116, 29-33 (1999).

[30] I. Barin, and O. Knacke, *Thermochemical Properties of Inorganic Substances*, p.568-715, Germany (1973).

[31] C.K. Cheng, "Application of PBI membrane polymer fuel cell for conversion of hydrocarbon", *Masters Thesis*, University of Alberta, pp.120-149 (2004).

[32] L.P. Cook and H.F. Mcmurdie, *Phase Equilibria Diagrams*, p.53, The American Ceramic Society, the United States (1987).

[33] R.D. Brittain, K.H. Lau, D.L. Hildenbrand, "Effusion studies of the decomposition of copper (II) sulfate and copper (II) oxide copper (II) sulfate", *Journal of Physical Chemistry*, 93 (13), 5316-5319 (1989).

[34] G. Marchal, "A study of the thermal decomposition of sulfates", *Journal de Chimie Physique et de Physico-Chimie Biologique*, 22, 493-517 (1925).

[35] M.A. Dissanayake, B.-E. Mellander, "Phase diagram and electrical conductivity of the Li_2SO_4-Li_2CO_3 system", *Solid State Ionics*, 21, 279-285 (1986).

[36] F.N. Büchi, A. Marek, G. Scherer, "In situ membrane resistance measurements in polymer electrolyte fuel cells by fast auxiliary current pulses", *Journal of the Electrochemical Society*, 142, 1895-1901 (1995).

[37] J. Li, J.L. Luo, K.T. Chuang, A.R. Sanger, "Proton conductivity and chemical stability of Li_2SO_4 based electrolyte in a H_2S–air fuel cell", *Journal of Power Sources*, 160 (2), 909-914 (2006).

[38] R.D.Carneim, T.R.Armstrong, "Chemical stability of barium cerate-based high-temperature proton conductors", in *Metals & Ceramics Division*, Abstracts of Papers, 225th ACS National Meeting, New Orleans, LA, March 23-27, 2003, paper FUEL-137.

[39] H.Iwahara, H.Uchida, K.Ono, K.Ogaki, "Proton conduction in sintered oxides based on barium cerate ($BaCeO_3$)", *Journal of the Electrochemical Society*, 135, 529-533 (1988).

CHAPTER 3

CONVERSION OF PROPANE TO PROPYLENE IN A PROTON-CONDUCTING FUEL CELL USING Y-DOPED $BaCeO_3$ AS ELECTROLYTE

3.1 Introduction

Using proton-conducting fuel cells for propane dehydrogenation to produce propylene is a novel process having many interesting characteristics [1,2,3,4], and from this process value-added product propylene and electricity power can be obtained simultaneously.

As will be shown, there are several advantages specific to this process, and so there has been extensive discussion on the concept of dehydrogenation of alkanes to alkenes in a proton-conducting fuel cell [5,6,7,8,9]. However, relatively little work has been conducted to achieve this fuel cell application because of challenges in finding suitable proton-conducting electrolytes and compatible electrodes operating at intermediate temperatures. Some perovskite-type oxides (e.g. $BaCeO_3$ and $SrCeO_3$ based compounds) and some sulphates (e.g. $LiNaSO_4$ and Li_2SO_4) were studied intensively for use as proton-conducting electrolytes [10,11,12,13,14,15], especially the former. The perovskite-type oxides contain no significant concentrations of protons within the host component but, through doping with aliovalent cations (ions with different oxidation state), which give rise to electron holes and oxygen ion vacancies, they can incorporate

protons via equilibrium reactions with hydrogen or humidity from the atmosphere, involving defects in the oxide lattice:

$$V_O^{\cdot\cdot} + \frac{1}{2}O_2 \leftrightarrow O_O^{\times} + 2h^{\cdot} \qquad (3\text{-}1)$$

$$H_2O + 2h^{\cdot} \leftrightarrow 2H_i^{\cdot} + \frac{1}{2}O_2 \qquad (3\text{-}2)$$

$$H_2 + 2h^{\cdot} \leftrightarrow 2H_i^{\cdot} \qquad (3\text{-}3)$$

where $V_O^{\cdot\cdot}$, $O_O^{\times}$, $H_i^{\cdot}$ and $h^{\cdot}$ are oxygen vacancy, oxide ion at normal lattice site, proton and hole respectively [11,16,17,18,19,20]. By the so-called "hopping mechanism", protons travel by sequentially bonding to successive lattice oxide ions to form OH^- bonds, as illustrated in Figure 3-1. Among materials of this kind, $BaCeO_3$-based oxides have almost the highest proton conductivities, especially for 15% Y-doped $BaCeO_3$ (BCY15) [21,22,], which is due to the high lattice constants and very small deviation from the ideal cubic perovskite structure of $BaCeO_3$ [23,24,25,26,27]. Although $LiNaSO_4$ and Li_2SO_4 were reported to show even higher total conductivities under fuel cell conditions [12,28], the contribution from proton conductivity in these sulphates was lower than that in $BaCeO_3$-based compounds [29]. In addition, recent studies [30,31] showed that both $LiNaSO_4$ and Li_2SO_4 were not chemically stable in hydrogen-containing fuel cell atmospheres, so they are not suitable for use as proton-conducting electrolytes in fuel cells for propane dehydrogenation.

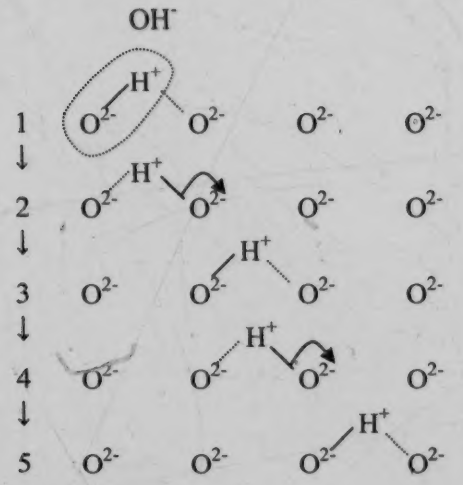

Figure 3-1. Illustration of proton migration "hopping" in a perovskite type oxide.

In this study, the suitability of Y-doped $BeCeO_3$ as protonic electrolytes in the C_3H_8-O_2 fuel cell and the feasibility of converting propane to propylene in fuel cells with perovskite type oxide electrolyte were investigated. Platinum was used as the electrodes.

3.2 Experimental

3.2.1 Electrolyte

The preparation of 15% Y-doped $BaCeO_3$ electrolyte membranes involved synthesizing Y-doped $BaCeO_3$ powder by solid-state reactions, and then making electrolyte solid disks from the powder. First, prescribed amounts of $BaCO_3$ (99.9%, Aldrich), CeO_2 (99.9%, Aldrich), and Y_2O_3 (99.99%, Koch) were ground together and intimately mixed in iso-propanol using a planetary ball mill (Fritsch P-5) with a zirconia mill container and zirconia balls at 120 rpm. for 24 h. Then the mixture was dried and

sintered in air at 1550°C for 15 h to produce a single-phase Y-doped $BaCeO_3$ compound. The synthesized Y-doped $BaCeO_3$ was ground again at 160 rpm. for 24 h. The composition and crystallinity of the product were determined using a Rigaku Rotaflex X-ray diffractometer. The powder was pressed into a pellet 1 mm thick and 20 mm in diameter which was then sintered at 1600°C for 10 h to make a dense electrolyte disk. Disk surfaces were polished using abrasive papers (220 grit) until the thickness was reduced to about 0.7 mm. The surface morphology and microstructure of the resulting BCY15 electrolyte disks were determined using a Hitachi S-2700 scanning electron microscope (SEM).

3.2.2 Electrodes

Platinum was used as the cathode and anode catalysts because platinum is active and stable in oxidative and reductive atmospheres. It is also an active catalyst for propane dehydrogenation [2,3,4,32,33,34,35,36,37]. The electrodes were prepared by screen-printing platinum paste (Heraeus CL11-5100) onto the corresponding surfaces of the BCY15 electrolyte disk. The platinum paste was dried in air at 120°C for 30 min and then fired at 1000°C for 60 min to remove the organic binder and to increase adhesion to the electrolyte. The superficial surface area of each electrode was approximately 0.7 cm^2.

3.2.3 Fuel cell system fabrication

The fuel cell system was similar to that described in Chapter 2, but of smaller size (Figure 3-2; outer tube: O.D. of 1.0 cm and I.D. of 0.8 cm; inner tube: O.D. of 0.7 cm and I.D. of 0.5 cm) due to smaller size of BCY15 electrolyte disk, caused by significant shrinkage when sintered at high temperatures. After the cell had stabilized at a selected

temperature under nitrogen in each compartment, the anode and cathode feeds were switched from nitrogen to propane and oxygen, respectively. Pure C_3H_8 (Praxair, grade 2.0) and O_2 (Praxair, grade 2.6) were fed into the anode and cathode compartments via the inner tube respectively, and spent gases exited via the gas outlet in the outer tube.

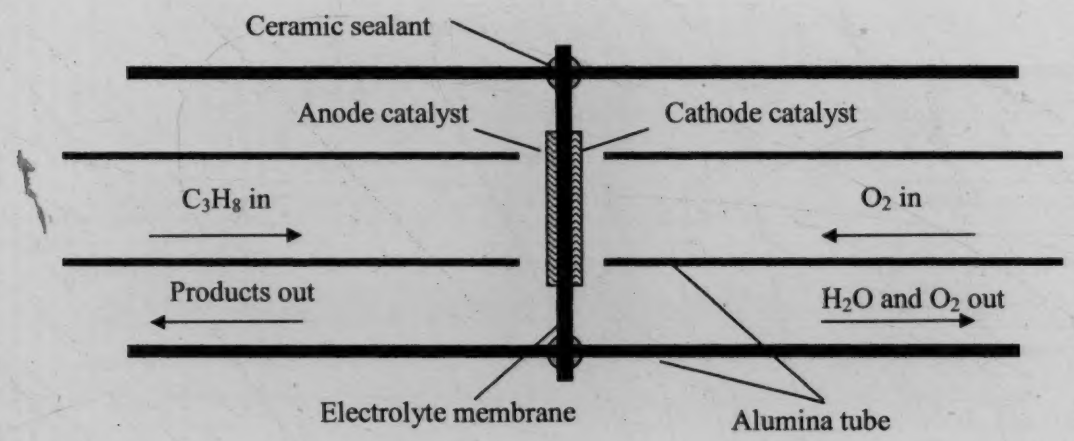

Figure 3-2. Schematic of high temperature fuel cell set-up with ceramic sealant (Aremco 503).

3.2.4 Electrical Measurements and Gas Analysis

The open circuit voltage, overpotential and impedance spectrum between the two electrodes were measured using a Solartron 1287 electrochemical interface together with 1255B frequency response analysis instrumentation. AC impedance spectra were measured for frequencies between 0.01 Hz and 1 MHz to determine the conductivity of each membrane. Current-voltage characteristics were determined potentiodynamically with the electrochemical systems using a scanning rate of 5 mV/s. The relation between spectra and conductivity of electrolyte is described in ref. 29.

Gas analysis of the anode effluent streams performed during fuel cell experiments was performed to identify the extent of electrochemical and chemical reactions taking place at the anode as well as gas products distribution. A gas chromatograph (Hewlett-Packard Model 5890 II), using a Polypack column at 80°C and a thermal conductivity detector (TCD) was employed to determine the concentration of anode outlet gas stream. Hewlett-Packard ChemStation software was utilized for data acquisition and chromatogram analysis. This software enabled simultaneous data acquisition and processing on a computer workstation.

Calibration was done with the standard gases which included propane, propylene, ethane, ethylene, hydrogen and methane. Table 3-1 gives one example of standard gas composition (except hydrogen), as well as retention time of each gas species, the area of peak responding to each gas species, and the calculated response factors when using helium as the carrier gas. These response factors were relative values, adopting the response factor for propane as unity. The average response factors calculated from four different standard gas compositions were used to calculate the concentration of each gas component. The calibration of hydrogen was conducted separately in the same GC under the same conditions except using argon as carrier gas. The relationship between hydrogen concentration and area of GC peak is approximately linear for hydrogen concentrations not exceeding 8% (APPENDIX-A), which is the range of hydrogen concentration in the fuel cell system under operating temperatures 600-700°C.

Table 3-1. Calibration with a standard gas.

Standards	Specified concentration (v %)	Retention time (Sec.)	Peak area (μV·sec)	Response factors
Methane	15	0.976	93960	3.26
Ethylene	5	2.316	74542	1.37
Ethane	10	2.919	159516	1.28
Propylene	20	8.968	388954	1.05
Propane	50	10.012	1021031	1.00

Based on the inlet and outlet gas concentrations, the conversion, selectivity and yield were defined as:

$$Conversion = \frac{n_{feedin} - n_{feedout}}{n_{feedin}} \quad (3\text{-}4)$$

$$Selectivity = \frac{n_{product}}{n_{feedin} - n_{feedout}} * \frac{C_{product}}{C_{propane}} \quad (3\text{-}5)$$

$$Yield = \frac{n_{product}}{n_{feedin}} * \frac{C_{product}}{C_{propane}} \quad (3\text{-}6)$$

n_{feedin}: moles of propane feed in;

$n_{feedout}$: moles of propane in the effluent;

$n_{product}$: moles of product in the effluent;

$C_{product}$: carbon atoms per molecule presented in the product (3 for propylene);

$C_{propane}$: carbon atoms per molecule of propane (3 for propane).

3.3 Results and discussion

3.3.1 BCY15 Electrolyte

3.3.1.1 Properties

The identity and high crystallinity of the synthesized BCY15 after sintering at 1600°C was confirmed by the X-ray diffraction pattern (Figure 3-3). Disks formed by pressing BCY15 included a dense mass of cubic crystals (Figure 3-4). The bulk density of the electrolyte disks was very close to the density of solid BCY15 powder (6.01g/cm^3 for the disks v.s. 6.12 g/cm^3 for the bulk material).

The proton transport number in the BCY15 electrolyte was determined by hydrogen concentration cell/EMF method described by Heed, et al [6]. It was found to be above 0.95 at the temperature range 550~700°C using the following concentration cell:

Pure H_2 (Praxair, PP 4.5) | Pt | BCY15 electrolyte | Pt | 10% H_2 (balance with Ar)

The conductivity of BCY15 electrolyte in a C_3H_8-O_2 fuel cell at different operating temperatures is shown in Figure 3-5. This material showed very high protonic conductivity at high temperatures. Above 600°C, it attained ~10^{-2} S/cm.

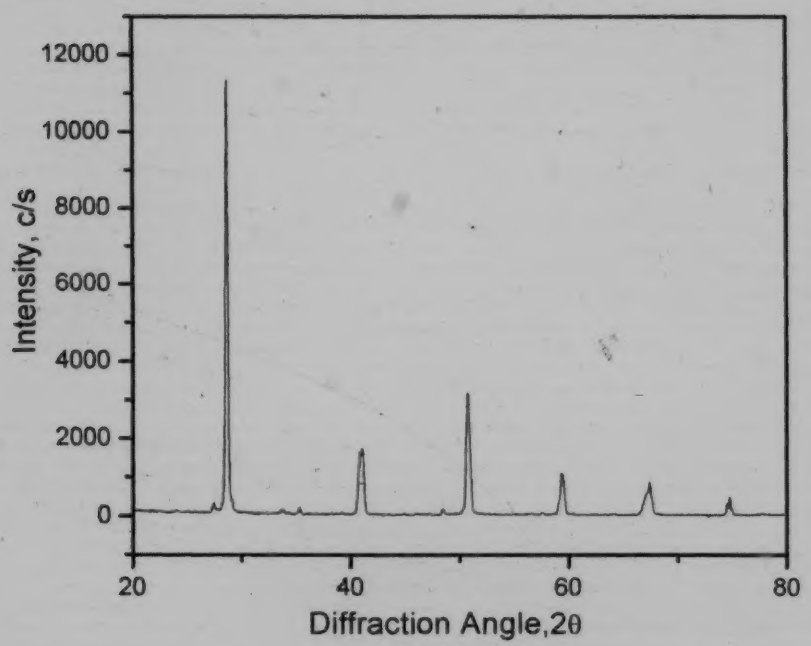

Figure 3-3. XRD of $BaCe_{0.85}Y_{0.15}O_{3-\alpha}$ powder after sintering at 1600°C.

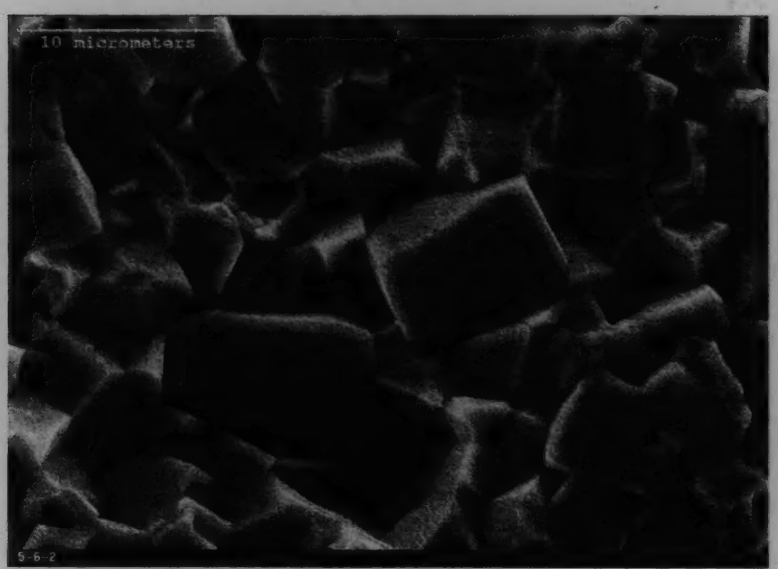

Figure 3-4. SEM of surface of BCY15 electrolyte.

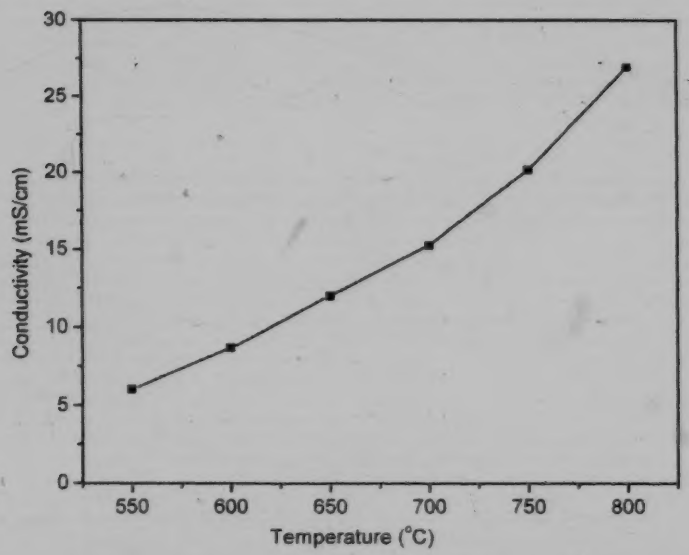

Figure 3-5. Temperature dependence of conductivity in BCY15 in C_3H_8-O_2 fuel cell.

3.3.1.2 Stability tests of the electrolyte, and analysis

The conductivity of the electrolyte Y-doped $BaCeO_3$ in a C_3H_8–O_2 fuel cell with platinum as the electrodes was recorded at 650°C for 40 h (Figure 3-6). There was no significant change in conductivity over the short-term testing period on stream. A 120 h stability test of the electrolyte Y-doped $BaCeO_3$ was also conducted at 650°C using AC impedance analysis. In this case, the conductivity of Y-doped $BaCeO_3$ at the end of the test had decreased to one-quarter of the value measured within the initial 1 h. SEM imaging showed some small white crystals had formed on the anode side surface of electrolyte membrane (Figure 3-7), especially on the area near the sealant that was not covered by platinum. The white crystals had different structures from the cubic perovskite phase of Y-doped $BaCeO_3$, and EDX analysis showed the composition of the white crystals (point 2) had a different ratio of Ba atoms to Ce atoms when compared to

an area (point 1) that had substantially the same composition as fresh Y-doped $BaCeO_3$ samples (Figure 3-8). It appeared that the white crystals on the anode side surface of electrolyte were due to reactions of Y-doped $BaCeO_3$ with the anode atmosphere, because the same phenomenon was not observed on the cathode side surface.

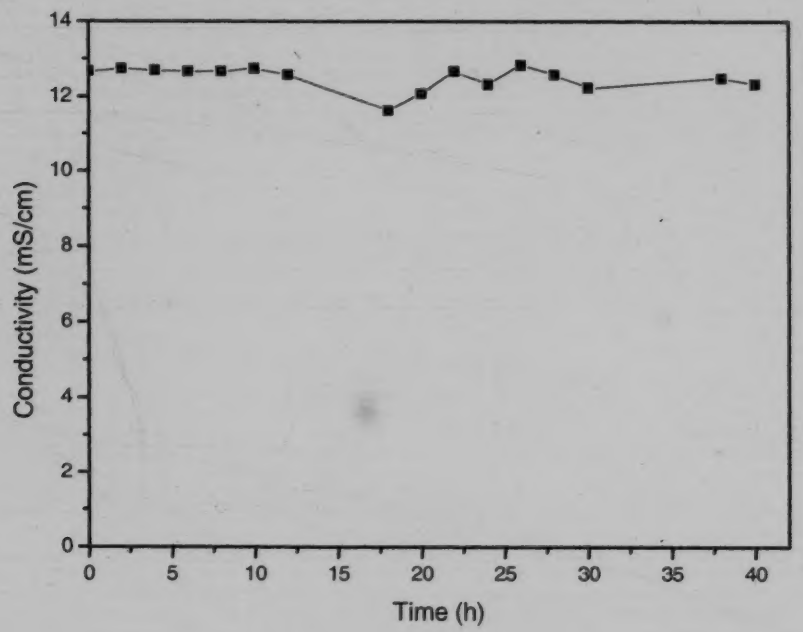

Figure 3-6. Conductivity as a function of exposure time under open circuit conditions at 650°C with propane flow rate 80 mL/min.

Figure 3-7. Microstructures of anode side surface of Y-doped $BaCeO_3$ electrolyte after 120 h test.

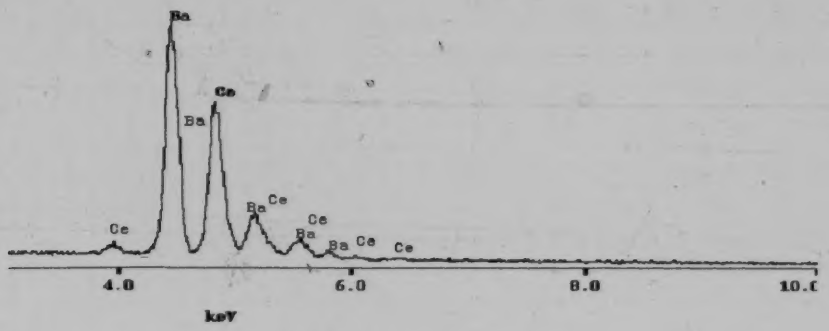

(a)

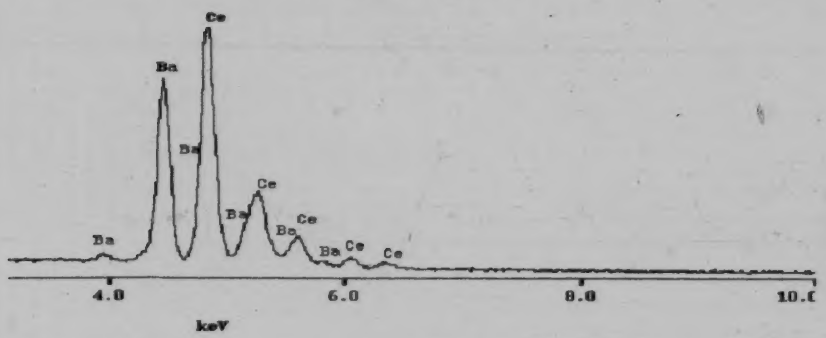

(b)

Figure 3-8. EDX profiles of anode side surface of Y-doped $BaCeO_3$ electrolyte after 120 h test (corresponding to Figure 5-7). (a) Point 1; (b) Point 2).

A separate test of stability of Y-doped $BaCeO_3$ electrolyte samples in propane was conducted in a quartz tube at 650°C over 120 h. XRD analyses showed that there was no reaction between the electrolyte and propane (Figure 3-9). In addition, the white crystals seen in Figure 3-7 were not detected using SEM. Thus, the electrolyte material appeared to be chemically stable in propane at 650°C. However, under fuel cell testing conditions, a low concentration of carbon oxides (~ 2%) was detected by GC at the anode side, which appeared to be arising from oxidation of anode fuel by small amounts of oxygen that diffused through the sealant, which became porous after it was sintered (Figure 3-

10). Consequently, it was concluded that degradation of Y-doped $BaCeO_3$ electrolyte under fuel cell conditions was caused by the reactions of the material with small amounts of CO_2 at the anode side. It has been shown that barium cerate reacts with CO_2 at temperatures below 1100°C to form $BaCO_3$ [38,39]. In the present application, the electrolyte was a dense material in an atmosphere containing a relatively low partial pressure of CO_2. Consequently, it was anticipated that reaction with CO_2 to form $BaCO_3$ would be slow, and that it would occur primarily at the surface, especially at the area near the ceramic sealant.

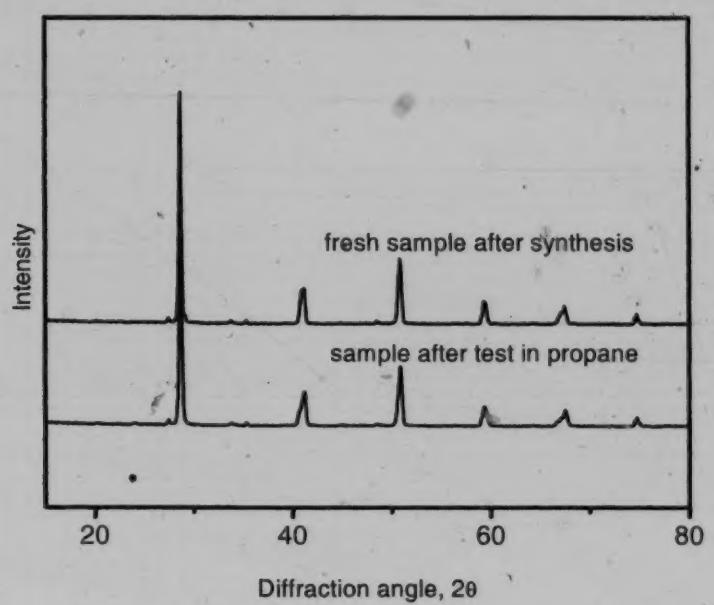

Figure 3-9. XRD profiles of electrolyte BCY15 disk before and after test in propane for 120 h.

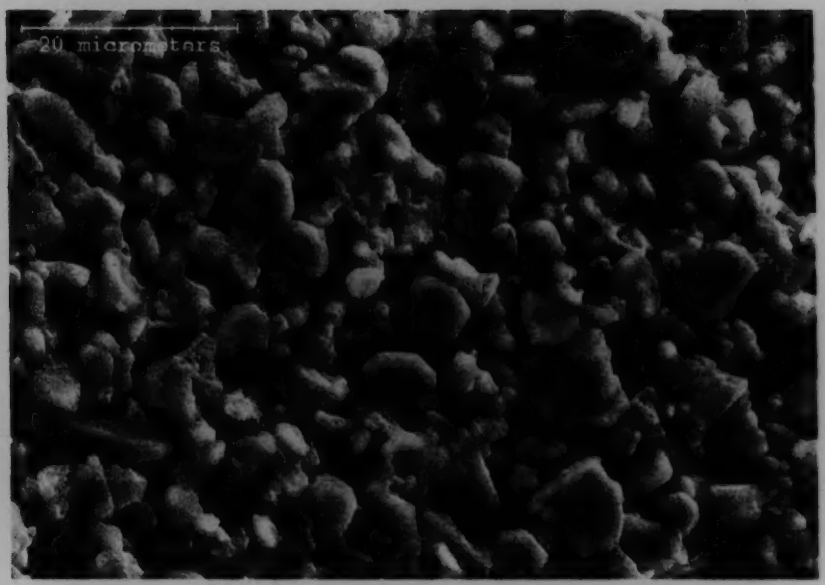

Figure 3-10. Microstructure of ceramic sealant (Aremco 503) after sintering at 650°C in the fuel cell.

To prevent formation of carbon oxides in the anode atmosphere and thereby enhance the stability of Y-doped $BaCeO_3$ electrolyte under C_3H_8–O_2 fuel cell conditions, it was necessary to modify the fuel cell set-up and to replace the ceramic sealant that was prone to becoming porous. Although it was recognized that oxide ion conductivity of Y-doped $BaCeO_3$ at 650°C [40] could lead to a low concentration of CO_2 and contribute to white $BaCO_3$ crystal formation, it was determined that this was not a significant source of CO_2 since there were no white crystals formed at the anode electrode surface when a superior sealant was used.

3.3.1.3 New fuel cell set-up designs

To prevent deterioration of the electrolyte by reaction with carbon oxides caused by porous sealant at high temperatures, several commercially available ceramic sealants

were tested as substitutes for Aremco 503. Unfortunately all of them became porous to some degree after sintering at high temperatures. Recently, a high quality seal was achieved using very fine glass particles. When cured at the designated temperature (>850°C), the sealant melted and then formed a contiguous seal as the temperature was reduced to the fuel cell operating temperature. Figure 3-11 shows the microstructure of the glassy coating so formed, which obviously is very dense and without any holes or cracks. However, a new setup having a vertical furnace stand needed to be used to avoid leakage of the melted sealant when curing at the designated temperature (Figure 3-12). Because the cathode side atmosphere was oxygen, the ceramic sealant could still be used, and it had no obvious influence on the stability of the electrolyte in the $C_3H_8 - O_2$ fuel cell.

Figure 3-11. Microstructure of glass sealant after sintering at 650°C in the fuel cell.

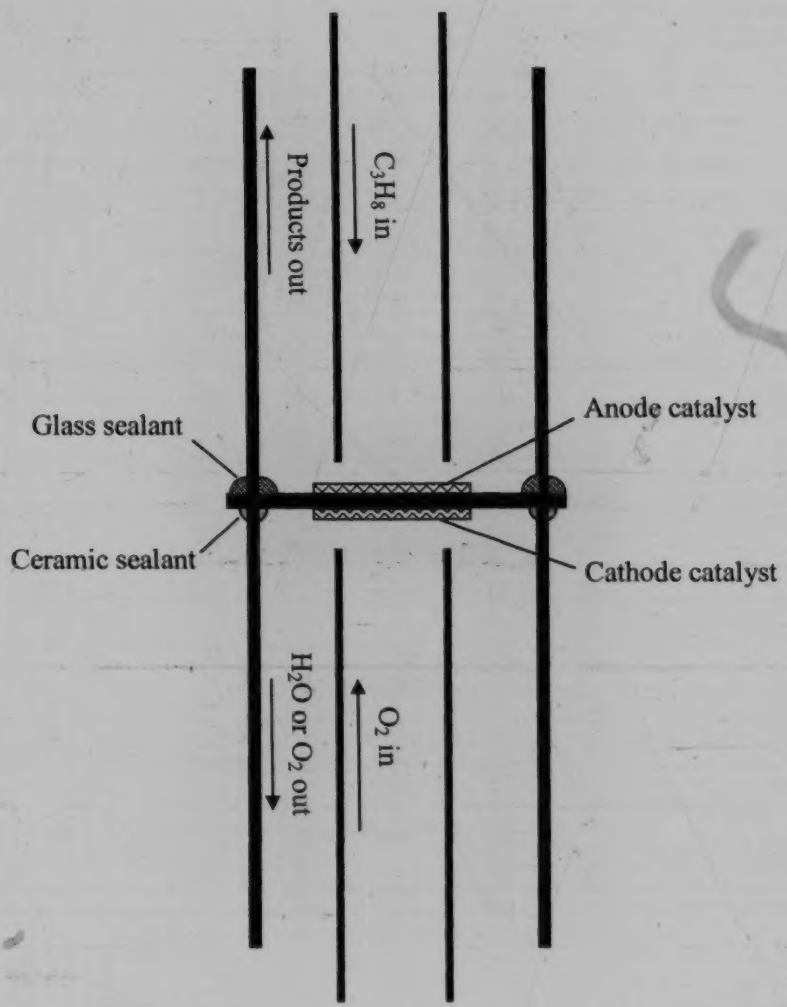

Figure 3-12. Schematic diagram of revised high temperature fuel cell set-up with vertical design.

The performance of the glass sealant in the vertical set-up was tested by measuring the concentrations of carbon oxides and nitrogen in the anode chamber effluent. From GC analysis, the amount of CO, and even traces of CO_2, indicated the extent of leakage of oxygen into the anode chamber. Oxygen could react with fuel to form only oxides of carbon or mixtures containing water vapor. In the latter case, the

water vapor so formed still can interact with the hydrocarbons to form carbon oxides by shift reactions. Under the operating conditions (temperature: 600–700°C and propane flow rate: 50-200 mL/min), the total concentrations of carbon oxides and nitrogen were limited to values below 30 ppm.

In addition to the vertical fuel cell set-up design, a horizontal set-up was developed by revising the original design (Figure 3-13). By putting the fuel cell set-up into a big glass tube filled with flowing argon, diffusion of oxygen into the anode chamber through porous ceramic sealant was suppressed. GC analysis showed the concentrations of carbon oxides and nitrogen in the anode chamber of this set-up were almost at the same level as in the vertical set-up.

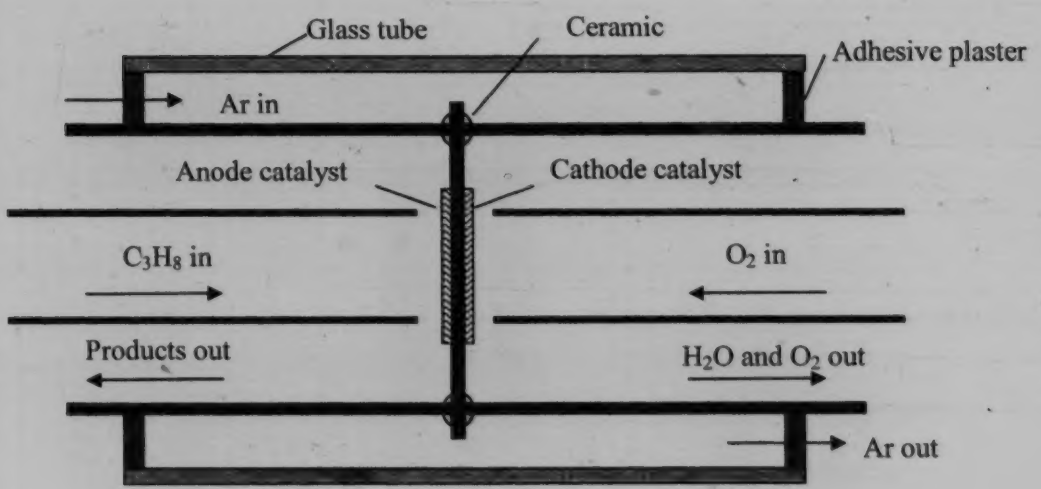

Figure 3-13. Schematic of revised horizontal high temperature fuel cell set-up.

3.3.1.4 Stability of Y-doped $BaCeO_3$ electrolyte using the revised fuel cell design

Additional 120 h stability tests of Y-doped $BaCeO_3$ electrolyte in a C_3H_8–O_2 fuel cell were conducted under the same operating conditions as previous tests. There were no extensive reactions with CO_2, and thus no adverse effects on the electrolyte, as reflected in the sustainability of conductivity of the electrolyte and correspondingly stable fuel cell performance. AC impedance analysis demonstrated that there was no apparent degradation of conductivity of the electrolyte over time, and Figure 3-14 showed that the conductivities measured in the initial 1 h and after 120 h were similar. No white crystals were found on the anode side surface by SEM analysis after the test (Figure 3-15).

So the chemical stability of Y-doped $BaCeO_3$ electrolyte in $C_3H_8 - O_2$ was greatly improved through developing the new fuel cell set-up designs with suitable sealants to prevent the air diffusion. The following tests were conducted in the vertical fuel cell system.

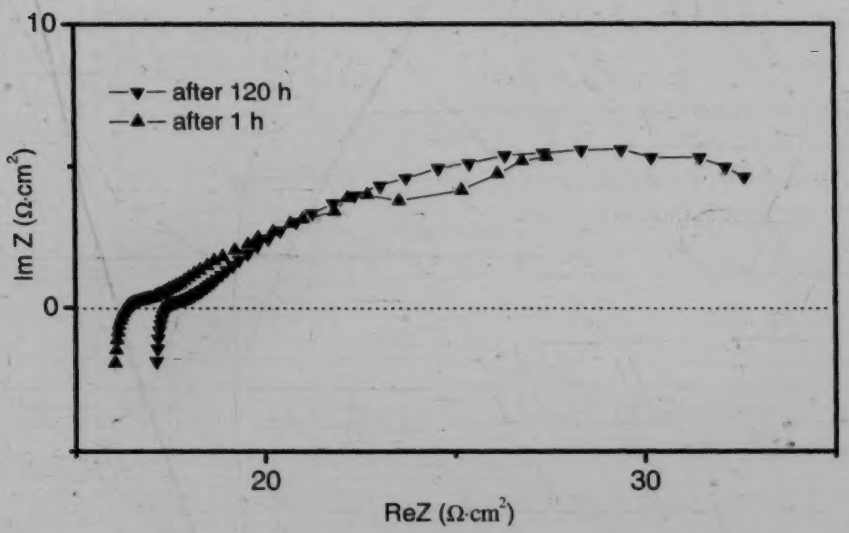

Figure 3-14. AC impedance spectra of C_3H_8–O_2 fuel cell based on Y-doped $BaCeO_3$ electrolyte.

Figure 3-15. Microstructure of anode side surface of Y-doped $BaCeO_3$ electrolyte after 120 h test in revised fuel cell design.

3.3.2 Analysis of anode outlet gas

3.3.2.1 Open circuit conditions

Ideally, the anode outlet products should be only propylene and unreacted propane. However, in addition to propane dehydrogenation some other side reactions can also occur in the anode chamber, especially under open circuit conditions. Under this condition, there was no current drawn from the fuel cell, so the gas products were only caused by catalytic reactions and some thermal reactions rather than electro-catalytic dehydrogenation. A studies [41] has shown that reactions of propane primarily involved two pathways on some dehydrogenation catalysts: dehydrogenation and cracking.

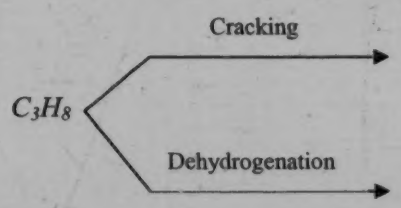

$$C_3H_8 \xrightarrow{\text{Cracking}} CH_4 + C_2H_4 \qquad (3\text{-}7)$$

$$C_3H_8 \xrightarrow{\text{Dehydrogenation}} C_3H_6 + H_2 \qquad (3\text{-}8)$$

The two parallel reactions are not independent, and are in competition with each other via absorbed intermediates on the catalyst surface [42]. Thermodynamic analysis also indicated that the products of the two reactions interacted and secondary reactions occurred among them. For example, ethane could also exist as the product of hydrogenation of ethylene:

$$C_2H_4 + H_2 \rightarrow C_2H_6 \qquad (3\text{-}9)$$

In addition, at high temperatures the hydrocarbons easily form carbon in an irreversible process, especially via alkenes [43]:

$$1/nC_nH_{2n} \rightarrow C + H_2 \qquad (3\text{-}10)$$

So, under open circuit conditions, all these factors make the reactions and the products very complex. C_3H_6, CH_4, C_2H_4, C_2H_6 and H_2 were detected in the effluent stream by gas chromatography at the anode outlet. Compared to C_3H_6, CH_4 and C_2H_4, the concentrations of C_2H_6 and H_2 were much less, especially H_2. The reason for the low concentrations of C_2H_6 and H_2 was that C_2H_6 was the product of a secondary reaction and H_2 was mostly consumed in secondary reactions. Therefore, C_3H_6, CH_4 and C_2H_4 were the predominant gas products. The gas distributions at different operating temperatures and different propane flow rates are shown in Figures 3-16 and 3-17. It was obvious that, from testing under open circuit conditions, thermal reactions were less selective to propylene than electrochemical processes (section 3.3.2.2).

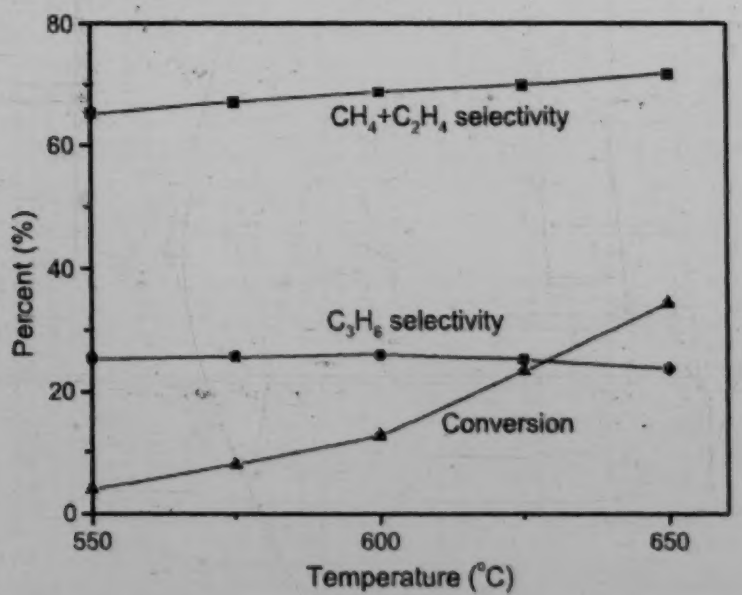

Figure 3-16. Propane conversion and selectivities to C_3H_6 and $CH_4 + C_2H_4$ at different operating temperatures under open circuit conditions (propane flow rate: 20 mL/min).

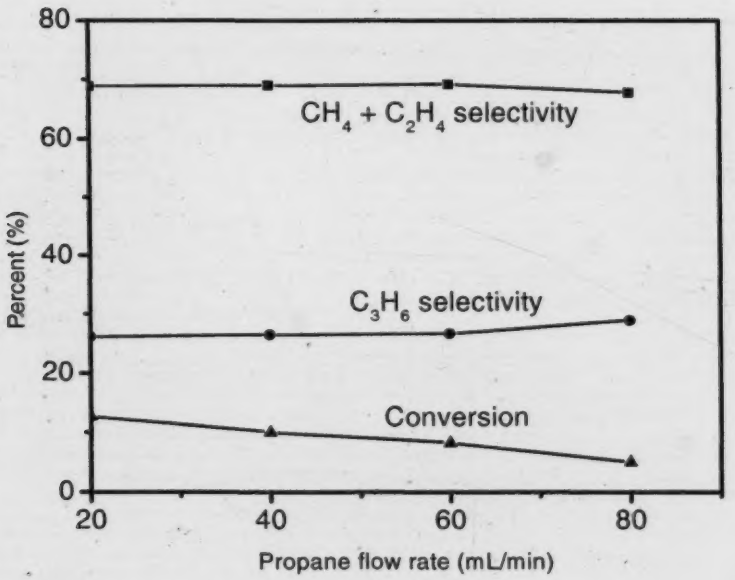

Figure 3-17. Propane conversion and selectivities to C_3H_6 and $CH_4 + C_2H_4$ at different propane flow rates under open circuit conditions (600°C).

3.3.2.2 Discharging fuel cells

The occurrence of some thermal reactions could not be avoided even when drawing current from the fuel cell because the two hollow coaxial fuel cell tubes provided space to enable thermal reactions to occur. However, discharging fuel cells obviously improved the gas distribution through activation of the electro-catalytic reaction.

Figure 3-18 shows propane conversion and selectivities of C_3H_6 and the combination of CH_4 and C_2H_4 at different discharging current densities (i.e. closed circuit). Compared to the open circuit condition (zero discharging current density), the selectivity of propylene increased by 6% at a discharging current density of 40 mA/cm^2 with propane flow rate of 10 mL/min and operating temperature of 600°C. Discharging

the fuel cell improved propane dehydrogenation by conducting hydrogen atoms through the proton conducting electrolytes. On the other hand, the reactions of propane intramolecular C-C bond breaking were inhibited during fuel cell discharging, and the total selectivity of CH_4 and C_2H_4 apparently decreased. The propane conversion slightly increased with discharging the fuel cell, but at low discharging current density (e.g.10 mA/cm^2 in Figure 3-18) propane conversion was below the level of the open circuit conditions. This phenomenon may be due to the suppression of the reactions of propane involving intramolecular C-C bond breaking and other side reactions during discharging the fuel cell. With the further increase of discharging current density, propane dehydrogenation became more important and the total conversion increased.

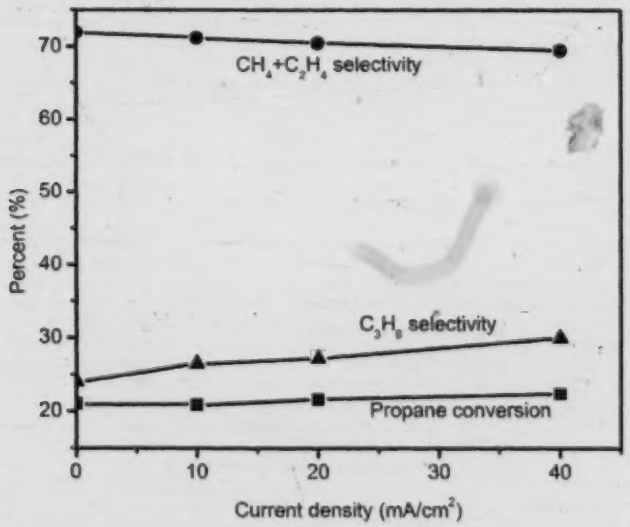

Figure 3-18. Propane conversion and selectivities of C_3H_6 and $CH_4 + C_2H_4$ at different discharging current density (600°C, propane flow rate: 10 mL/min and effective electrode area: 0.7 cm^2).

To analyze the impact of reaction parameters on the process of electro-catalytic dehydrogenation to propylene, side reactions that occurred to a significant degree only at the open circuit conditions were excluded, and only the electro-catalytic reaction was correlated with discharging current density. Figure 3-19 shows the propylene yield arising from electro-catalytic dehydrogenation during discharging the fuel cell. Propylene yield obtained from experiments was a little less than the theoretical values, which were calculated based on Faraday's Law for the anode side reaction (detailed calculation in APPENDIX-B).

$$C_3H_8 \rightarrow C_3H_6 + 2H^+ + 2e^- \qquad (2\text{-}18)$$

Hence these data indicated that, during the process of discharging fuel cell, some other side reactions in addition to propane dehydrogenation also occurred on the anode catalysts and a portion of hydrogen ion transported through the protonic electrolyte was contributed by these side reactions.

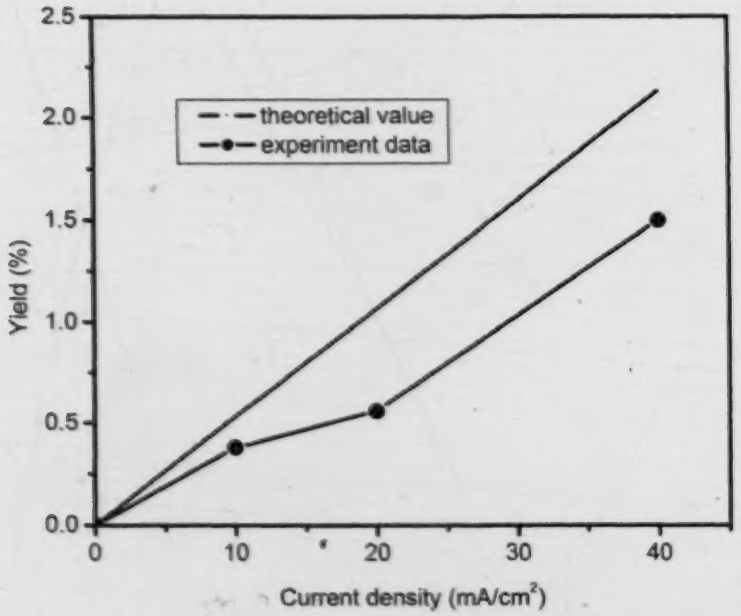

Figure 3-19. Propylene yield by electro-catalytic dehydrogenation at different discharging current density (600°C, propane flow rate: 10 mL/min and effective electrode area: 0.7 cm^2).

3.3.3 Fuel cell performance

Figure 3-20 shows the current density as a function of cell voltage and power density for the $C_3H_8 - O_2$ fuel cell at a propane flow rate of 10 mL/min at 600 and 650°C. The current density increased quasilinearly with decrease in potential generated, and even in the high current density region there was no apparent slope deviation, showing that mass transfer was not a limitation for the system [44]. At the same propane flow rate, the fuel cell performance strongly depended on operating temperature. The maximum power density doubled, from about 17 mW/cm^2 at 600°C to 35 mW/cm^2 at 650°C. The maximum current density also increased, from 85 to 176 mA/cm^2. The position of the peak increased from 44 to 73 mA/cm^2. The cause of this behavior was that the higher

temperature not only facilitated propane dehydrogenation but also increased the proton conductivity of the electrolyte.

Propane flow rate also influenced the performances of C_3H_8–O_2 fuel cell. At 600°C when the propane flow rate was increased from 10 mL/min to 30 mL/min the maximum current density and power density also slightly increased (Figure 3-21). When the propane flow rate was increased the residence time was decreased, a lower proportion of the propane was converted, and so there was higher average propane concentration in the anode compartment, thus the reaction rate of propane dehydrogenation also accelerated.

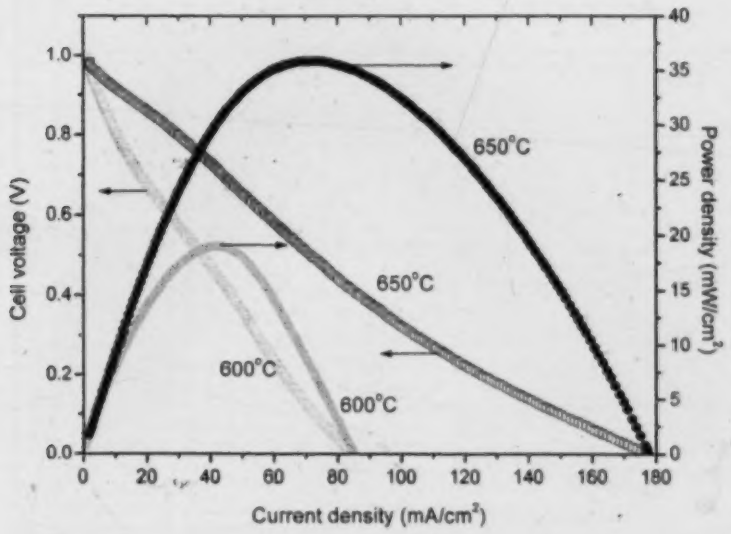

Figure 3-20. Discharge properties of C_3H_8-O_2 fuel cell using BCY15 electrolyte at 600°C and 650°C with propane flow rate of 10 mL/min (thickness of electrolyte: 0.7 mm).

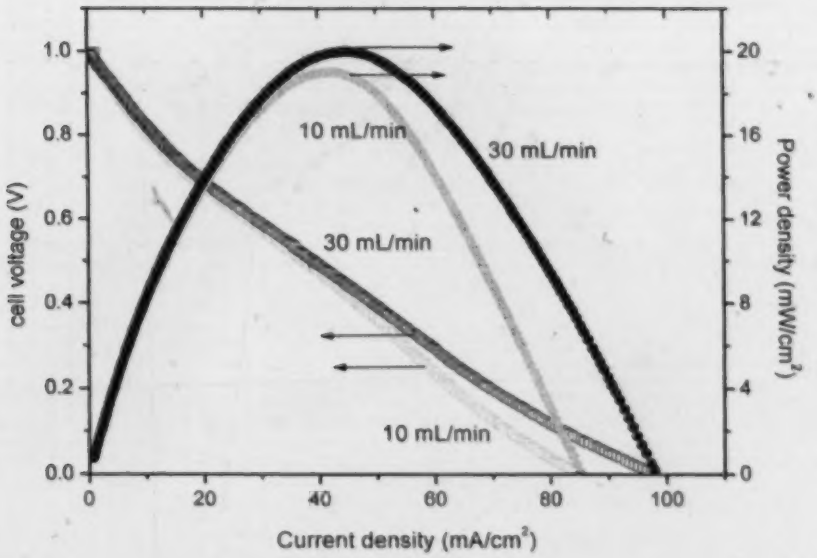

Figure 3-21. Discharge properties of C_3H_8-O_2 fuel cell using BCY15 electrolyte at 600°C with propane flow rate of 10 and 30 mL/min (thickness of electrolyte: 0.7 mm).

3.4 Conclusions

Conversion of propane to propylene in a proton-conducting fuel cell when using 15% Y-doped $BaCeO_3$ as electrolyte and platinum as anode and cathode is feasible. High selectivity to propylene as well as good fuel cell performances are obtained by electro-catalytic dehydrogenation of propane in the proton-conducting solid oxide fuel cell.

The 15% Y-doped $BaCeO_3$ protonic electrolyte shows high proton conductivity in the fuel cell at high temperatures, but its chemical stability deteriorates under fuel cell operating conditions due to reaction with carbon oxides arising from oxidation of anode fuel by small amounts of oxygen that diffuse through the ceramic sealant. The concentration of carbon oxides in the fuel cell anode atmosphere is dramatically reduced

through use of an improved fuel cell set-up design and use of a glass sealant, which dramatically improves the stability of performance of Y-doped $BaCeO_3$ as electrolyte in C_3H_8–O_2 fuel cells. So Y-doped $BaCeO_3$ is suitable for use as the protonic electrolyte for use in C_3H_8–O_2 fuel cells.

References:

[1] C.K. Cheng, "Application of PBI membrane polymer fuel cell for conversion of hydrocarbon", *Masters Thesis*, University of Alberta, 120-129 (2004).

[2] Y. Feng, J. Luo, S. Wang, J. Melnik, K.T. Chuang, "Investigation of Y-doped $BaCeO_3$ as electrolyte in propane fueled proton conducting solid oxide fuel cell", *Proceedings of the International Symposium on Fuel Cell and Hydrogen Technologies*, Editor: D. Ghosh, Calgary, Canada, Aug. 21-24, pp.461- 471 (2005).

[3] Y. Feng, J. Luo, K.T. Chuang, "Conversion of propane to propylene in a proton-conducting solid oxide fuel cell", *Fuel*, 86, 123-128 (2007).

[4] Y. Feng, J. Luo, K.T. Chuang, "Analysis and improvement of chemical stability of Y-doped $BaCeO_3$ as proton conducting electrolytes in C_3H_8 - O_2 fuel cells", *Journal of New Materials for Electrochemical Systems*, 10 (3), 147-152 (2007).

[5] B. Zhu, I. Albinsson, B.E. Mellander, G.Y. Meng, "Intermediate-temperature proton-conducting fuel cells - present experience and future opportunities", *Solid State Ionics*, 125, 439-446 (1999).

[6] B. Heed, B. Zhu, B.E. Mellander, A. Lundén, "Proton conductivity in fuel cells with solid sulfate electrolytes", *Solid State Ionics*, 46, 121-125 (1991).

[7] J.H. White, M. Schwartz, A.F. Sammells, "Solid state proton and electron mediating membrane and use in catalytic membrane reactors", *United States Patent*, No. 6,281,403 B1, Aug. 28 2001.

[8] W.G. Barker, B.S. Berland, M. Schwaartz, L. Simpson, J. Armstrong, "Apparatus and method for the design and manufacture of thin-film electrochemical devices", *United States Patent*, No. 6,772,501 B2, Aug.10 2004.

[9] D.J. Edllund, D.T. Friesen, "Hydrogen-permeable composite metal membrane and uses thereof", *United States Patent*, No.5, 217,506, Jun. 08 1993.

[10] H. Iwahara, T. Esaka, H. Uchida, N. Maeda, "Proton conduction in sintered oxides and its application to steam electrolysis for hydrogen production", *Solid State Ionics*, 3-4, 359-363 (1981).

[11] H. Uchida, H. Yoshikawa, T. Esaka, S. Ohtsu, "Formation of protons in strontium cerium oxide ($SrCeO_3$)-based proton conducting oxides. Part II. Evaluation of proton concentration and mobility in ytterbium-doped $SrCeO_3$", *Solid State Ionics*, 36, 89-95 (1989).

[12] S.W. Tao, B. Zhu, D.K. Peng and G.Y. Meng, "Investigation on $LiNaSO_4$-Al_2O_3 ceramics as electrolytes for H_2/O_2 fuel cells", *Materials Research Bulletin*, 34, 1651-1659 (1999).

[13] B. Zhu, I. Albinsson, B.E. Mellander and G.Y. Meng, "Intermediate-temperature proton-conducting fuel cells - present experience and future opportunities", *Solid State Ionics*, 125, 439-446 (1999).

[14] B. Zhu, X. Liu and T. Schober, "Novel hybrid conductors based on doped ceria and BCY20 for ITSOFC applications", *Electrochemical Communications*, 6, 378-383 (2004).

[15] B. Heed, B. Zhu, B.E. Mellander and A. Lundén, "Proton conductivity in fuel cells with solid sulfate electrolytes", *Solid State Ionics*, 46, 121-125 (1991).

[16] E. Kendrick, M.S. Islam and P.R. Slater, "Developing apatites for solid oxide fuel cells: insight into structural, transport and doping properties", *Journal of Materials Chemistry*, 17 (30), 3104-3111(2007).

[17] T. Shimura, H. Tanaka, H. Matsumoto, and T. Yogo, "Influence of the transition-metal doping on conductivity of a $BaCeO_3$ -based protonic conductor", *Solid State Ionics*, 176 (39-40), 2945-2950 (2005).

[18] T. Higuchi, T. Tsukamoto, S. Yamaguchi, S. Shin, T. Hattori, "Spectroscopic analysis of perovskite -type protonic conductor", *Materials Integration*, 18 (7), 28-36 (2005).

[19] J. Wu, R.A. Davies, M.S. Islam, S.M. Haile, "Atomistic study of doped $BaCeO_3$: site-selectivity and cation nonstoichiometry", *Chemistry of Materials*, 17 (4), 846-851 (2005).

[20] A.L. Samgin, "Doping effects on protonic conduction in $SrCeO_3$- and $BaCeO_3$ -based perovskites", *Inorganic Materials*, 36 (8), 816-819 (2000).

[21] T. Takahashi, H. Iwahara, "Ionic conduction in perovskite-type oxide solid solution and its application to the solid electrolyte fuel cell", *Energy Conversion*, 11, 105-111 (1971).

[22] W.F. Chu, F.J. Rohr, "Catalytic reduction of nitric oxide in flue gas", *Solid State Ionics*, 28-30, 1540-6 (1988).

[23] K.D. Kreuer, "Proton-conducting oxides", *Annual Review of Materials Research*, 33, 333-336 (2003).

[24] S. Yamaguchi, N. Yamada, "Thermal lattice expansion behavior of Yb-doped $BaCeO_3$", *Solid State Ionics*, 162-163, 23-29 (2003).

[25] H.C. Gupta, P. Ashdhir, "Lattice dynamic investigation of the phonon wavenumbers of $BaCeO_3$ perovskite", *Journal of Raman Spectroscopy*, 30 (1), 65-67 (1999).

[26] W. Muench, G. Seifert, K.D. Kreuer, J. Maier, "A quantum molecular dynamics study of proton conduction phenomena in $BaCeO_3$", *Solid State Ionics*, 86-88, 647-652 (1996).

[27] K.S. Knight, N. Bonanos, "Space group and lattice constants for barium cerate and minor corrections to the crystal structures of $BaCe_{0.9}Y_{0.1}O_{2.95}$ and $BaCe_{0.9}Gd_{0.1}O_{2.95}$", *Journal of Materials Chemistry*, 4 (6), 899-901 (1994).

[28] S.W. Tao, Q.Y. Wu, D.K. Peng and G.Y. Meng, "Electrode materials for intermediate temperature proton-conducting fuel cells", *Journal of Applied Electrochemistry*, 30, 153-157 (2000).

[29] Y. Feng, J. Luo, K.T. Chuang. "A method to measure the proton conductivity of $LiNaSO_4$ under fuel cell conditions", *Journal of the Electrochemical Society*, 153 (6), A1049-A1052 (2006).

[30] S.W. Tao, Z.L Zhan, P. Wang, G.Y. Meng, "Chemical stability study of Li_2SO_4 on the operation condition of a H_2/O_2 fuel cell", *Solid State Ionics*, 116, 29-33 (1999).

[31] Y. Feng, J. Luo, K.T. Chuang, "Chemical stability of $LiNaSO_4$ electrolyte during operation in a H_2-O_2 fuel cell", *Journal of the Electrochemical Society*, 153 (5), A865-A868 (2006).

[32] Y.W. Zhang, Y. Zhou, A. Qiu, Y. Wang, Y. Xu, P. Wu, "Propane dehydrogenation on PtSn/ZSM-5 catalyst: Effect of tin as a promoter", *Catalysis Communications*, 7 (11), 860-866 (2006).

[33] C. Yu, Q. Ge, H. Xu, W. Li, "Effect of Cr promoter on the performance of Pt-Sn/-Al_2O_3 catalyst for propane dehydrogenation", *Ranliao Huaxue Xuebao*, 34 (2), 209-213 (2006).

[34] S.B. Kogan, M. Herskowitz, "Selective propane dehydrogenation to propylene on novel bimetallic catalysts", *Catalysis Communications*, 2 (5), 179-185 (2001).

[35] H.P. Rebo, E.A. Blekkan, L. Bednarova, A. Holmen, "Deactivation of Pt-Sn catalyst in propane dehydrogenation", *Studies in Surface Science and Catalysis*, 126, 333-340 (1999).

[36] Z. Xu, A. Hu, T. Zhang, J. Xia, L. Lin, "Effects of the catalyst preparation conditions on the performance of catalytic dehydrogenation reaction for light hydrocarbon", *Tianranqi Huagong*, 20 (6), 16-19 (1995).

[37] O.A. Bariaas, A. Holmen, E.A. Blekkan, "Propane dehydrogenation over supported platinum catalysts: The influence of tin on the coking properties", *Studies in Surface Science and Catalysis*, 88, 519-524 (1994).

[38] D. Shima, S.M. Haile, "The influence of cation non-stoichiometry on the properties of undoped and gadolinia-doped barium cerate", *Solid State Ionics*, 97, 443-455 (1997).

[39] N. Bonanos, K.S. Knight, B. Ellis, "Perovskite solid electrolytes: Structure, transport properties and fuel cell applications", *Solid State Ionics*, 79, 161-170 (1995).

[40] T. Hibino, A. Hashimoto, M. Suzuki, M. Yano, S. Yoshida, M. Sano, "A solid oxide fuel cell using Y-doped $BaCeO_3$ with Pd-loaded FeO anode and $Ba_{0.5}Pr_{0.5}CoO_3$ cathode at low temperatures", *Journal of the Electrochemical Society*, 149, 195-200 (2002).

[41] S.Y. Yu, "Coupling alkane dehydrogenation reactions with hydrogenation reactions on cation-modified H-ZSM5", *Ph.D. Dissertation*, University of California, Berkeley (2001), pp.8-30.

[42] E. Heracleous, A.A. Lemonidou, "Homogeneous and heterogeneous pathways of ethane oxidative and non-oxidative dehydrogenation studied by temperature-programmed reaction", *Applied Catalysis*, 269, 123-135 (2004).

[43] P.R. Pujado, B.V. Vora, "Make C_3-C_4 olefins selectively", *Hydrocarbon Processing, International Edition*, 69, 65-70 (1990).

[44] J.M. Bockris, S. Srinivasan, *Fuel cells: Their Electrochemistry*, McGraw-Hill, New York, 1969 (Chapter 4).

CHAPTER 4

THE PROCESS OF PROPANE DEHYDROGENATION IN A PROTON-CONDUCTING FUEL CELL

4.1 Introduction

Conversion of propane to propylene in a proton-conducting fuel cell is a process by which propane is dehydrogenated to propylene [1,2,3]. While development of this process clearly has economic and environmental attractiveness, there have been few studies directed to realization of the concept. The challenge has been finding suitable proton-conducting electrolytes and compatible electrodes operating at temperatures below 800°C. Our fuel cell group at the University of Alberta made a breakthrough in this process and proved the feasibility of conversion of propane to propylene in a proton-conducting fuel cell [1,2]. Good fuel cell performance and high selective propylene were achieved using Y-doped $BeCeO_3$ as electrolyte and Pt as electrodes [4,5,6].

In the preliminary work at operating temperatures in the range 600-700°C we detected hydrogen and other small molecule hydrocarbons in the anode outlet gas, in addition to the desired gas product propylene and unreacted propane. Involvement of these hydrocarbon species in the electrochemical reactions in the fuel cell would affect fuel cell performance and propylene selectivity. Consequently, we now have investigated the behaviors of these species to understand the reaction mechanism of propane dehydrogenation in the fuel cell.

4.2 Experimental

4.2.1 Materials

Y-doped $BaCeO_3$ was used as the proton-conducting electrolyte. The preparation procedure was described previously [2]. Y-doped $BaCeO_3$ powder was prepared by solid-state reactions, and then electrolyte solid disks were made by pressing the powder.

Platinum was used for both cathode and anode catalysts, and the electrodes were prepared by screen-printing platinum paste (Heraeus CL11-5100) onto the corresponding surfaces of the BCY15 electrolyte disk. The membrane electrode assembly (MEA) was dried in air at 120°C for 30 min and then fired at 1000°C for 60 min to remove the organic binder and to increase adhesion to the electrolyte. The surface area of each electrode was approximately 0.7 cm^2.

4.2.2 Fuel cell system design

A vertical fuel cell set-up was adopted with a glass sealant to achieve good anode side gas seal [7], as shown in Figure 3-12. This system comprises anode and cathode compartments, each consisting of two co-axial alumina tubes. The inner tube extended from outside the heated reaction zone to a position close to the respective electrode of the cell. The two tubes were fastened together at the remote end with a tailing gas outlet. The cell was sandwiched between the outer tubes of the anode and cathode compartment. The outer perimeter of anode and cathode outer tubes was sealed to the cell by applying a thin layer of glass and ceramic sealant (Aremco 503) respectively. Platinum gauze (52 mesh) was applied as the current collector for both anode and cathode.

The assembled cell was placed in a tubular furnace (Thermolyne F79300). The seals were cured gradually as the cell was heated to the prescribed temperature for testing

[7], prior to operation of the cell under reaction conditions. During the heating procedure, nitrogen was passing through the anode chamber and air through the cathode chamber.

All the fuel cell experiments were carried out in the temperature range of 600-700°C. After the cell had stabilized at the operating temperature, the anode feed was switched to pure C_3H_8 (Praxair, grade 2.0). O_2 (Praxair, grade 2.6) was supplied to the cathode side as oxidant via the inner tube. The gas flow rates were carefully controlled with mass flow controllers.

4.2.3 Electrical measurements and gas analysis

The open circuit voltage and I-V behaviors were measured using a Solartron 1287 electrochemical interface. I-V characteristics were determined potentiodynamically with the electrochemical systems using a scanning rate 5 mV/s. The outlet gases from the anode chamber were analyzed using a Hewlett Packard model HP5890 GC, using a polypack column at 80°C and a thermal conductivity detector (TCD) connected to a computer workstation.

The terms of conversion, selectivity and yield were defined in Chapter 3.

4.3 Results and discussion

4.3.1 Non-electrochemical reactions in the fuel cell system

Ideally, the gas product from the fuel cell system is only propylene if propane dehydrogenation is the only electrochemical reaction (reactions 2-18 and 4-1). However, in the experiments some other species CH_4, C_2H_4, C_2H_6 and H_2 were also detected in the anode chamber effluent by gas chromatography. This was due to the occurrence of other non-electrochemical reactions in the anode chamber of the fuel cell [8]. This situation

became more severe under the open circuit condition because there was no current drawn from the fuel cell, thus there was no electrochemical reaction and the possible reactions were the thermal reactions occurring in the hollow coaxial fuel cell tube and the chemically catalytic reactions on the Pt anode catalyst. When the fuel cell was discharged, the electrochemical reactions were activated and the gas product distribution was improved with enhanced propylene selectivity in contrast to the open circuit condition [2]. However, even in this situation, thermal reactions still could not be avoided. The same gas product species were found in the effluent from the anode chamber in different concentrations, whether under open or close circuit conditions.

Anode: $C_3H_8 \rightarrow C_3H_6 + 2H^+ + 2e^-$ *(2-18)*

Cathode: $2H^+ + \frac{1}{2}O_2 + 2e^- \rightarrow H_2O$ *(4-1)*

So, based on thermodynamic calculations and anode outlet gas analyses, all the following Equations, but not limited to these, are possible non-electrochemical reactions occurring in the fuel cell system.

$$C_3H_8 \rightarrow C_3H_6 + H_2 \qquad (4\text{-}2)$$

$$C_3H_8 \rightarrow CH_4 + C_2H_4 \qquad (4\text{-}3)$$

$$C_2H_4 + H_2 \rightarrow C_2H_6 \qquad (4\text{-}4)$$

$$C_2H_6 + H_2 \rightarrow 2CH_4 \qquad (4\text{-}5)$$

$$1/nC_nH_m \rightarrow C + \frac{m}{2n}H_2 \qquad (4\text{-}6)$$

All these reactions are thermodynamically favored at the fuel cell operating temperatures, and the reaction equilibrium constant of each reaction is shown in Figure 4-1. Studies have shown that thermal reactions of propane followed free-radical chain mechanism [9]. Equation (4-7) is the initial step, while Equations (4-8) through (4-14) and (4-15) thorough (4-20) refer to free radicals propagation and termination, respectively. Catalytic reactions of propane on the Pt catalyst primarily involved two pathways: dehydrogenation by breaking of C-H bond and intramolecular C-C bond cracking [3]. The two pathways compete with each other, shown in Figure 4-2. The gas products distribution in experiments was consistent with these studies in which CH_4, C_2H_4, C_3H_6 and H_2 were the predominant gas products (total selectivity > 90%). In addition, carbon deposition on the anode catalyst was also detected [8] because, at high temperatures, hydrocarbons easily form carbon in an irreversible process, especially for alkenes [10,11,12,13,14,15], which can also be seen from Figure 4-3. Although some researchers mentioned polymerization reactions might be involved in the reaction network, no hydrocarbons with higher molecular weight were detected in effluent from our fuel cell system.

$$C_3H_8 \rightarrow CH_3^* + C_2H_5^* \qquad (4\text{-}7)$$

$$CH_3^* + C_3H_8 \rightarrow C_3H_7^* + CH_4 \qquad (4\text{-}8)$$

$$C_2H_5^* + C_3H_8 \rightarrow C_2H_6 + C_3H_7^* \qquad (4\text{-}9)$$

$$C_3H_7^* \rightarrow C_3H_6 + H^* \qquad (4\text{-}10)$$

$$C_3H_7^* \rightarrow C_2H_4 + CH_3^* \qquad (4\text{-}11)$$

$$H^* + C_3H_8 \rightarrow C_3H_7^* + H_2 \qquad (4\text{-}12)$$

$$H^{\bullet} + C_2H_6 \rightarrow C_2H_5^{\bullet} + H_2 \qquad (4\text{-}13)$$

$$C_2H_5^{\bullet} \rightarrow C_2H_4 + H^{\bullet} \qquad (4\text{-}14)$$

$$H^{\bullet} + H^{\bullet} \rightarrow H_2 \qquad (4\text{-}15)$$

$$H^{\bullet} + CH_3^{\bullet} \rightarrow CH_4 \qquad (4\text{-}16)$$

$$H^{\bullet} + C_2H_5^{\bullet} \rightarrow C_2H_6 \qquad (4\text{-}17)$$

$$H^{\bullet} + C_3H_7^{\bullet} \rightarrow C_3H_8 \qquad (4\text{-}18)$$

$$CH_3^{\bullet} + CH_3^{\bullet} \rightarrow C_2H_6 \qquad (4\text{-}19)$$

$$CH_3^{\bullet} + C_2H_5^{\bullet} \rightarrow C_3H_8 \qquad (4\text{-}20)$$

These non-electrochemical reactions are strongly affected by operating temperatures and propane flow rates, i.e. reaction time. Thus the concentrations of the gas species were functions of the operating conditions [2].

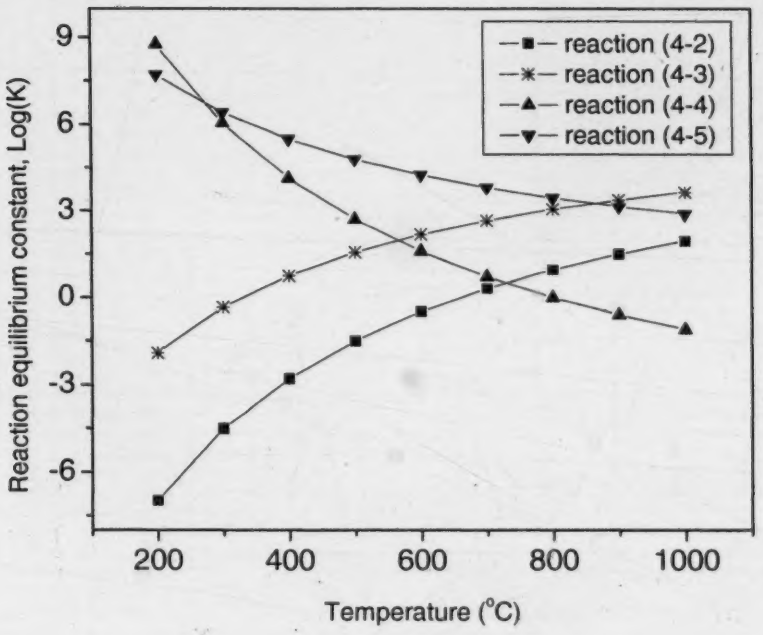

Figure 4-1. Reaction equilibrium constants of the non-electrochemical reactions in C_3H_8 – O_2 fuel cell at different temperatures.

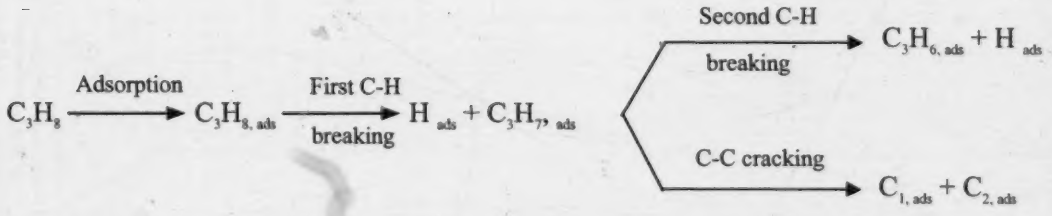

Figure 4-2. Schematic of propane reaction on the platinum catalyst.

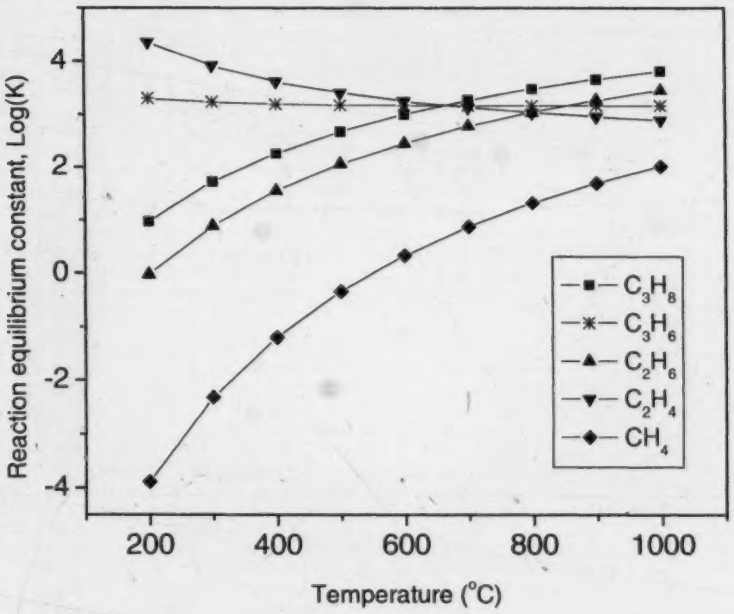

Figure 4-3. Reaction equilibrium constant for carbon formation reaction (4-6) from hydrocarbon species in the gas products.

4.3.2 Open circuit voltage

The electro-motive-force (EMF) for the electrochemical propane dehydrogenation (reaction 4-21) is determined by Nernst Equation (Equation 4-22).

$$C_3H_8(g)+\frac{1}{2}O_2(g)\rightarrow C_3H_6(g)+H_2O(g) \qquad (4\text{-}21)$$

$$E_1 = E_1^o(T)-\frac{RT}{2F}\ln\left(\frac{P_{H_2O}P_{C_3H_6}}{P_{C_3H_8}P_{O_2}^{1/2}}\right) \qquad (4\text{-}22)$$

where $E_1^o(T)$ is the cell standard potential, calculated from thermodynamic data ΔG^o at standard conditions, *i.e.* the potential when the partial pressures of all reactants and products are 1 bar. $P_{C_3H_8}$, $P_{C_3H_8}$, P_{H_2O} and P_{O_2} in the logarithmic term refer to the

equilibrium partial pressures of the gas species at the interfaces between electrodes and electrolyte. Usually the partial pressure at the interface can be replaced by that in the bulk fluid if there is no mass transfer limitation for the gas species. In experiments, the total pressures of anode and cathode compartment were both kept at 1 atm, so the partial pressure of each gas component was not in the standard condition (1 bar). $P_{C_3H_8}$ and $P_{C_3H_6}$ could be calculated from GC analysis of anode outlet gas, but it is not easy to obtain P_{H_2O} because the partial pressure of water vapour in the cathode compartment was very low (~10 ppm) at open circuit condition [16,17], which was difficult to measure accurately by GC. To obtain the value of P_{H_2O} in experiments the water-saturated oxygen at room temperature instead of pure dry oxygen was conducted to the cathode compartment. Thus the values of P_{H_2O} and P_{O_2} were obtained as 0.031 and 0.969 respectively. Because the partial pressures of the gas species were functions of operating temperatures and propane flow rates, the calculated EMF of propane dehydrogenation from Nernst Equation (Equaiton.4-22) also depends on the operating conditions. The calculated EMFs at different temperatures with propane flow rate of 100 mL/min were listed in Table 4-1, as well as partial pressures of the gas species and standard potential (HSC Chemistry Software, Version 5.1, Outokunpu Research).

Table 4-1. The calculated EMF values from Nernst Equation for reactions (4-21), (4-23) and (4-24), as well as the standard potentials and partial pressures of gas species, at different temperatures (propane flow rate: 100 mL/min).

	$C_3H_8 + \frac{1}{2}O_2 \rightarrow C_3H_6 + H_2O$						$H_2 + \frac{1}{2}O_2 \rightarrow H_2O$					$C_2H_6 + \frac{1}{2}O_2 \rightarrow C_2H_4 + H_2O$					
Temperature/ °C	E_1°/ V	P_{C3H8}/ atm	P_{O2}/ atm	P_{C3H6}/ atm	P_{H2O}/ atm	E_1/ V	E_2°/ V	P_{H2}/ atm	P_{O2}/ atm	P_{H2O}/ atm	E_2/ V	E_3°/ V	P_{C2H6}/ atm	P_{O2}/ atm	P_{C2H4}/ atm	P_{H2O}/ atm	E_3/ V
600	0.992	0.948	0.969	0.009	0.031	**1.295**	1.035	0.010	0.969	0.031	**0.994**	0.897	3.60E-4	0.969	0.011	0.031	**0.896**
650	1.014	0.783	0.969	0.043	0.031	**1.265**	1.021	0.037	0.969	0.031	**1.029**	0.917	0.003	0.969	0.047	0.031	**0.937**
700	1.036	0.521	0.969	0.085	0.031	**1.255**	1.006	0.072	0.969	0.031	**1.043**	0.938	0.009	0.969	0.107	0.031	**0.975**

As predicted from the Nernst Equation, the measured open circuit voltage of the $C_3H_8 - O_2$ fuel cell was not only dependent of operating temperature but also propane flow rate, but the value was not in consistence with the calculated EMF. For example, at 600°C with propane flow rate of 100 mL/min, the calculated EMF for the electrochemical reaction of propane dehydrogenation was 1.295 V, which was larger than the measured OCV value 1.085 V. The same phenomena were found during operating the fuel cell at 650°C or 700°C. The apparent discrepancy between the measured OCV values and the calculated EMF values possibly was due to involvement of other side electrochemical reactions in addition to propane dehydrogenation. However, this speculation is based on an assumption that the measured OCV values of an electrochemical reaction, without interference of other side reactions, is equal or very close to the EMF value calculated from Nernst Equation. This assumption usually was not true because conceptually OCV is not same as EMF, and the discrepancy between these two values was even apparent for low temperature fuel cells (such as PEM fuel cell) due to slow anodic and/or cathodic reaction rates where the electrode reactions no longer attain equilibriums [18,19]. For high temperature fuel cells, the OCV value could very closely reach the corresponding EMF value if the electrolyte is a complete ion conductor without electron conduction [20,21,22]. Therefore, before we safely come to the conclusion that the difference between the EMF and measured OCV values of C_3H_8–O_2 fuel cells was caused by involvements of other side reactions in addition to electrochemical propane dehydrogenation, the consistence between OCV and EMF values for a single reaction in our fuel cell system must be proved. Apparently, for the propane dehydrogenation reaction, it can never be guaranteed as the sole electrochemical reaction at the fuel cell operating conditions even with pure propane feed to the anode, as discussed before. So

another experiment was made with pure hydrogen as anode feed and water saturated oxygen (saturated at room temperature) conducted to the cathode, and the OCV of the H_2–O_2 fuel cell is shown in Figure 4-4 (the kink is due to varying hydrogen concentration on the anode catalyst when switching gas). It is obvious that the measured OCV value (the value after reaching equilibrium) at 650°C is 1.158 V, which is almost the same as the calculated value from the Nernst Equation for hydrogen fuel cell 1.160 V. So the experimental results supported the previous deduction, that the gas species in addition to propane could take part in the electrochemical reactions.

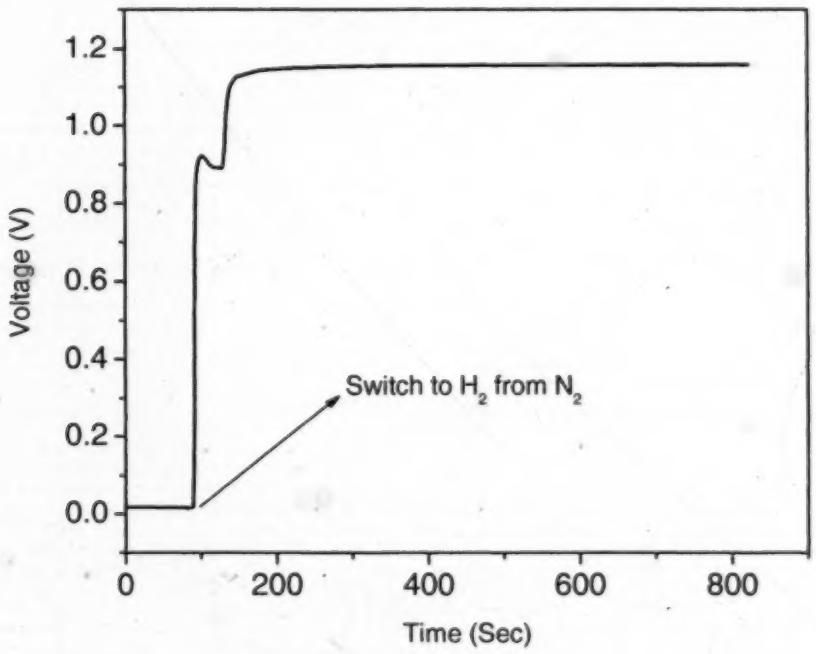

Figure 4-4. Open circuit voltage of H_2–O_2 fuel cell using Y-doped $BaCeO_3$ as electrolyte with pure hydrogen as anode feed and water saturated oxygen as cathode gas at 650°C.

Among the gas species (CH_4, C_2H_4, C_3H_6 and H_2) at the anode outlet, hydrogen can be easily oxidized in the fuel cell (Equation. 4-24) because platinum is an active anode catalyst for hydrogen fuel cells [23,24,25,26,27,28]. Another possibility is that ethane may be involved in the electrochemical reactions through reaction (4-24), similar to propane dehydrogenation. The partial pressures of the gas species involved in reactions (4-23) and (4-24) were determined from GC analysis and are summarized in Table 4-1, as well as the calculated EMF values from Nernst Equations (Equations.4-25 and 4-26). From the comparison of the measured OCV and calculated EMF values of the three different reactions (4-21), (4-23) and (4-24) (Table 4-2), it is apparent that the OCV value was equal to none of the EMF values of three reactions. At 600°C and 650°C, the measured OCV value was less than the EMF value of reaction (4-21) but larger than the EMF values of reaction (4-23) and (4-24). Thus, measured OCV values may be a mixed reaction voltage of these three reactions. A little difference at 700°C is that the measured OCV value is below all of the three EMF values, which indicates some other side reactions maybe also occurred in addition to the three reactions discussed here.

$$H_2 + \frac{1}{2}O_2 \rightarrow H_2O \qquad (4\text{-}23)$$

$$C_2H_6 + \frac{1}{2}O_2 \rightarrow C_2H_4 + H_2O \qquad (4\text{-}24)$$

$$E_2 = E_2^o(T) - \frac{RT}{2F}\ln\left(\frac{P_{H_2O}}{P_{H_2}P_{O_2}^{1/2}}\right) \qquad (4\text{-}25)$$

$$E_3 = E_3^o(T) - \frac{RT}{2F}\ln\left(\frac{P_{H_2O}P_{C_2H_4}}{P_{C_2H_6}P_{O_2}^{1/2}}\right) \qquad (4\text{-}26)$$

Therefore, the measured OCV of $C_3H_8 - O_2$ fuel cell was a result of competition of all the electrochemical reactions present under the open circuit condition, such as reactions (4-21), (4-23) and (4-24), and the value of OCV depends on the proportions of each electro-active species present and the reaction potentials.

Table 4-2. Comparison of measured OCV values of $C_3H_8 - O_2$ fuel cell and the calculated EMFs for different possible electrochemical reactions in $C_3H_8 - O_2$ fuel cell at different temperatures with propane flow rate of 100 mL/min.

Temperature/ °C	Theoretical EMF of reaction (4-21), E_1/ V	Theoretical EMF of reaction (4-23), E_2/V	Theoretical EMF of reaction (4-24), E_3/V	Measured OCV, V/V
600	1.295	0.994	0.896	1.085
650	1.265	1.029	0.937	1.061
700	1.255	1.043	0.975	0.892

4.3.3 Fuel cell performances

The involvements of hydrogen reaction (reaction 4-23) and other side reactions in the process of propane dehydrogenation in the fuel cell were also reflected in the I-V curves. For example, at 650°C with propane flow rate of 100 mL/min, the concentrations of hydrogen and propane were 3.7% and 78.3% respectively in the anode chamber under the open circuit conditions. So if the fuel cell were discharged, the current would be contributed by the gas species in the anode chamber: 3.7% hydrogen, 78.3% propane and/or other gas components. To analyze the individual contribution by each gas species, especially for the hydrogen in the gas products, separate experiments were conducted with propane (100 mL/min) and 3.7% hydrogen (balance with Ar), as the fuels respectively at 650°C (Figure 4-5). If the reactions (reaction.4-21) and (reaction.4-23) are independent, it can be inferred from Figure 4-5 that the C_3H_8–O_2 fuel cell performance was mainly attributed to hydrogen reaction (4-23) rather than propane dehydrogenation (4-21). However, when discharging the fuel cell at low voltage (<0.2 V), the current and power obtained from the hydrogen fuel cell (3.7% H_2 in Ar) were higher than those from the C_3H_8–O_2 fuel cell (with 3.7% H_2 in the gas products) (Figure 4-5). So in the process of propane dehydrogenation in a proton-conducting fuel cell, the desired propane dehydrogenation (reaction.4-21) and the side reaction (reaction.4-23) were not independent but were in competition with each other.

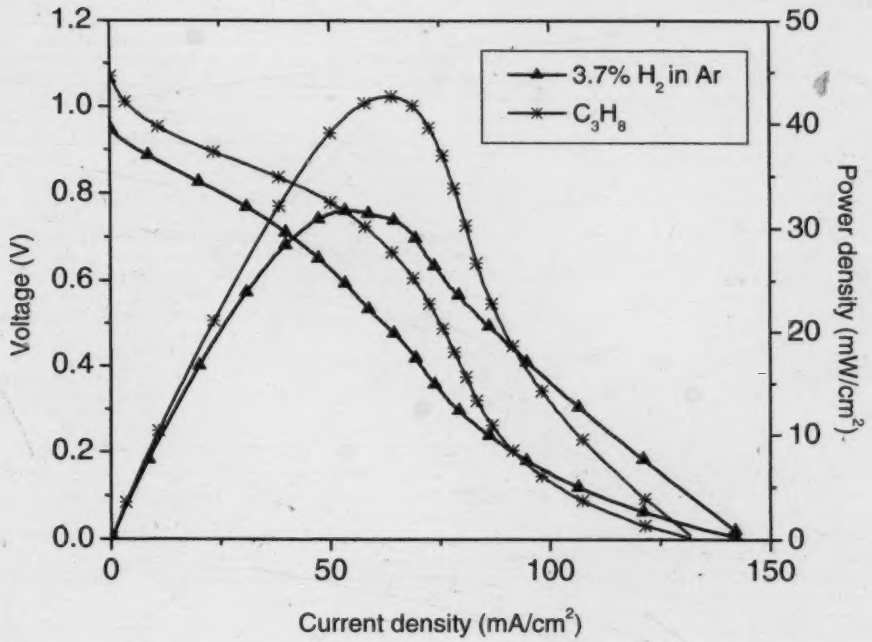

Figure 4-5. Fuel cell performances using pure propane (flow rate: 100 mL/min) and 3.7% hydrogen (balance with argon) as anode feed respectively, with the same electrolyte of Y-doped $BaCeO_3$ and electrodes of Pt at 650°C.

Varying the propane flow rate can influence the concentrations of propane, hydrogen and other species, leading to affecting the fuel cell performances. Figure 4-6 and Figure 4-7 show the fuel cell maximal power density with different propane flow rates at 650°C and 700°C respectively. Depending on the propane flow rate, the variation trend of the maximal power density can be roughly classified into three different zones. Zone I referred to the range of very low propane flow rate, under which conditions the concentration of hydrogen was much higher than propane. So within zone I hydrogen reaction was the predominant electrochemical reaction and the fuel cell performances

were mainly attributed to this reaction, and increasing propane flow rate in this range gave rise to lower hydrogen concentration and thus lower fuel cell performances. However, in the range of very high propane flow rate (zone III) propane concentration was significant in the gas products and propane dehydrogenation became the predominant electrochemical reaction in the fuel cell. Between zone I and zone III, these two electrochemical reactions (reactions.4-21 and 4-23) existed simultaneously but neither of them was superior to the other. In zone II, with increase of propane flow rate, there appeared a maximal point, which means at this point the total contributions of hydrogen reaction and propane dehydrogenation to the fuel cell performances reached the maximal value.

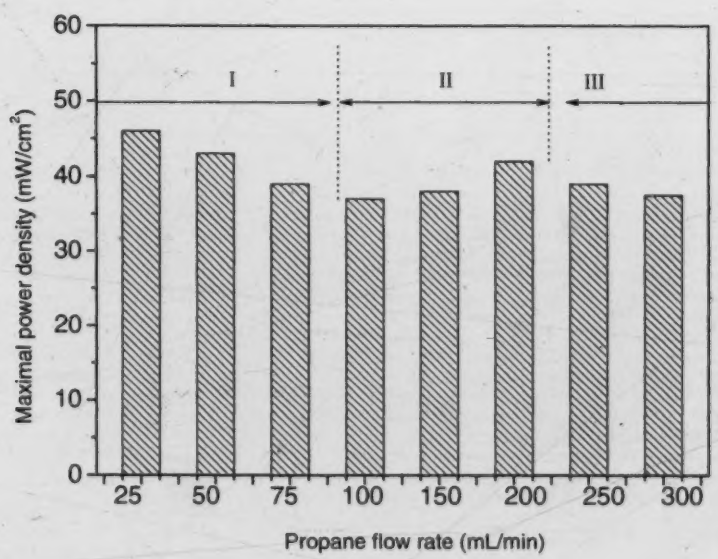

Figure 4-6. Maximal power density at different propane flow rate obtained from C_3H_8–O_2 fuel cell at 650°C.

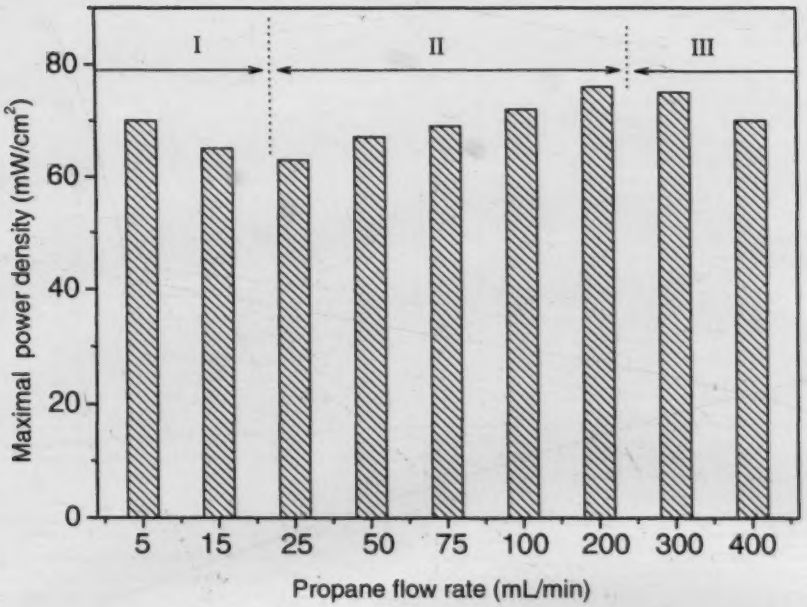

Figure 4-7. Maximal power density at different propane flow rate obtained from C_3H_8–O_2 fuel cell at 700°C.

By comparison of zone I to zone III in Figure 4-6, it can be concluded that the electrochemical reaction activation of propane dehydrogenation was more difficult on Pt catalyst at 650°C than hydrogen reaction activation, because at very high propane flow rate (zone III) the propane concentration in the anode chamber was close to 100%, which was much more than the hydrogen concentration at low propane flow rate (zone I), but higher fuel cell performances were achieved at zone I rather than at zone III. At 700°C (Figure 4-7) very similar fuel cell performances were observed, except that higher maximal power densities were obtained at zone III rather than zone I. So it can be inferred that propane dehydrogenation became easier at 700°C than at 650°C, based on the fact

that the electrochemical hydrogen reaction was favored at higher temperatures on Pt catalyst in the fuel cell [24,25].

4.3.4 Gas products analysis

The changes of propylene and hydrogen yield were also monitored during electrically discharge of the fuel cell. If the electrochemical reaction follows the reaction (4-21) and propane dehydrogenation is the only source of protons produced at the anode, the propylene yield would be proportional to the discharging current, which is easily calculated from the Faraday law. Figure 4-8 shows the relationship of the theoretical propylene yield, i.e. the propylene yield obtained from only electrochemical dehydrogenation of propane, to the discharging current at 650°C with propane flow rate 100 mL/min. The relationship between experimental propylene yield and hydrogen yield with discharging current is also shown in Figure 4-8. Obviously the experimental propylene yield was less than the theoretical value, which indicated propane dehydrogenation was not the only electrochemical reaction and other side electrochemical reactions were involved in this process and contributed some portion of protons. The negative hydrogen yield meant that some amount of hydrogen was consumed during the process of discharging the fuel cell, which confirmed our conclusion that the hydrogen reaction (reaction. 4-23) was one of side electrochemical reactions during the process of propane dehydrogenation in proton-conducting fuel cell. By summation of the absolute values of propylene yield and hydrogen yield at a specific discharging current, it can be seen that the protons consumed in the fuel cell mostly arose from propane dehydrogenation and hydrogen reaction. So, hydrogen reaction was a significant electrochemical reaction in the fuel cell in addition to propane dehydrogenation. Although

electrochemical ethane dehydrogenation (reaction 4-22) may be another side reaction during the process of propane dehydrogenation in the fuel cell, no obvious change of ethane concentration was observed when discharging the fuel cell. So the electrochemical ethane dehydrogenation was not an electrochemical reaction involved in the process.

With increasing discharging current, although propylene yield increased (Figure 4-8), the selectivity to propylene slightly decreased at 650°C (Figure 4-9), which indicates the extent of rate increase of propane dehydrogenation was less than that of hydrogen disassociation.

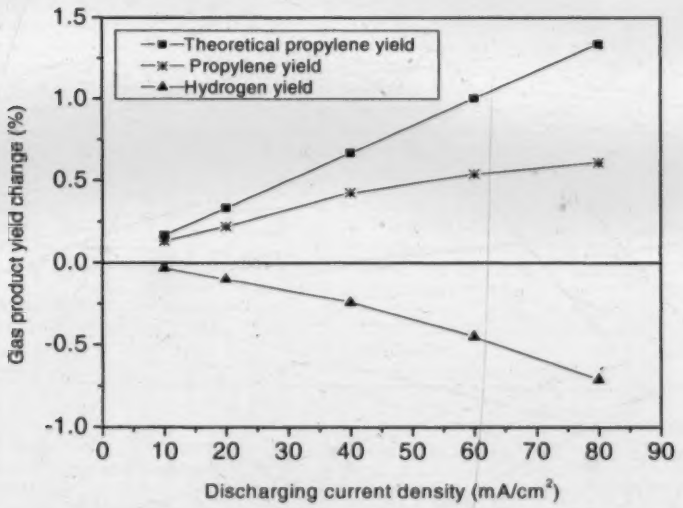

Figure 4-8. Propylene and hydrogen concentration changes in anode chamber effluent at 650°C during discharging C_3H_8–O_2 fuel cell with Y-doped $BaCeO_3$ as electrolyte and platinum as electrodes at propane flow rate 100 mL/min.

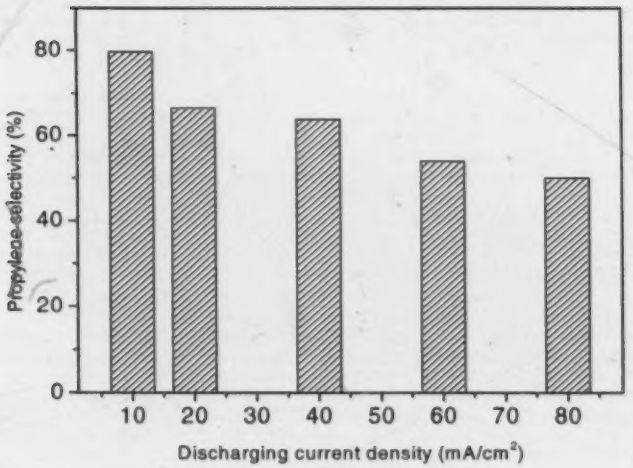

Figure 4-9. Propylene selectivity at different discharging current of C_3H_8–O_2 fuel cell at 650°C.

At 700°C the hydrogen reaction was still the predominant side electrochemical reaction (Figure 4-10); however, its contribution to the fuel cell performances was much less than that of propane dehydrogenation. As a result, the propylene selectivity during discharging the fuel cell at 700°C was much enhanced compared to 650°C (Figure 4-11). At 700°C with propane flow rate of 100 mL/min the propane concentration at the exit to the anode chamber was 52.1% (hydrogen concentration at this condition: 7.2%), which was less than that at 650°C with the same flow rate (hydrogen concentration at this condition: 3.7%), and so the reaction rate of propane dehydrogenation was improved at 700°C relative to the hydrogen reaction. It was inferred that, by increasing operating temperatures from 650°C to 700°C, the electrochemical reaction of propane dehydrogenation became easier to activate in contrast to the electrochemical hydrogen reaction (reaction.4-23).

The information on the reaction mechanism of electrochemical dehydrogenation of propane in a fuel cell is very limited in the open literature. Cheng, et al [3] proposed a three-step reaction process. First, propane molecule chemisorbs on the catalyst surface, and then dissociates to propylene, and two hydrogen atoms. The hydrogen atoms are subsequently transformed to protons that are conducted through the membrane to the cathode side, while propylene desorbs from the catalyst surface and makes the active sites available for further reaction (Figure 4-12). Because low operating temperature (<250°C) was used in this case with PBI polymer as proton-conducting electrolyte, the reaction mechanism in our system may not be the same as the one Cheng, et al. proposed. Based on the increased propylene selectivity during electrochemical dehydrogenation of propane in fuel cells compared to catalytic dehydrogenation of propane on platinum catalyst [2] as well as the demonstrated mechanism of catalytic dehydrogenation of propane on platinum (Figure 3) [29], the reaction mechanism of electrochemical dehydrogenation of propane in this proton-conducting fuel cell is proposed by analogy with catalytic dehydrogenation of propane. The initial step of propane adsorption on the anode in a fuel cell system may be the same as the catalytic dehydrogenation, but the following steps could be different due to the existence of electrons and/or such formed local electrical field on the anode catalyst surface. There is a speculation that electrons can assist in removing the disassociated hydrogen atoms from anode catalysts surface by forming protons, which promotes C-H bond breaking rather than C-C bond cracking. But more experiments are needed to illustrate this process. In addition, the extent of influence of electrons or such formed local electrical field on the reaction mechanism is dependent of the electron concentration at the anode catalyst surface, which was reflected in the experimental results that different propylene selectivity was obtained at different currents [2]. To better

understand the details of this reaction mechanism, further more investigations are required.

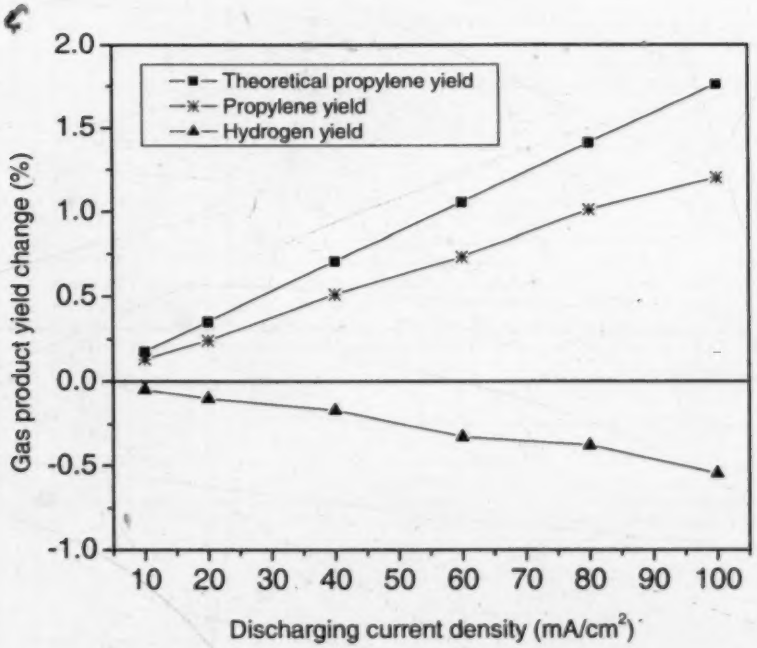

Figure 4-10. Propylene and hydrogen concentration changes in anode chamber effluent at 700°C during discharging C_3H_8–O_2 fuel cell with Y-doped $BaCeO_3$ as electrolyte and platinum as electrodes at propane flow rate 100 mL/min.

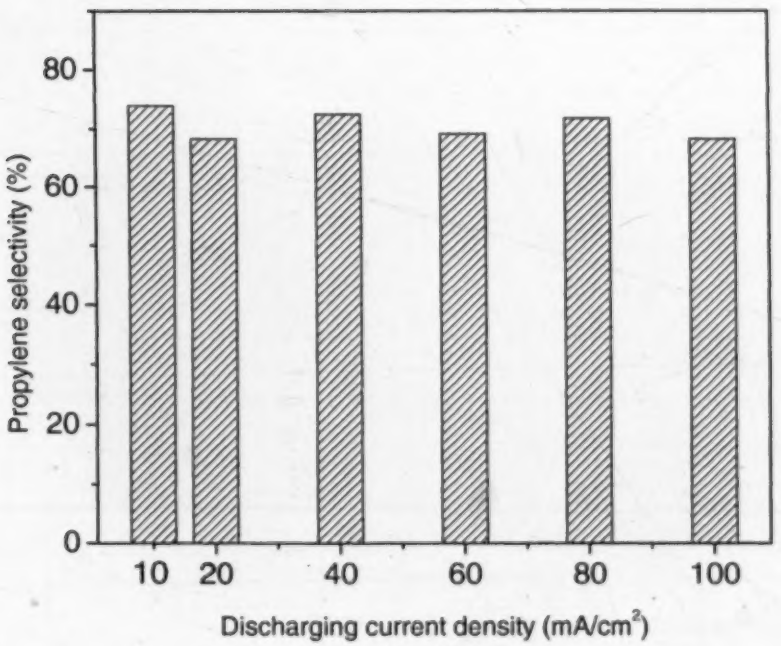

Figure 4-11. Propylene selectivity at different discharging current of C_3H_8–O_2 fuel cell at 700°C.

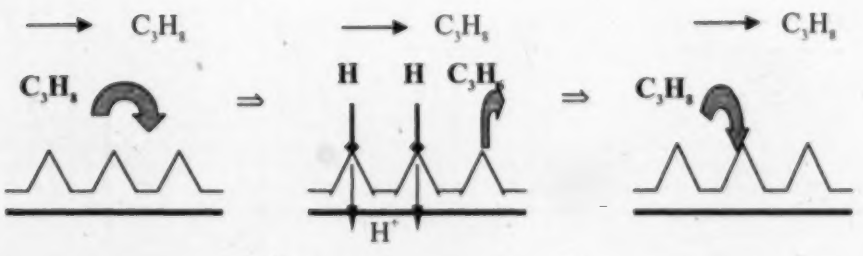

Figure 4-12. Schematic of proposed electrochemistry reactions utilizing propane (Adapted from ref.3).

4.4 Conclusions

During the operation of propane dehydrogenation in a proton-conducting fuel cell other gas species caused by the thermal cracking and catalytic reactions of propane in the fuel cell anode chamber were involved in this process. Hydrogen oxidation reaction was the most significant side electrochemical reaction, which was in competition with propane dehydrogenation in the fuel cell. Compared to the hydrogen oxidation reaction, the electrochemical reaction of propane dehydrogenation was more difficult to activate at 650°C but much easier at 700°C, which results in a higher selectivity to propylene obtained at 700°C than 650°C.

References

[1] Y. Feng, J. Luo, S. Wang, J. Melnik, K.T. Chuang, "Investigation of Y-doped $BaCeO_3$ as electrolyte in propane fueled proton conducting solid oxide fuel cell", *Proceedings of the International Symposium on Fuel Cell and Hydrogen Technologies*, Editor: D. Ghosh, Calgary, Canada, Aug. 21-24, pp. 461-471 (2005).

[2] Y. Feng, J. Luo, K.T. Chuang, "Conversion of propane to propylene in a proton-conducting solid oxide fuel cell", *Fuel*, 86, 123-128 (2007).

[3] C.K. Cheng, "Application of PBI membrane polymer fuel cell for conversion of hydrocarbon", *Masters Thesis*, University of Alberta, pp. 120-129 (2004).

[4] J.H. White, M. Schwartz, A.F. Sammells, "Solid state proton and electron mediating membrane and use in catalytic membrane reactors", *United States Patent*, No. 6,281,403 B1, 28 Aug. 2001.

[5] W.G. Barker, B.S. Berland, M. Schwaartz, L. Simpson, J. Armstrong, "Apparatus and method for the design and manufacture of thin-film electrochemical devices", *United States Patent*, No. 6,772,501 B2, 10 Aug. 2004.

[6] D.J. Edllund, D.T. Friesen, "Hydrogen-permeable composite metal membrane and uses thereof", *United States Patent*, No.5, 217,506, 08 Jun. 1993.

[7] Y. Feng, J. Luo, K.T. Chuang, "Analysis and improvement of chemical stability of Y-doped $BaCeO_3$ as proton conducting electrolytes in C_3H_8 - O_2 fuel cells", *Journal of New Materials for Electrochemical Systems*, 10(3), 147-152 (2007).

[8] Y. Feng, J. Luo, K.T. Chuang, "Carbon deposition during propane dehydrogenation in a fuel cell", *Journal of Power Sources*, 167, 486-490 (2007).

[9] F.O. Rice, K.K. Rice, *The Aliphatic Free Radicals*, Baltimore, Johns Hopkins Press, 1935.

[10] P.R. Pujado, B.V. Vora, "Make C_3-C_4 olefins selectively", *Hydrocarbon Processing, International Edition*, 69, 65-70 (1990).

[11] G.F. Hornaday, F.M. Ferrell, G.A. Mills, "Manufacture of mono- and diolefins from paraffins by catalytic dehydrogenation", *Advances in Petroleum Chemistry and Refining*, 4, 54-96 (1961).

[12] R.G. Craig, D.C. Spence, "Catalytic dehydrogenation of liquefied petroleum gas by the Houdry Catofin and Catadiene processes", *Handbook of Petroleum Refining Processes*, McGraw-Hill, New York, 1986.

[13] C.P. Poole, D.S. MacIver, "The physical–chemical properties of chromia-alumina catalysts", *Advances in Catalysis*, 17, 223–314 (1967).

[14] R.O. Dunn, F.M. Brinkmeyer, G.F. Schuette, "The Phillips STAR process for the dehydrogenation of C_3, C_4, and C_5 paraffins", *Proceedings of the NPRA Annual Meeting, New Orleans*, LA, 22–24 March 1992.

[15] A.H. Weiss, "Which propylene process is best?" *Hydrocarbon Process*, 47, 123–127 (1968).

[16] M. Liu, P. He, J. Luo, A.R. Sanger, K.T. Chuang, "Performance of a solid oxide fuel cell utilizing hydrogen sulfide as fuel", *Journal of Power Sources*, 94, 20-25 (2001).

[17] N.U. Pujare, K.W. Semkow, A.F. Sammells. "A Direct H_2S/Air Solid Oxide Fuel Cell", *Journal of the Electrochemical Society*, 134, 2639-2640 (1987).

[18] W.J. Fleming, "Physical principles governing nonideal behavior of the zirconia oxygen sensor", *Journal of the Electrochemical Society*, 124, 21-26 (1977).

[19] J. Weissbart, R. Ruka, "Solid electrolyte fuel cell", *Journal of the Electrochemical Society*, 109, 723-726 (1962).

[20] J. Larminie, A. Dicks, Fuel Systems Explained; Wiley: Chichester, U. K., 2000.

[21] G. Alberti, M. Casciola, M. Pica, G.D. Cesare, "Preparation of nano-structured polymeric proton conducting membranes for use in fuel cells", *Annals of the New York Academy of Sciences*, 984, 208-225 (2003).

[22] S.C. Singhal, "Application of ionic and electronic conducting ceramics in solid oxide fuel cells", *Proceedings - Electrochemical Society*, 97 (24), 125-136 (1998).

[23] T. Hibino, A. Hashimoto, M. Suzuki, M. Sanob, "A solid oxide fuel cell using Y-doped $BaCeO_3$ with Pd-loaded FeO anode and $Ba_{0.5}Pr_{0.5}CoO_3$ cathode at low temperatures", *Journal of the Electrochemical Society*, 149, A1503-A1508 (2002).

[24] H. Iwahara, T. Esaka, H. Uchida, N. Maeda, "Proton conduction in sintered oxides and its application to steam electrolysis for hydrogen production", *Solid State Ionics*, 3-4, 359-363 (1981).

[25] H. Iwahara, H. Uchida, K. Ono, K. Ogaki, "Proton conduction in sintered oxides based on barium cerate ($BaCeO_3$)", *Journal of the Electrochemical Society*, 135, 529-533 (1988).

[26] H. Uchida, H. Yoshikawa, T. Esaka, S. Ohtsu, "Formation of protons in strontium cerium oxide ($SrCeO_3$)-based proton conducting oxides. Part II. Evaluation of proton concentration and mobility in ytterbium-doped $SrCeO_3$", *Solid State Ionics*, 36, 89-95 (1989).

[27] F. Seland, T. Berning, B. Børresen, R. Tunold, "Improving the performance of high-temperature PEM fuel cells based on PBI electrolyte", *Journal of Power Sources*, 160 (1), 27-36 (2006).

[28] J.H. Wee, K.Y. Lee, "Overview of the development of CO-tolerant anode electrocatalysts for proton-exchange membrane fuel cells", *Journal of Power Sources*, 157 (1), 128-135 (2006).

[29] S.Y. Yu, "Coupling alkane dehydrogenation reactions with hydrogenation reactions on cation-modified H-ZSM5", *Ph.D. Dissertation*, University of California, Berkeley (2001), pp.8-30.

CHAPTER 5

Cr_2O_3 BASED ANODE CATALYSTS FOR PROPANE DEHYDROGENATION IN A PROTON-CONDUCTING FUEL CELL

5.1 Introduction

High temperature propane dehydrogenation reactions are unselective because all equivalent C-H bonds have equal bonding energy, and therefore, an equal chance of reaction [1,2,3,4,5].Propylene is formed when two C-H bonds of neighbouring carbons are broken and a C=C double bond is formed. If the two C-H bonds are part of two different propane molecules, higher molecular-weight hydrocarbons are formed, and extensive C-H bond breaking and C-C bond formation may lead to hydrogen gas and coke. Hence, it is clear that a proper choice of catalyst is needed to achieve an optimum dehydrogenation process that has both high conversion and high selectivity to propylene.

Platinum is active for propane dehydrogenation [6,7,8,9,10,11,12]. Usually platinum is used in the form of a supported catalyst, such as supported on Al_2O_3 in the industrial OLEFLEX process licensed by UOP [13]. In the work described in Chapter 3, commercial platinum paste was investigated as the anode catalyst for propane dehydrogenation in the proton-conducting fuel cell, and it was shown that platinum had high electrochemical activity under fuel cell conditions. However, due to the high cost of platinum, alternative catalysts were developed for the process of propane dehydrogenation in the fuel cell. Since the pioneering work of Frey et al. [14], the

superior properties of supported chromium oxide catalysts for alkane dehydrogenation are well-known, and Cr_2O_3/Al_2O_3 catalysts are widely used in industrial processes [15,16,17,18,19,20,21,22]. A possible catalytic mechanism for alkane dehydrogenation over Cr_2O_3/Al_2O_3 catalysts, illustrated in Figure 5-1 [23], involves the adsorption of an alkane on a coordinative unsaturated Cr^{3+}-center, which can be either isolated or clustered. In a second step, the C-H bond of the alkane is broken, and an O-H-bond and a Cr-C bond are formed. In the product formation step, an alkene is released from the surface and a Cr-H bond is formed as an intermediate species. The catalytic surface is regenerated by the formation of H_2.

In this study, chromium (III) oxide was investigated as the anode catalyst for the process of propane dehydrogenation in a proton-conducting fuel cell with BCY15 as electrolyte at operating temperatures of 600-700°C.

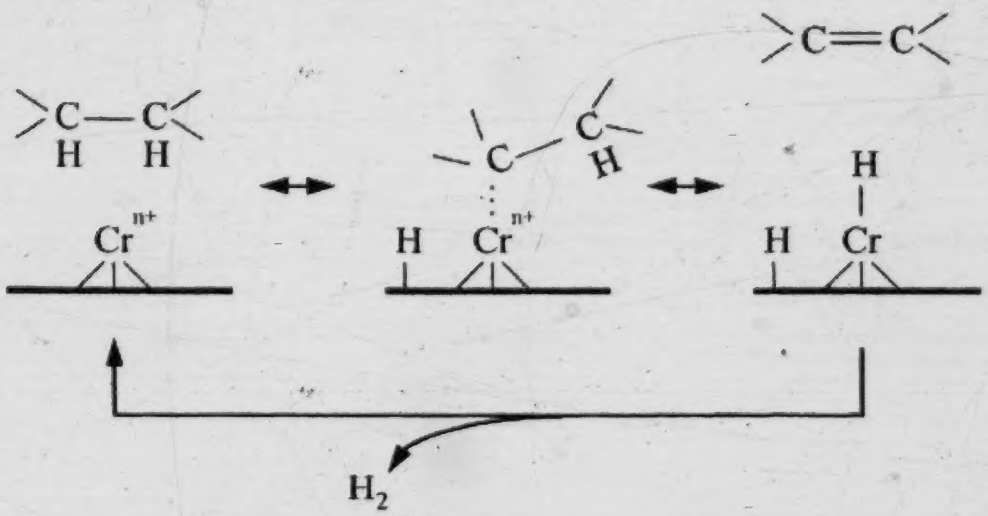

Figure 5-1. Catalytic mechanism for alkane dehydrogenation over Cr_2O_3/Al_2O_3 catalysts (Adapted from ref.23).

5.2 Experimental

5.2.1 Synthesis of chromium (III) oxide based anode catalyst

The sol-gel method was used to synthesize nano-chromium oxide dehydrogenation catalysts [24,25,26,27,28,29]. A 0.18 mol·L^{-1} Cr^{3+} aqueous solution was prepared by dissolving $Cr(NO_3)_3 \cdot 9H_2O$ (Aldrich; 99% purity) in deionized water. The catalyst precursor was formed by precipitation from this solution with an approximately 2 mol·L^{-1} ammonia aqueous solution added dropwise with stirring by a Teflon-coated magnetic stir bar. The reacting mixtures were stirred continuously throughout the synthesis procedure. The ammonia aqueous solution was added until the solution became slightly basic, as indicated by pH paper. The precipitate was separated by filtration, washed three times with deionized water, and then suspended in 2-butanol. The resulting gel was stirred overnight. When gelation was complete, the solute initially present was contained within the final gel. The green gelatinous substance formed was filtered again. The obtained material was sintered in an oven by 1°C·min^{-1} to 110°C where it was kept for 2 h and then the temperature was increased by 2°C/min to 600°C, at which it was kept for 6 h.

Since chromium (III) oxide is not electronically conductive at high temperatures, it cannot be used alone as a fuel cell electrode. To increase the electronic conductivity of the catalyst, conductive Ag or Fe was added to the synthesized chromium (III) oxide powder in a 50:50 volume ratio and tested. The impregnation of the metals was made by dissolving $Ag(NO_3)$ or $Fe(NO_3)_3$ in deionized water, and then introducing synthesized chromium(III) oxide powder into the solution with stirring with a Teflon-coated magnetic stir bar at about 100°C, followed by thermal treatment at 500°C in flowing air for 5 h.

The impregnated powder was then ground in iso-propanol using a planetary ball mill (Fritsch P-5) with a zirconia mill container and zirconia balls at 120 r.p.m. for 8 h.

5.2.2 Fuel cell system

As described in previous Chapters, the vertical fuel cell set-up with a glass sealant was adopted for testing with BCY15 as the electrolyte and platinum paste (Heraeus CL11-5100) as cathode. The procedure to make BCY 15 electrolyte disks was also the same as used in Chapter 3. The anode and cathode were prepared by screen-printing the synthesized Cr_2O_3 based anode catalysts and platinum paste respectively onto the corresponding surfaces of the BCY15 electrolyte disk, and then were dried in air at 120°C for 30 min to remove the organic solvent and to increase adhesion to the electrolyte.

5.2.3 Characterization of anode catalysts, fuel cell performance and gas products

The microstructure of the synthesized chromium (III) oxide powder was examined using a Hitachi S-2700 scanning electron microscope (SEM). Freshly prepared and used Cr_2O_3 based anode catalysts from the $C_3H_8 - O_2$ fuel cell were compared using X-ray Powder Diffraction (XRD) analysis. In the test, a Solartron Electrochemical interface (S1 1287) was used to monitor the open circuit voltage (OCV) between anode and cathode, measure current-potential performance and electrochemical impedance. Potentiodynamic mode was used when performing current-potential measurements, and the scanning rate was kept at 5 mV/s. Impedance data typically were obtained over the frequency range 1 MHz to 0.1 Hz. Gas analysis of the anode effluent streams was

performed during fuel cell experiments using a Hewlett Packard model HP5890 GC, using a polypack column at 80°C and a thermal conductivity detector (TCD) connected to a computer workstation. The terms "propylene selectivity" and "hydrogen yield" in the following discussions were defined in Chapter 3.

5.3 Results and discussion

5.3.1 Materials

SEM micrographs (Figure 5-2) of the chromium (III) oxide powder synthesized by the sol-gel method showed uniform distribution of particle size, mostly in the range 250-350 nm. Figure 5-3 shows the SEM image of the fuel cell assembly cross-section view of the BCY15 electrolyte and the anode catalyst. The porous electrode formed with several interior cavities, improving the surface area and mass transfer. The XRD profiles of Cr_2O_3 based anode catalyst mixed with Ag before and after test in the fuel cell for 24 h (Figure 5-4) showed no obvious changes, and the same phenomena was found on the anode catalyst comprising Cr_2O_3+Fe. Thus, the anode material prepared using this chromium (III) oxide powder was stable for use in the fuel cell for propane dehydrogenation.

Figure 5-2. Microstructure of synthesized chromium oxide powder.

Figure 5-3. SEM micrograph of cross section of a BCY15/Cr_2O_3 anode catalyst interface.

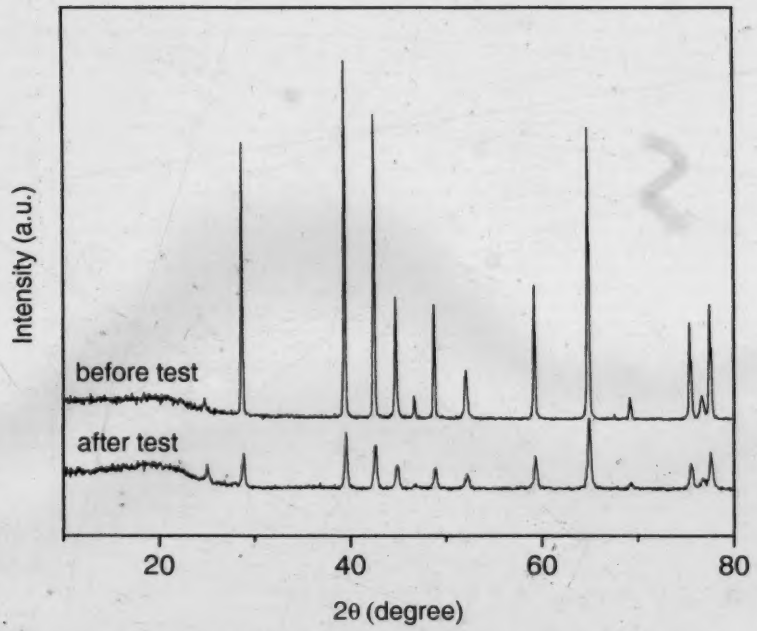

Figure 5-4. XRD profiles of the anode Cr_2O_3+Ag before and after test in fuel cell at 700°C for 24 h.

5.3.2 Fuel cell performances

Before the fuel cell measurements, nitrogen was supplied to the anode chamber during heating the fuel cell up to the operating temperatures. After the cell temperature reached 600°C hydrogen was introduced to reduce the silver oxides or iron oxides in the anode components to the corresponding metals. The reduction process was monitored using impedance measurements. None of Cr_2O_3, silver oxide or iron oxide was a good electronic conductor at 600°C, and the conductivity of the cell increased during the reduction process. When the cell conductivity reached to constant value, the reduction process was completed and then nitrogen was switched to propane for fuel cell measurements.

Impedance spectra for the Cr_2O_3+Ag/BCY15/Pt cell operated at 650°C and 700°C are shown in Figures 5-5. Theoretically, there should be at least two semicircles, because there were at least two electrochemical reactions: propane dehydrogenation and hydrogen oxidation, as discussed in Chapter 4. These two reactions would simultaneously take place on anode catalysts' surfaces, but in our tests the two semicircles evidently are not well developed and merge into almost one because maybe one of them was predominant, so that it covered the others. As described earlier, the intercept of the first high frequency semicircle with the real-axis is related to the ionic conductivity of electrolyte as well as additional ohmic losses in electrical connection wire and contact resistance. The total ohmic resistance decreased with increasing temperature. Although the resistances due to electrical connection wire and electronic conduction in the electrodes increased with increasing temperature, the effects of these were less pronounced when compared to the decreasing extent of resistance due to ionic conduction of electrolyte as the temperature increased, and thus was exceeded by the reduction in the total ohmic resistance. The same phenomena were found for impedance spectra measurements for the cell based on the Cr_2O_3+Fe anode (Figure 5-6). The ohmic resistance obtained from the cell with the anode Cr_2O_3+Fe was very close to the resistance achieved from the cell with the anode Cr_2O_3+Ag, which is consistent with the theoretical predictions, as the cell components were exactly the same in the two measurements except for the different conductive metals (Ag or Fe) that play much lesser roles in determining the total ohmic resistance.

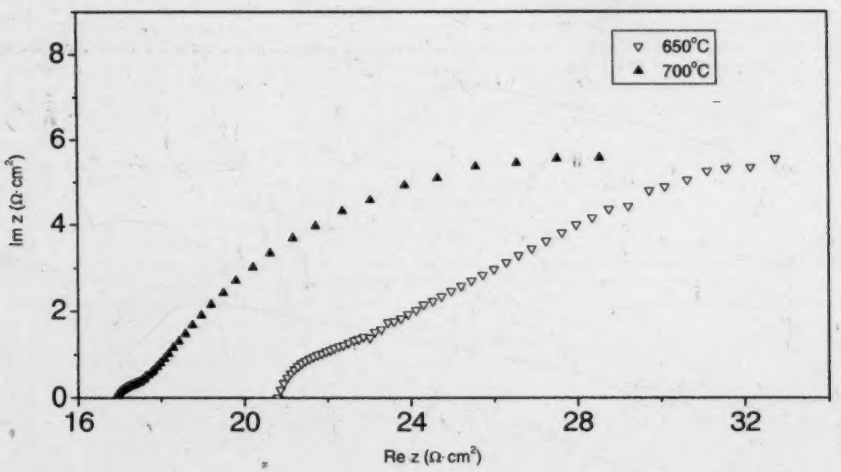

Figure 5-5. Impedance spectra of C_3H_8-O_2 fuel cell with the anode catalyst Cr_2O_3+Ag.

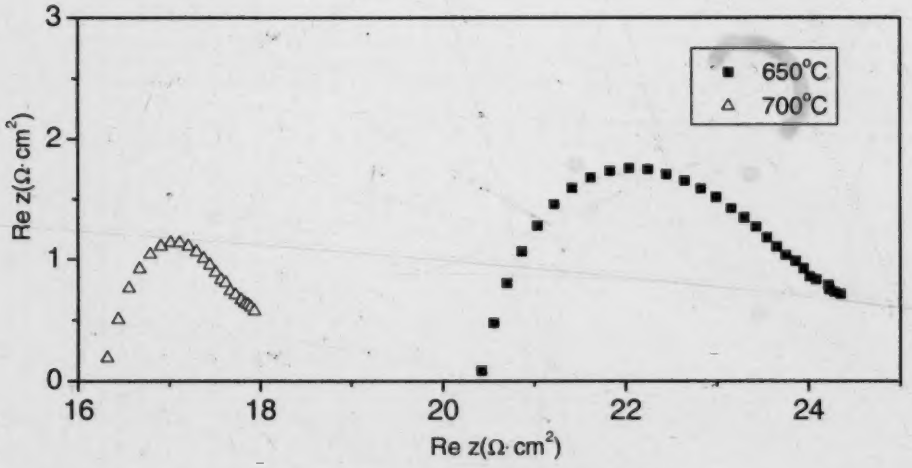

Figure 5-6. Impedance spectra of C_3H_8-O_2 fuel cell with the anode catalyst Cr_2O_3+Fe.

Figure 5-7 and Figure 5-8 display the fuel cell performances obtained on the two kinds of anode catalysts at different operating temperatures. It is obvious that a higher operating temperature greatly enhanced the fuel cell performances. The maximum power density and maximum current density achieved using the anode catalyst Cr_2O_3+Ag increased from 45 mW/cm^2 and 293 mA/cm^2 at 650°C to 82 mW/cm^2 and 495 mA/cm^2 at 700°C respectively (Figure 5-7), and the same results were obtained on the anode catalyst Cr_2O_3+Fe (Figure 5-8). It is known that the fuel cell current density-voltage performance curves can be divided into three stages: activation loss, ohmic loss and concentration loss [30,31,32,33]. The higher operating temperature not only decreased the ohmic loss, but also decreased the activation loss by improving the catalytic activity of anode catalyst. In addition, the higher operating temperature favoured the mass transport process in the fuel cell.

It can be seen from comparison of Figure 5-7 and Figure 5-8 that higher fuel cell performances were obtained using the anode catalyst Cr_2O_3+Fe. For example, at 700°C the maximum power density was 82 mW/cm^2 using Cr_2O_3+Ag, while it reached 108 mW/cm^2 using Cr_2O_3+Fe under similar operating conditions. The difference in the fuel cell performance is attributed to the performance of the electronic conductors (Ag and Fe) added to the anode catalysts. From the aspect of electronic conduction, silver is superior to iron under similar conditions. If the functions of silver and iron in the anodes were just pure electronic conductors, better cell performance would have been achieved with Cr_2O_3+Ag in contrast to Cr_2O_3+Fe. So it can be inferred that iron also showed some activity for the electrochemical reaction. Separate experiments were conducted to study the activity performance of silver and iron for chemical propane dehydrogenation in a

quartz tube filled with silver or iron, and none of them was found with obvious activity for propane dehydrogenation. Therefore, iron or silver maybe demonstrate the activities for the electrochemical reaction of hydrogen oxidation, which could occur in fuel cell operating process. This deduction is confirmed by the finding of Hibino, et al. [34] that iron was an active anode component for hydrogen oxidation reaction in the H_2-O_2 fuel cell. In addition, our experimental results also showed that higher cell performances were obtained in the H_2-O_2 fuel cell (BCY15 as electrolyte and Pt as cathode) with iron as anode compared to with silver as anode.

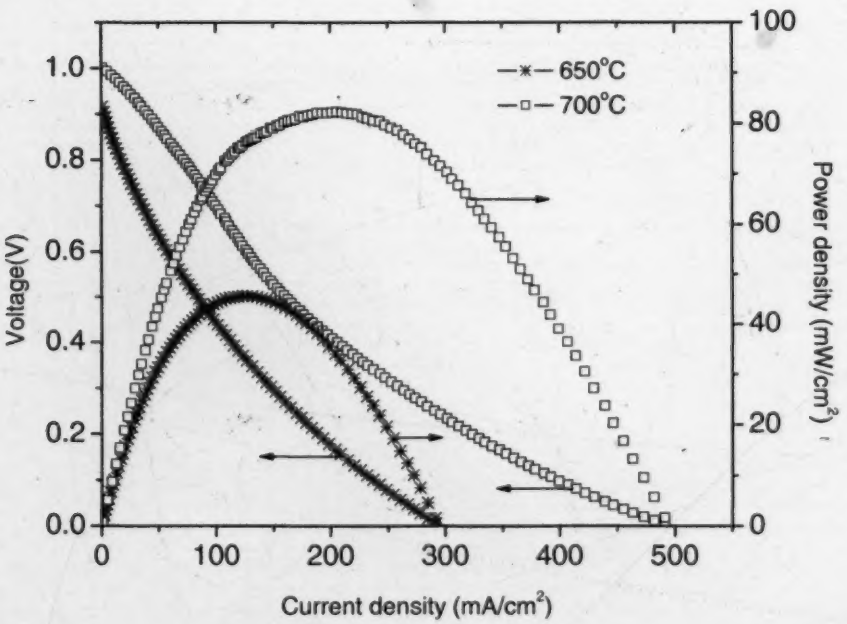

Figure 5-7. Fuel cell performances with the anode catalyst Cr_2O_3+Ag at propane flow rate of 100 mL/min.

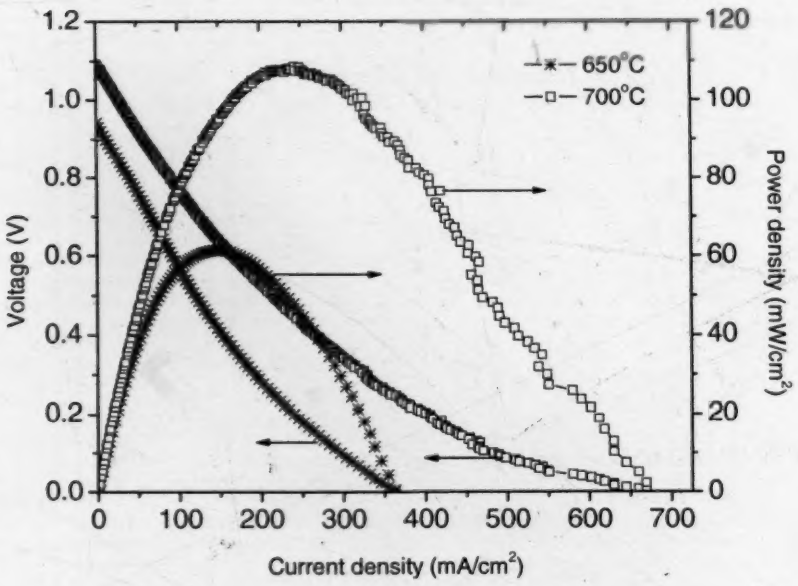

Figure 5-8. Fuel cell performances with the anode catalyst Cr_2O_3+Fe at propane flow rate of 100 mL/min.

In addition to the operating temperature, the influence of propane flow rate on the fuel cell performances was also investigated. Unlike the complex situations found using anode catalysts prepared using commercial platinum paste, as discussed in Chapter 4, fuel cell performances increased with increasing of propane flow rates in the operating range 60-300 mL/min (Figure 5-9). There are two reasons accounting for the difference found between the Cr_2O_3 based anode catalysts and those derived from commercial platinum paste. First, the Cr_2O_3 based anode may not be as active for hydrogen oxidation in the fuel cell as platinum. So, propane dehydrogenation was the predominant electrochemical reaction under our operating conditions when using Cr_2O_3 based anode catalysts. Second, the range of propane flow rate when using Cr_2O_3 based anode catalysts could not be adjusted to as widely as with platinum anodes, because the Cr_2O_3 based anode catalysts

were very sensitive to carbon deposition. This would result in a reduction in activity when the cell was operated under strenuous conditions.

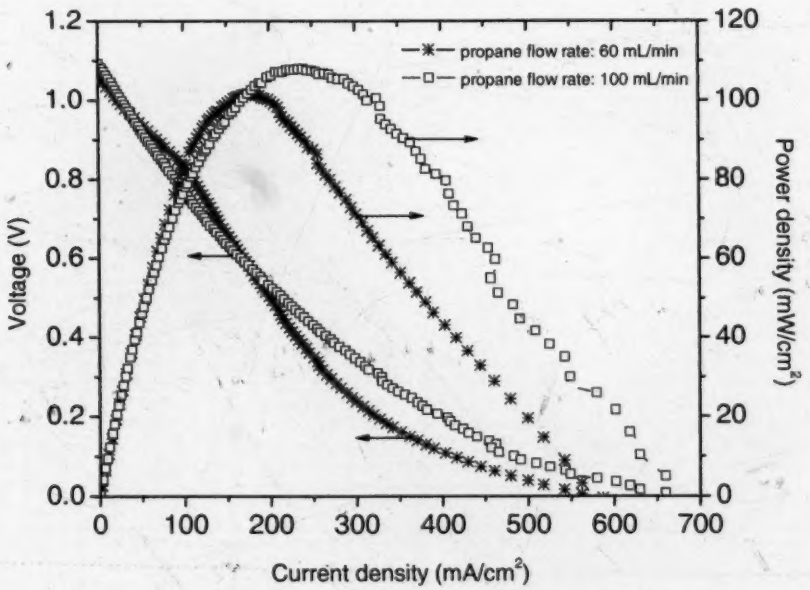

Figure 5-9. Fuel cell performances with the anode catalyst Cr_2O_3+Fe at different propane flow rates (700°C).

5.3.3 Gas products analysis

The anode outlet gas products were monitored by GC and the same gas species were detected during use of the Cr_2O_3 based anode catalysts as when using platinum. The propylene selectivity obtained from electrochemical reactions process using Cr_2O_3+Ag and Cr_2O_3+Fe are shown in Figure 5-10. Apparently higher propylene selectivity was obtained when using Cr_2O_3+Ag, and it reached values up to 95%. In contrast, the propylene selectivity obtained with Cr_2O_3+Fe was below 85% and most values were in the range of 70-80% under our operating conditions, which were comparable to the results obtained on platinum. The difference between propylene selectivity for the two

kinds of Cr_2O_3 based anode catalysts was consistent with the above conclusion that iron was more active than silver for side electrochemical reaction of hydrogen oxidation during the process of propane dehydrogenation in the fuel cell. When using the anode catalyst Cr_2O_3+Ag, the side electrochemical reaction of hydrogen oxidation was suppressed and the desired electrochemical reaction of propane dehydrogenation predominated, and so the reaction became more selective, leading to higher propylene selectivity. This conclusion was also confirmed by analysis of hydrogen yield during current flow conditions (Figure 5-11), and more hydrogen was consumed using Cr_2O_3+Fe than using Cr_2O_3+Ag.

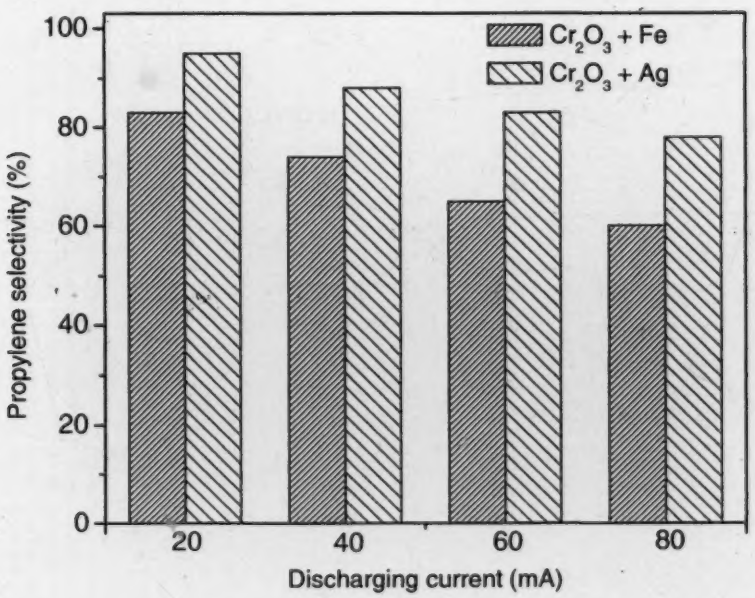

Figure 5-10. Propylene selectivity obtained from electrochemical reaction process using the Cr_2O_3 based anode catalysts (700°C; propane flow rate: 100 mL/min).

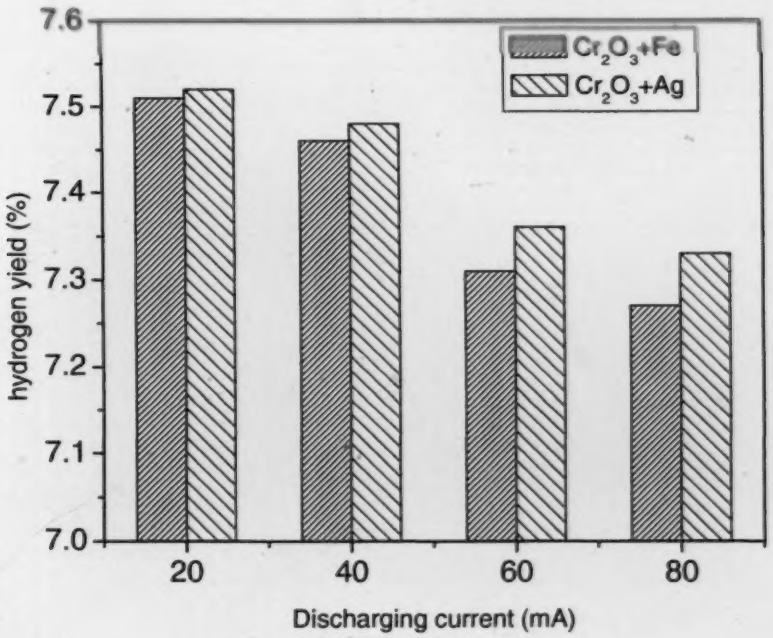

Figure 5-11. Hydrogen yield obtained using the Cr_2O_3 based anode catalysts under current flow conditions (700°C; propane flow rate: 100 mL/min).

5.3.4 Stability test of chromium (III) oxide based anode catalyst

Although XRD analysis showed the Cr_2O_3 based anode catalysts were unchanged after use, and thus chemically stable in the fuel cell under our operating conditions, the fuel cell performances obtained with such materials decreased continuously during the 10 h test (Figure 5-12). The degradation of cell performances was due to carbon deposition on the anode catalyst leading to a reduction of activity. Figure 5-13 shows the XPS analysis of 1s electrons of carbon on the anode surfaces. The anode was operated under fuel cell conditions for 24 h. Additional research on and discussion of carbon deposition during the process of propane dehydrogenation in the proton-conducting fuel cell will be presented separately in Chapter 6.

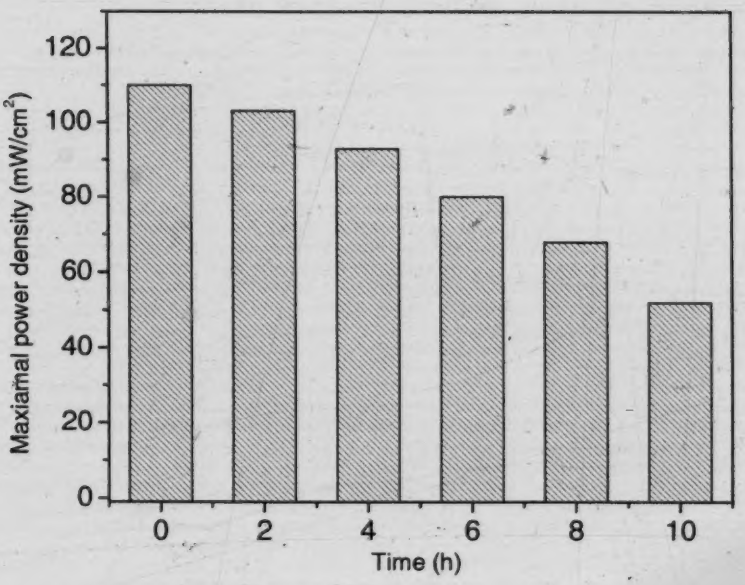

Figure 5-12. Influence of carbon deposition on fuel cell performance using Cr_2O_3+Fe with time on stream (700°C; propane flow rate: 100 mL/min).

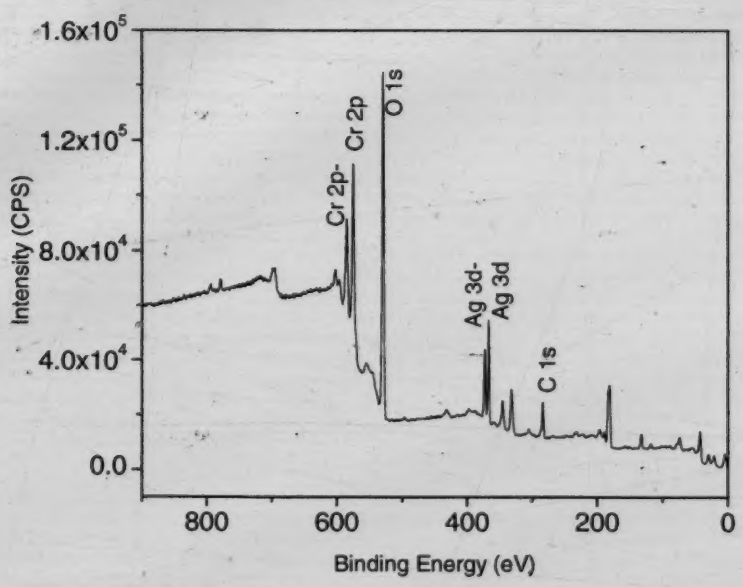

Figure 5-13. Binding energy peak of C1s in the anode Cr_2O_3+Ag after 24h fuel cell test.

5.4 Conclusions

Chromium (III) oxide based anode catalysts synthesized by sol-gel method are effective for propane dehydrogenation in the proton-conducting fuel cell using BCY15 as electrolyte and platinum as cathode. High fuel cell performances and high propylene selectivity are obtained whether on Cr_2O_3+Ag or on Cr_2O_3+Fe. Iron in the composite Cr_2O_3+Fe anode serves as an electronic conductor and also contributes to the fuel cell performances by activation of the side electrochemical reaction of hydrogen oxidation. At 700°C maximum power density reaches about 110 mW/cm^2 using Cr_2O_3+Fe, which is superior to Cr_2O_3+Ag. However, higher propylene selectivity is achieved using Cr_2O_3+Ag and values up to 95% have been achieved under our operating conditions. Carbon deposition poisons the chromium (III) oxide based anode catalysts leading to loss of activity.

References

[1] H. Iwahara, H. Uchida, K. Morimoto, "High-temperature solid electrolyte fuel cells using perovskite-type oxide based on $BaCeO_3$", *Journal of the Electrochemical Society*, 137, 462-465 (1990).

[2] A. Christodoulakis, M. Machli, A.A. Lemonidou, S. Boghosian, "Molecular structure and reactivity of vanadia-based catalysts for propane oxidative dehydrogenation studied by in situ Raman spectroscopy and catalytic activity measurements", *Journal of Catalysis*, 222 (2), 293-306 (2004).

[3] C. Yu, Q. Ge, H. Xu, W. Li, "Development of dehydrogenation of propane to propylene", *Huagong Jinzhan*, 25 (9), 977-982 (2006).

[4] F. Geng, "Technical progress of producing propylene by propane dehydrogenation", *Henan Shiyou*, 19 (5), 70-72 (2005).

[5] R. Grabowski, "Kinetics of oxidative dehydrogenation of C_2-C_3 alkanes on oxide catalysts", *Catalysis Reviews Science and Engineering*, 48 (2), 199-268 (2006).

[6] C. Yu, H. Xu, Q. Ge, W. Li, "Properties of the metallic phase of zinc-doped platinum catalysts for propane dehydrogenation", *Journal of Molecular Catalysis A: Chemical*, 266 (1-2), 80-87 (2007).

[7] C. Yu, Q. Ge, H. Xu, W. Li, "Propane dehydrogenation to propylene over Pt-based catalysts", *Catalysis Letters*, 112 (3-4), 197-201 (2006).

[8] Y. Zhang, Y. Zhou, A. Qiu, Y. Wang, Y. Xu, P. Wu, "Propane dehydrogenation on PtSn/ZSM-5 catalyst: effect of tin as a promoter", *Catalysis Communications*, 7 (11), 860-866 (2006).

[9] P.L. De Cola, R. Glaeser, J. Weitkamp, "Non-oxidative propane dehydrogenation over Pt-Zn-containing zeolites", *Applied Catalysis, A: General*, 306 85-97 (2006).

[10] B. Silberova, M. Fathi, A. Holmen, "Oxidative dehydrogenation of ethane and propane at short contact time", *Applied Catalysis, A: General*, 276 (1-2), 17-28 (2004).

[11] R. Schafer, M. Noack, P. Kolsch, M. Stohr, J. Caro, "Comparison of different catalysts in the membrane-supported dehydrogenation of propane", *Catalysis Today*, 82 (1-4), 15-23 (2003).

[12] S.B. Kogan, M. Herskowitz, "Selective propane dehydrogenation to propylene on novel bimetallic catalysts", *Catalysis Communications*, 2 (5), 179-185 (2001).

[13] http://www.mrw.interscience.wiley.com/emrw/9780471238966/kirk/article/propcala.a01/current/html.

[14] F.E. Frey, R.D. Snow, W.F. Huppke, "Conversion of hydrocarbons", *United States Patent*, No. 2349160 19440516 (1944).

[15] M. Cherian, M.S. Rao, W.T. Yang, J.M. Jehng, "Oxidative dehydrogenation of propane over Cr_2O_3/Al_2O_3 and Cr_2O_3 catalysts: effects of loading, precursor and surface area", *Applied Catalysis A*, 233, 1-33 (2002).

[16] W.K. Jozwiak, W. Ignaczak, D. Dominiak, T.P. Maniecki, "Thermal stability of bulk and silica supported chromium trioxide", *Applied Catalysis A*, 258, 33-45 (2004).

[17] A. Tsyganok, P.J.E. Harlick, A. Sayari, "Non-oxidative conversion of ethane to ethylene over transition metals supported on Mg-Al mixed oxide: Preliminary screening of catalytic activity and coking ability", *Catalysis Communications*, 8, 850-854 (2007).

[18] J.C. Kuriacose, R. Uma, "Chromia as a catalyst", *Metals and Minerals Review*, 9 (11), 36-41 (1970).

[19] Y. Zhang, Y. Zhou, Y. Xu, P. Wu, "Research progress of propane dehydrogenation catalysts", *Huagong Jinzhan*, 24 (7), 729-732 (2005).

[20] S. Wang, K. Murata, "Cr_2O_3 /ZrO_2 catalysts for CO_2 dehydrogenation of ethane to ethylene", *Studies in Surface Science and Catalysis*, 147, 691-696 (2004).

[21] S. Deng, H. Li, Y. Zhang, "Oxidative dehydrogenation of ethane with carbon dioxide to ethylene over nanosized Cr_2O_3 catalysts", *Cuihua Xuebao*, 24 (10), 744-750 (2003).

[22] H. Xie, Y. Tan, "Study of higher olefin synthesis from propane and carbon dioxide on supported Cr_2O_3 catalysts", *Meitan Zhuanhua*, 25 (1), 87-90 (2002).

[23] B.M. Weckhuysen, R.A. Schoonheydt, "Alkane dehydrogenation over supported chromium oxide catalysts", *Catalysis Today*, 51, 223-232 (1999).

[24] Q. Wang, Z. Huang, S. Liu, R. Wang, "Formation and properties of SiO_2-ZrO_2-Al_2O_3- Cr_2O_3 coatings on stainless steel substrates by sol - gel process", *Taoci (Xianyang, China)*, 1, 16-18 (2006).

[25] H. Cao, X. Qiu, Y. Liang, M. Zhao, Q. Zhu, "Sol - gel synthesis and photoluminescence of p-type semiconductor Cr_2O_3 nanowires", *Applied Physics Letters*, 88 (24), 24111211-24111213 (2006).

[26] J. Onyenekwe, W. Delouis, R. Oki, B.G. Shpeizer, A. Clearfield, "Synthesis of mixed chromium zirconium oxides and titanium-chromium oxides", *Abstracts of Papers, 231st ACS National Meeting*, Atlanta, GA, United States, March 26-30 (2006).

[27] H. Li, Y. Yue, C. Miao, Z. Xie, W. Hua, Z. Gao, "Preparation of highly active Cr_2O_3 -SiO_2 catalyst by sol - gel method for ethylbenzene dehydrogenation in the presence of CO_2", *Cuihua Xuebao*, 27 (1), 4-6 (2006).

[28] Y. Huang, M. Liu, Y. Zeng, C. Li, "The effect of secondary phases on electrical properties of ZnO-based ceramic films prepared by a sol - gel method", *Journal of Materials Science: Materials in Electronics*, 15 (8), 549-553 (2004).

[29] S.Y. Chu, T.M. Yan, S.L. Chen, "Characteristics of sol - gel synthesis of ZnO-based powders", *Journal of Materials Science Letters*, 19 (4), 349-352 (2000).

[30] A.B. Hart, G.J. Womack, *Fuel Cells: Theory and Application*, Publisher: Chapman and Hall, London, pp. 72-124 (1967).

[31] C. Berger, *Handbook of Fuel Cell Technology*, Publisher: Prentice-Hall, Englewood Cliffs, N. J., pp. 168-195 (1968).

[32] S.C. Singhal, K. Kendall, *High Temperature Solid Oxide Fuel Cells: Fundamentals, Design and Applications*, Publisher: Elsevier Ltd., Oxford, UK, pp. 205-276 (2003).

[33] F. Zhao, A.V. Virkar, "Dependence of polarization in anode-supported solid oxide fuel cells on various cell parameters", *Journal of Power Sources*, 141 (1), 79-95 (2005).

[34] T. Hibino, A. Hashimoto, M. Suzuki and M. Sano, "A solid oxide fuel cell using Y-doped $BaCeO_3$ with Pd-loaded FeO anode and $Ba_{0.5}Pr_{0.5}CoO_3$ cathode at low temperatures", *Journal of Electrochemical Society*, 149, A1503-A1507 (2002).

CHAPTER 6

CARBON DEPOSITION DURING PROPANE DEHYDROGENATION IN A FUEL CELL

6.1 Introduction

Propane can be selectively dehydrogenated to propylene in a proton-conducting fuel cell [1,2,3]. The unique advantages associated with this process attracted some researchers to investigate the feasibility of this process by conducting experiments [4,5,6]. However, no technology investigated to date has been successfully applied. The Fuel Cells Group at the University of Alberta has been developing fuel cells for highly selective dehydrogenation of light alkanes, including an intense effort to selectively convert propane. Early low temperature models using H_3PO_4-doped PBI polymer as a proton conductor in C_3H_8-O_2 fuel cells operating at 200-250°C showed that formation of very stable intermediate species on the surface of noble metal catalysts blocked propylene production, and very small and unsustainable current flows were obtained [3]. It was recognized that high temperature systems were required to promote desorption of hydrocarbon products from the anode and to provide a higher rate of reaction. Success has been made recently to realize this process based on high temperature proton-conducting solid oxide fuel cells [1,2,7,8]. High temperatures increased the reaction rate of propane dehydrogenation, the process was highly selective to propylene, and enhanced levels of fuel cell power were generated, as described in Chapter 5. Although operating

temperatures (600-700°C) of the solid oxide fuel cell were advantageous to the kinetics of propane dehydrogenation, carbon deposition during the process became a problem at these temperatures. The carbon poisoned the anode catalysts leading to reduction of catalytic activity, which affected both fuel cell performance and gas product distribution.

In this study, the conditions and processes leading to carbon deposition during propane dehydrogenation in the high temperature solid oxide fuel cell were investigated, to develop ways to either avoid the problem or minimize the rate of carbon deposition so as to extend the cell lifetime to economically acceptable levels.

6.2 Experimental

6.2.1 Fuel cell system

The vertical fuel cell set-up with a glass sealant was adopted to ensure good anode side gas seal [9], as shown in Figure 4-12. All the fuel cell experiments were carried out in the temperature range of 600-700°C. After the cell had stabilized at the operating temperature, the anode feed was switched to pure C_3H_8 (Praxair, grade 2.0). O_2 (Praxair, grade 2.6) was supplied to the cathode side as oxidant via the inner tube. The gas flow rates were carefully controlled with mass flow controllers.

6.2.2 Electrolyte

15%Y-doped $BaCeO_3$ (BCY15) was used as the proton-conducting electrolyte. The preparation procedure was described in Chapter 3. Y-doped $BaCeO_3$ powder was prepared by solid-state reactions, and then solid electrolyte disks were made by pressing the powder.

6.2.3 Electrodes

Commercial platinum paste (Heraeus CL11-5100) and synthesized Cr_2O_3+Ag paste were adopted as anode catalysts. The cathode was fixed to platinum paste. Two kinds of chromium oxide based anode catalysts were prepared for testing: (1) Cr_2O_3+Ag (50:50) and (2) Cr_2O_3+Ag (50:50) modified by addition of 0.5% (w.t.%) potassium through pre-treating Cr_2O_3+Ag with potassium hydroxide solution. For comparison purposes, a platinum anode catalyst supported on silver was also prepared. A typical impregnation-reduction method was employed to prepare Ag-supported Pt catalyst using formaldehyde as a reducing agent. To synthesize Pt/ Ag with the Pt loading of 4.0 wt.%, 2.4g of Ag was uniformly dispersed in 44 mL of an aqueous solution of H_2PtCl_6 (3.7g/L) by ultrasound. Then 40 mL of the formaldehyde was added dropwise slowly into the H_2PtCl_6 solution at 40°C and 0.8 mL of H_2O_2 (30v/o) was added to stabilize the Pt particles under continuous stirring for 4 h. The solid product was rinsed repeatedly with deionized water and filtered. Finally, the product was dried at 60°C for 8 h in a fume hood.

Both the anode and cathode were prepared by screen-printing corresponding pastes onto the surfaces of the BCY15 electrolyte disk, and then were dried in air at 120°C for 30 min to remove the organic binder and to increase adhesion to the electrolyte.

6.2.4 Characterization of the anode catalysts

The microstructure of the anode catalysts was examined using a Hitachi S-2700 scanning electron microscope. Carbon deposition on anode catalysts was characterized using XPS and EDX analysis. Before analysis by XPS or EDX, the sample of used anode

catalyst was treated in Ar at 400°C for 10 h to remove propane and other hydrocarbon moieties adsorbed on the anode. The definition of carbon selectivity was given in Chapter 3.

6.3 Results and discussion

6.3.1 Carbon deposition under open circuit conditions

Under the open circuit conditions the reactions taking place in the fuel cell chamber were mainly thermal cracking of propane and some additional catalytic reactions occurring at the anode (Figure 6-1). The gas components (CH_4, C_2H_4, C_2H_6, C_3H_6) arising from the thermal reactions [1,2] are thermodynamically favoured to form carbon on the anode catalyst in an irreversible process (Figure 4-2). The thermodynamic bias to carbon deposition was very strong, especially at high temperatures, for propane, propylene and ethylene, and favored carbon deposition during propane dehydrogenation in the fuel cell at the operating temperatures (600-700°C). However, the rate of carbon formation was determined by the operating conditions and catalysts. Figure 6-2 shows the carbon deposition from thermal cracking reactions in the fuel cell chamber with pure propane as feed. The carbon selectivity from thermal cracking of propane was dependent on the operating temperature and propane flow rate, i.e. reaction time. While decreasing the operating temperature and reaction time diminishes carbon formation, the yield of propylene was also compromised because low temperatures are kinetically unfavorable and so short reaction time causes low propane conversion. Generally the thermal reactions occurring in the hollow tube set-up (Figure 6-1) make no significant contribution to carbon deposition on the catalyst but deteriorate gas products distribution,

thus decreasing propylene selectivity. The mechanism of carbon formation from propane during thermal pyrolysis is through free radicals, which was well described in ref. 10. Thus it was necessary to minimize the carbon deposition caused by thermal reactions through optimizing fuel cell set-up design.

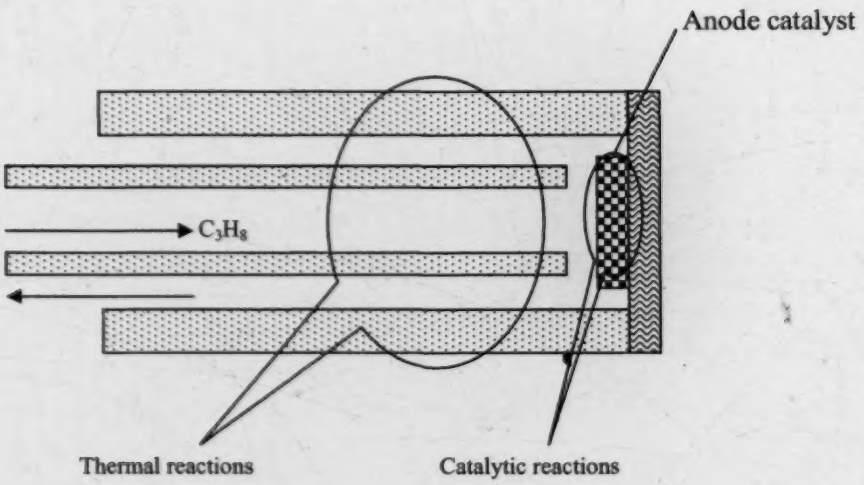

Figure 6-1. Different reaction zones in the anode chamber of fuel cell under open circuit conditions.

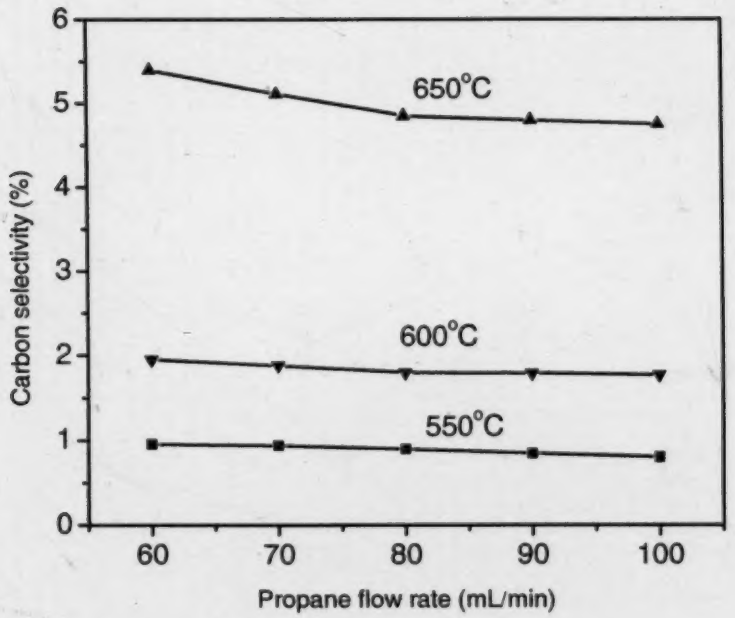

Figure 6-2. Carbon selectivity from thermal cracking of propane in the fuel cell chamber.

The behaviours leading to carbon deposition on the anode catalysts were investigated at 650°C with propane flow rate of 60 mL/min under open circuit conditions. Figure 6-3 shows the XPS analysis of carbon on the Cr_2O_3 based anode surfaces after testing in the fuel cell for 10 h. For comparison, Cr_2O_3+Ag anode catalyst and Cr_2O_3+Ag modified by addition of 0.5% potassium were also analyzed. It was found that carbon deposition occurred on both types of anode surface, but much more carbon was formed on the unmodified anode catalyst Cr_2O_3+Ag. The difference is due to the addition of potassium to the catalyst that modified the surface of chromium (III) oxide. It has been shown [11,12,13,14,15,16,17] that the catalytic properties of chromium-based catalysts for dehydrogenation are due to surface Cr^{III} species, and addition of potassium could

decrease the surface density of Cr^{III} by formation of Cr^{VI} containing compounds (K_2CrO_4 or $K_2Cr_2O_7$ species). So the addition of potassium decreased the activity of chromium-based catalyst, i.e. the surface acidity, especially for the sites with strong acidity, which tend to cause carbon deposition during the reaction. Our results are consistent with those studies.

P. Biloen et al [18] found that the small-particle-size and well-dispersed platinum enhanced propylene selectivity through investigating the catalytic mechanism of propane dehydrogenation on platinum, and single atoms of platinum were proposed as accounting for propane dehydrogenation. The high propylene selectivity on small-particle-size and well-dispersed platinum was due to inhibition of side reactions, such as carbon deposition. The comparison was made on the two different platinum-particle-size anode catalysts, as shown in Figure 6-4 and Figure 6-5. The advantage of synthesized small platinum particle sizes was reflected in the better propylene selectivity during operation at fuel cell operating conditions. For example, the propylene selectivity on the commercial platinum paste was about 70-80% at 600°C with propane flow rate of 10 $mL.min^{-1}$, but for the synthesized Ag-supported Pt catalyst, the propylene selectivity was above 80% at the same operating conditions. These data indicated that the higher propylene selectivity was due to the small-particle-size and well-dispersed platinum, and the results obtained from the electrochemical propane dehydrogenation in the fuel cell were consistent with an electrochemical propane dehydrogenation process. So use of small-particle-size and well-dispersed platinum could suppress the carbon deposition and other side reactions, with the consequence of increasing propylene selectivity during the process of propane dehydrogenation in the fuel cell. However, at high temperatures the small platinum

particles would aggregate to form larger particles, which would lead to loss of the advantages of inhibition of carbon deposition and increased propylene selectivity.

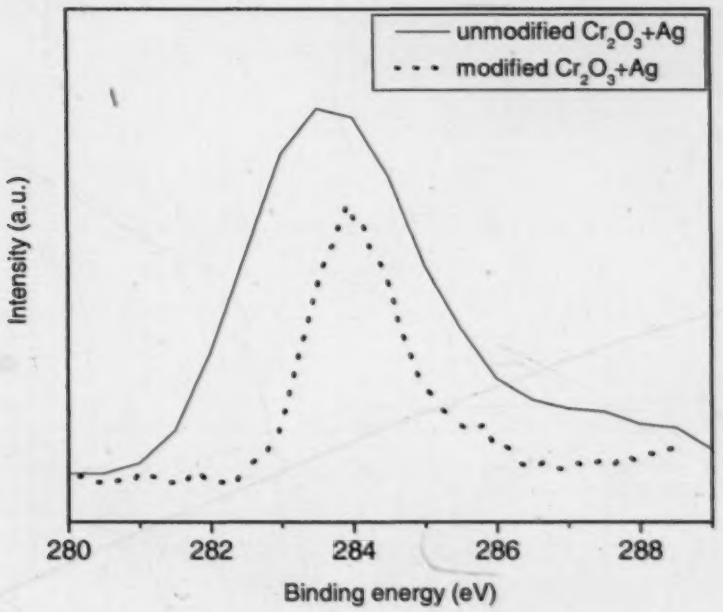

Figure 6-3. Comparison of binding energy peak of C1s for different catalysts after 10 h fuel cell operation.

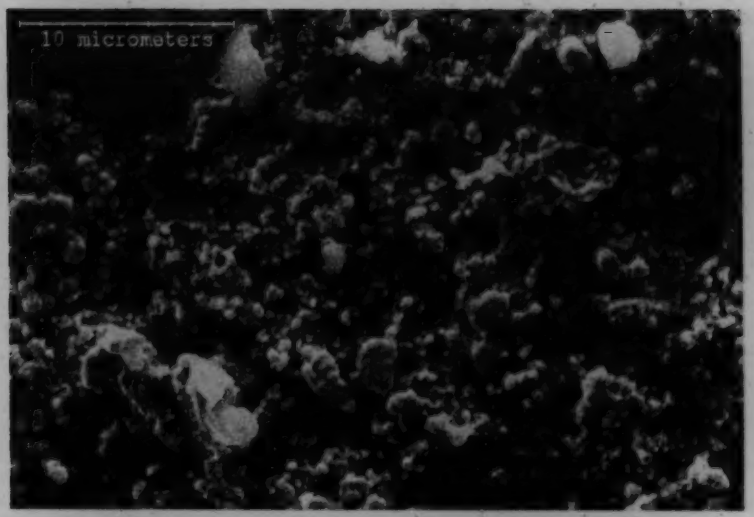

Figure 6-4. Microstructure of commercial platinum paste (Heraeus CL11-5100).

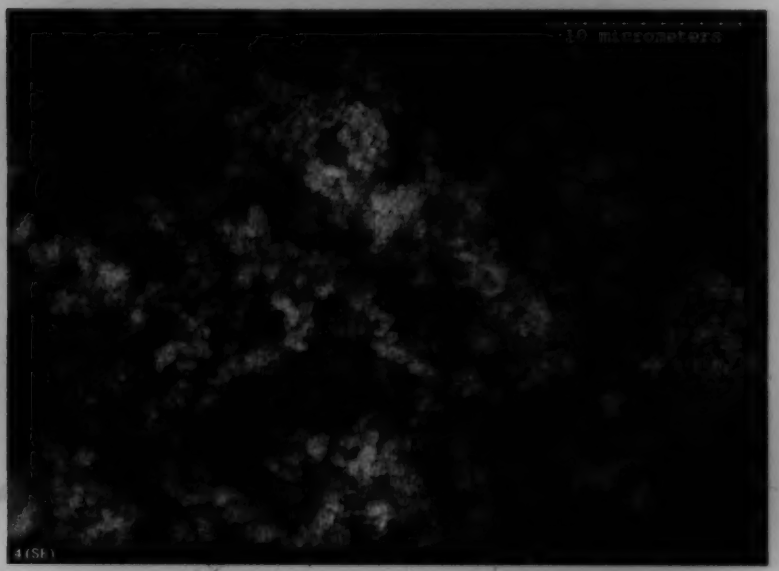

Figure 6-5. Microstructure of synthesized platinum anode catalyst supported on silver.

6.3.2 Carbon deposition under fuel cell operation conditions

During the current flow conditions, the reaction process on the anode catalyst was completely changed from chemical to electrochemical and thus the intermediate species formed on the catalyst surface readily reacted further to form products and generate power. Compared to the open circuit condition, much less carbon formation was detected on the chromium(III) oxide-based anode catalysts under the operating conditions by XPS technique (Figure 6-6), which was confirmed by EDX analysis (Figure 6-7). For the fuel cell continuously running at 650°C for 10 h with a 50 mA current flow, the amount of carbon deposition on the anode catalyst Cr_2O_3+Ag was below 5% mass concentration in the catalyst, which corresponded to about 0.2% carbon selectivity based on the mass balance and carbon atom balance of inlet and outlet gas. The same phenomena were found for use of the platinum catalyst, which also exhibited much inhibited carbon deposition during discharging of the fuel cell (closed circuit). The carbon deposition behaviors at different discharging currents were also monitored at the propane flow rate of 50 $mL.min^{-1}$ and operating temperature of 600°C (Figure 6-8). Compared to open circuit conditions (i.e. zero current), the selectivity to carbon dropped steadily with increasing current. Thus, operating the fuel cell under current flowing conditions clearly reduced the rate of carbon formation. This phenomenon may be due to the presence of electron on the anode catalyst under current flow conditions. The electrons on the anode catalyst formed a local electrical field which affected the reaction mechanism of propane dehydrogenation, and enabled the gas products, propylene and small amounts of other by-products, to be easily desorbed before they could be further dehydrogenated to form carbon. In contrast, during the process of catalytic propane dehydrogenation the gas

species of propylene or other intermediate were difficult to desorb and contributed to carbon deposition [3,19,20,21,22,23]. Because there are no other publications available on the propane dehydrogenation process in a proton-conducting fuel cell, the details of carbon deposition mechanism during this process are not yet fully understood and further study is required.

However, there was no obvious difference in carbon deposition found between the modified and unmodified chromium (III) oxide catalysts under the current flowing conditions. The similarity may be due to the following reason. The surface chemistry of chromium oxide, such as the ratio of Cr^{VI}/Cr^{III}), was influenced by the local electrical field over the anode catalyst under the current flowing conditions. This process probably was similar to the effect of addition of potassium to chromium oxide, which reduced the strength of acid sites, thus accounting for carbon deposition. However, the effect of potassium was less pronounced when compared to the local electrical field, and thus any effect of potassium on carbon deposition was unnoticeable under the current flow conditions. As a consequence, the two anode catalysts showed very similar ability to resist carbon deposition.

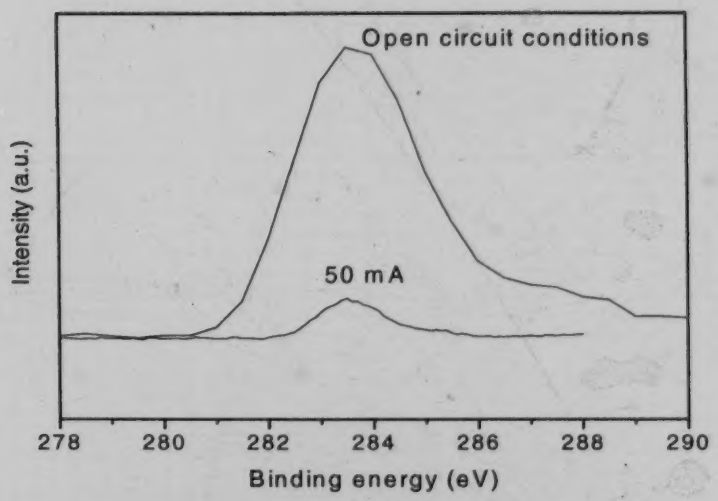

Figure 6-6. Comparison of binding energy peaks for C1s of carbon deposited on catalysts used under open circuit condition and at discharging current of 50 mA during 10 h fuel cell tests.

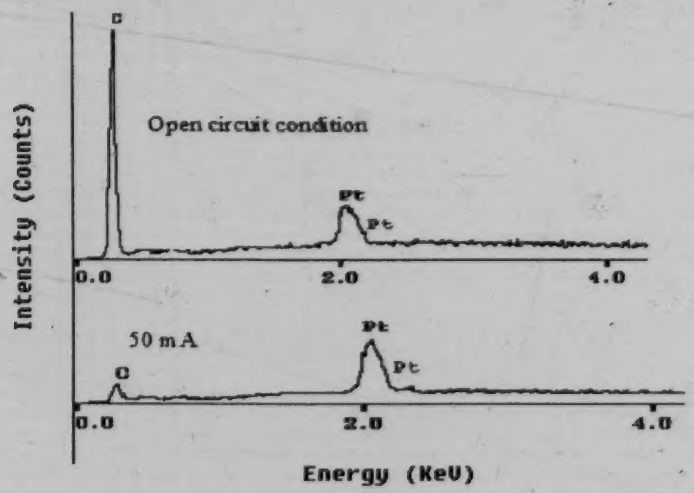

Figure 6-7. EDX analyses comparing carbon deposition on anode catalyst Cr_2O_3+Ag under open circuit condition and at a current of 50 mA during 10 h fuel cell tests.

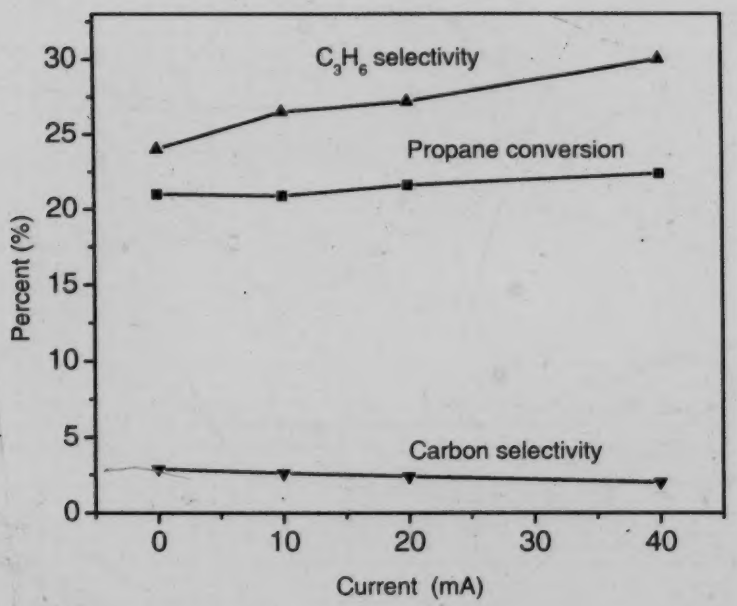

Figure 6-8. Propane conversion and selectivities of carbon and propylene as a function of current density (600°C, propane flow rate: 50 mL/min).

6.4 Conclusions

Carbon deposition caused by thermal reactions occurring in fuel cells is thermodynamically favorable and it deleteriously affects the gas product distribution. The carbon formed on the anode due to catalytic or electrochemical reactions poisons the catalysts, leading to the loss of their activity for dehydrogenation. Under current flow conditions, by activating electrochemical reaction of propane dehydrogenation the presence of a local electrical field on the anode catalyst can suppress the carbon deposition process, in contrast to the catalytic reactions under open circuit conditions. As a result, when current is flowing in the fuel cell there is dramatic inhibition of carbon deposition on the anode catalyst compared to open circuit conditions.

References

[1] Y. Feng, J. Luo, S. Wang, J. Melnik, K.T. Chuang, "Investigation of Y-doped $BaCeO_3$ as electrolyte in propane fueled proton conducting solid oxide fuel cell", *Proceedings of the International Symposium on Fuel Cell and Hydrogen Technologies*, Editor: D. Ghosh, Calgary, Canada, Aug. 21-24, pp. 461-471 (2005).

[2] Y. Feng, J. Luo, K.T. Chuang, "Conversion of propane to propylene in a proton-conducting solid oxide fuel cell", *Fuel*, 86, 123-128 (2007).

[3] C.K. Cheng, "Application of PBI membrane polymer fuel cell for conversion of hydrocarbon", *Masters Thesis*, University of Alberta, pp.120-129 (2004).

[4] J.H. White, M. Schwartz, A.F. Sammells, "Solid state proton and electron mediating membrane and use in catalytic membrane reactors", *United States Patent*, No. 6,281,403 B1, 28 Aug. 2001.

[5] W.G. Barker, B.S. Berland, M. Schwaartz, L. Simpson, J. Armstrong, "Apparatus and method for the design and manufacture of thin-film electrochemical devices", *United States Patent*, No. 6,772,501 B2, 10 Aug. 2004.

[6] D.J. Edllund, D.T. Friesen, "Hydrogen-permeable composite metal membrane and uses thereof", *United States Patent*, No.5, 217,506, 08 Jun. 1993.

[7] Y. Feng, J. Luo, K.T. Chuang. "A method to measure the proton conductivity of $LiNaSO_4$ under fuel cell conditions", *Journal of the Electrochemical Society*, 153(6), A1049-A1052 (2006).

[8] Y. Feng, J. Luo, K.T. Chuang, "Chemical Stability of $LiNaSO_4$ Electrolyte during Operation in a H_2-O_2 Fuel Cell", *Journal of the Electrochemical Society*, 153 (5), A865-A868 (2006).

[9] Y. Feng, J. Luo, K.T. Chuang, "Analysis and improvement of chemical stability of Y-doped $BaCeO_3$ as proton conducting electrolytes in C_3H_8 - O_2 fuel cells", *Journal of New Materials for Electrochemical Systems*, 10(3), 147-152 (2007).

[10] F.O. Rice, K.K. Rice, "The Aliphatic Free Radicals, Baltimore", Johns Hopkins Press, p. 92-94, 1935.

[11] E. Rombi, M.G. Cutrufello, V. Solinas, S.D. Rossi, G. Ferraris, A. Pistone, "Effects of potassium addition on the acidity and reducibility of chromia/alumina dehydrogenation catalysts", Applied Catalysis A, 251 (2003) 255-266.

[12] H.A. Mcveigh, "Kinetics of carbon on chromia-alumina catalysts during dehydrogenation reactions", *Ph.D. Dissertation*, University of Delaware, (1972) 200-250.

[13] I. Dybkjaer, A. Bjorkman, "Carbon deposition on catalysts during conversion of oxygenated organic compounds", *Advances in Chemistry Series*, 109 (1972) 219-222.

[14] P. Michorczyk, J. Ogonowski, D. Ralowicz, "Dehydrogenation of propane over chromium -based catalysts", *NATO Science Series, II: Mathematics, Physics and Chemistry*, 191, 339-343 (2005).

[15] H. Zou, X. Ge, M.S. Li, R.C. Shangguan, J.Y. Shen, "Dehydrogenation of propane over CrO_x/SiO_2 catalysts under CO_2 atmosphere", *Wuji Huaxue Xuebao*, 16(5), 775-782 (2000).

[16] J.A. Pena, A. Monzon, J. Santamaria, "Deactivation by coke of a chromium(III) oxide /alumina catalyst during butene dehydrogenation", *Journal of Catalysis*, 142(1), 59-69 (1993).

[17] X. Ge, M. Zhu, J. Shen, "Catalytic performance of silica-supported chromium oxide catalysts in ethane dehydrogenation with carbon dioxide", *Reaction Kinetics and Catalysis Letters*, 77(1), 103-108 (2002).

[18] P. Biloen, F.M. Dautzenberg, W.M. Sachtler, "Catalytic dehydrogenation of propane to propene over platinum and platinum-gold alloys", *Jounal of Catalysis*, 50, 77-86 (1977).

[19] P.L. De Cola, R. Glaeser, J. Weitkamp, "Non-oxidative propane dehydrogenation over Pt-Zn-containing zeolites", *Applied Catalysis, A: General*, 306 85-97(2006).

[20] P.C. Redfern, P. Zapol, M. Sternberg, S.P. Adiga, S.A. Zygmunt, L.A. Curtiss, "Quantum chemical study of mechanisms for oxidative dehydrogenation of propane on vanadium oxide", *Journal of Physical Chemistry B*, 110(16), 8363-8371 (2006).

[21] H. You, "Kinetics of propane oxidative dehydrogenation to propylene", *Petroleum Science and Technology*, 23(11-12), 1441-1452 (2005).

[22] T.X. You, H.J. You, "Advances in the reaction kinetics of propane dehydrogenation oxidation to propene", *Tianranqi Huagong*, 29(6), 51-56 (2004).

[23] C.J. Dillon, J.H. Holles, M.E. Davis, J.A. Labinger, "Heteropolyacid-based catalysts for selective alkane oxidation: mechanism of formation of maleic anhydride from propane", *Catalysis Today*, 81(2), 189-195 (2003).

CHAPTER 7

SUMMARY

7.1 General conclusions

1. A novel electrochemical process for propane dehydrogenation in a proton-conducting fuel cell co-generates the value-added product propylene and electricity, through development of suitable fuel cell components of electrolyte, anode catalyst and cathode catalyst as well as the fuel cell set-up. High selectivity to propylene and high fuel cell performances were obtained simultaneously during the electrochemical process of propane dehydrogenation in the proton-conducting fuel cell.
2. 15% Y-doped $BaCeO_3$ was synthesized by solid state reaction is an effective proton-conducting electrolyte in the fuel cell for propane dehydrogenation, as it was chemically stable and showed very high proton conductivity during operating temperatures 600-700°C. After intense investigation of the chemical stability of Y-doped $BaCeO_3$ under the fuel cell conditions, and by improving and redesigning the fuel cell set-up, it was shown that this protonic electrolyte has very good stability during a 120 h continuous test. This kind of material is a good candidate for use as the electrolyte in the fuel cell for propane dehydrogenation..
3. A new fuel cell set-up design coupled with application of a new kind of glass sealant solves the problem of diffusion of air through the ceramic sealants, and thus prevents the formation of carbon oxide near the surface of the electrolyte Y-doped $BaCeO_3$ in

the anode chamber, which deteriorates the stability of electrolyte as well as the fuel cell performance.

4. The solid sulphate $LiNaSO_4$ shows very high conductivity under the fuel cell operating conditions, but the portion of proton conductivity in the total conductivity is very small. Chemical stability tests showed that the conductivity and fuel cell performance of $LiNaSO_4$ degrade when using $LiNaSO_4$ as electrolyte for propane dehydrogenation due to its reduction by the hydrogen-containing atmosphere. Thus solid sulphate $LiNaSO_4$ is unsuitable as the electrolyte in a fuel cell for propane dehydrogenation.
5. A new method for measuring the proton conductivity of hydrogen-reducible materials, like $LiNaSO_4$, solves the limitation of traditional hydrogen concentration method, which cannot be applied for measurements of hydrogen-reducible materials. The proton conductivity of $LiNaSO_4$ determined using this method was consistent with the fuel cell test results.
6. Commercial platinum paste is an effective catalyst for anode and cathode in a fuel cell for propane dehydrogenation. It has good activity of electrochemical propane dehydrogenation and provides high selectivity to propylene as well as high fuel cell performance.
7. Cr_2O_3 based anode catalysts synthesized by sol-gel method show even higher activity for propane dehydrogenation in the proton-conducting fuel cell than commercial platinum paste. The propylene selectivity is up to 95%, and the maximum power density attainable to date is about 110 mW/cm^2 for a fuel cell using the Cr_2O_3 based anode catalyst.

8. Metal particles of Fe or Ag in composite anode catalysts comprising the metals and Cr_2O_3 not only serve as electronic conductors, but also influence propylene selectivity and fuel cell performances through activation of the catalyst toward electrochemical reactions during the process of propane dehydrogenation in the fuel cell. Relatively higher propylene selectivity is obtained using the anode Cr_2O_3+Ag, and even better fuel cell performance is achieved when using Cr_2O_3+Fe.
9. Gas phase species such as H_2 and C_2H_6 produced by thermal reactions in the fuel cell system are involved in the overall process of propane dehydrogenation in the fuel cell by side electrochemical reactions. Hydrogen oxidation is the predominant side electrochemical reaction, which competes with the desired electrochemical reaction of propane dehydrogenation.
10. The open circuit voltage of the fuel cell is the mixed voltage of propane dehydrogenation reaction and other side electrochemical reactions. All these electrochemical reactions contribute to the fuel cell performance, and the proportion of contribution of each reaction to gas product distribution and fuel cell performances is dependent on fuel cell operating conditions as well as the anode catalysts.
11. Carbon deposition during the process of propane dehydrogenation in the fuel cell not only deteriorates the gas product distribution but also poisons the anode catalyst leading to loss of activity. The amounts of carbon deposited on the anode catalysts are much less under the current flow conditions in contrast to open circuit conditions, due to the presence of electrons on the anode surface which form a local electrical field influencing the carbon deposition behaviour.

7.2 Claim for original research

1. The feasibility of propane dehydrogenation in a proton-conducting fuel cell to co-generate propylene and electricity simultaneously was experimentally proven.
2. Suitable protonic electrolyte with high proton conductivity and high stability in the fuel cell for propane dehydrogenation was developed and a new fuel cell set-up was designed to comply with application of the protonic electrolyte Y-doped $BaCeO_3$.
3. A new method was developed to measure the proton conductivity of hydrogen reducible materials for use as protonic electrolyte under the fuel cell conditions, and this method can be extended to measurements of proton conductivity of mixed conductive electrolytes under the "real" fuel cell conditions.
4. Chromium (III) oxide based anode catalysts were developed for use in the fuel cell for application of propane dehydrogenation with high electro-catalytic activity and high selectivity to propylene.
5. The reaction process of propane dehydrogenation in a proton-conducting fuel cell was revealed and the side electrochemical reactions were identified. The knowledge accumulated from the studies has advanced our understanding from "how" to "why" gas products distribution and fuel cell performances were influenced by operating temperatures, propane flow rates and anode catalysts.
6. The identification of different carbon deposition behaviours under different operating conditions provides guidance for how to suppress carbon deposition and thus improve gas products distribution, and for controlling carbon deposition during industrial chemical process of propane dehydrogenation.

7.3 Prospect of future work

I hope that this pioneer work is interesting to the followers. Should that be the case, I would like to recommend:

1. Anode supported thin electrolyte membranes need to be developed to increase the triple phase boundary area and thus increase propane conversion rates, and to reduce the ohmic resistance due to electrolyte conduction and thus increase fuel cell performance and power density.
2. Long-term carbon resistant anode catalysts with high electro-catalytic activity for propane activation and high selectivity to propylene need to be developed. Preliminary test showed that fine-particle of platinum anode catalyst with well dispersion had good resistance to carbon formation and showed very high selectivity to propylene, but the aggregation of such fine particles at high temperatures is a substantial limitation for application of this kind of anode catalyst for long term of fuel cell running. Some strategies to prevent this aggregation of platinum fine particles need to be developed. A possible suggestion is introducing tin into the platinum based anode catalysts, which metal showed effectiveness to prevent platinum particle aggregation under the chemical reaction of propane dehydrogenation. So it is necessary to evaluate tin or other metals with similar functions under the electrochemical conditions in the fuel cell. In addition, even smaller size particles of platinum with well dispersion are worthy to develop by employing some new technologies (e.g. nanotechnology) or methods.

3. Long-term stability of the whole fuel cell systems, including individual fuel cell components as well as the compatibility between each other, needs be further investigated. Although lots of work was done on the stability test of the proton-conducting electrolyte as well as anode catalysts, stability for the whole fuel cell system, especially for long-term run necessarily require more study. This situation is much more worthy to bring to attention when introducing some new fuel cell components into the current cell system.
4. More work needs be done on the mechanism of electrochemical propane dehydrogenation in the fuel cell to better understand this process and provide guidance for improvement of such a process. The current work described in Chapter 4 and Chapter 6 is attempting to illustrate the electrochemical reaction process from the aspects of open circuit voltage, fuel cell performance, gas products analysis, and anode catalysts characterization. Although the side electrochemical reactions were identified, the details of the reaction steps of propane dehydrogenation on anode catalysts are not clear, as well as the questions: (1) how do the side electrochemical reactions compete with electrochemical propane dehydrogenation? (2) What is the influence of different anode catalysts on the reaction mechanism? The answers to these questions will provide substantial useful information for anode catalysts design and improvement, and thereby increase propylene selectivity and decrease carbon formation as well as other side electrochemical reactions.

APPENDIX-A

The calibration of hydrogen was conducted with argon as carrier gas, and the following graph shows the relationship of the hydrogen concentration in the standard gas mixtures with the corresponding hydrogen peak areas detected by GC. Under the low hydrogen concentration (< 8.0%) range, the relationship is approximately linear. Because under our fuel cell operating conditions the concentration of hydrogen, which was produced by propane thermal cracking, is low, the hydrogen concentration range (0-8.0%) for calibration is sufficient to determine the hydrogen concentration in experiments. Our experimental results showed during the operating temperatures (600–700°C), the hydrogen concentration mostly lies within this range.

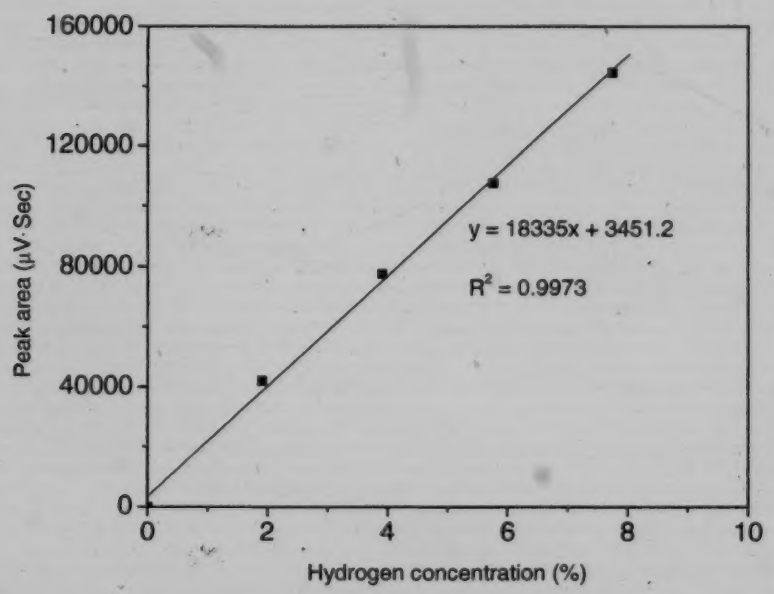

Figure I Relationship of standard hydrogen concentration with corresponding GC peak area.

In addition, the concentrations of standard gas components for calibration were listed as the following Table I.

Table I Concentrations of standard gas components

	Concentrations (%)			
	# 1	# 2	# 3	# 4
Hydrogen	1.9	3.9	5.8	7.8
Methane	8.2	14.4	19.2	22.3
Ethylene	0.9	4.8	4.2	5.2
Ethane	4.5	9.6	13.6	18.1
Propylene	5.8	19.3	22.1	29.3
Propane	78.7	48	35.1	17.3

APPENDIX-B

For anode reaction:

$$C_3H_8 \rightarrow C_3H_6 + 2H^+ + 2e^-$$

from Faraday's law, if one mole of propylene is produced and simultaneously there will be 2 mole electrons produced as well.

Assuming:

V = inlet propane volumetric flow rate (STP)

T = Standard temperature (298.15 K)

P = Standard Pressure (1 bar)

$Y_{propylene}$ = propylene yield obtained from the electro-catalytic dehydrogenation (anode reaction)

The inlet of propane molar flow rate (n) can be calculated from Peng-Robinson Equation

$$P = \frac{R*T}{v-b} - \frac{a*\alpha(T)}{v*(v+b)+b*(v-b)}$$

where

$v = V/n$;

$$a = 0.45724 * \frac{R^2 * T_c^2}{P_c}$$

$$b = 0.07780 * \frac{R*T_c}{P_c}$$

$$\alpha(T) = [1 + m * (1 - T_r^{1/2})]^2$$

$$m = 0.37464 + 1.54226 * \omega - 0.26992 * \omega^2$$

In this equation T_c and P_c represent the critical temperature and critical pressure, and ω represents acentric factor. For propane the value of these parameters are as following:

$T_c = 369.70$ K

$P_c = 4.25$ mPa

$\omega = 0.153$

So for the given inlet propane volumetric flow rate V, The inlet of propane molar flow rate n can be easily calculated from Peng-Robinson Equation and n is proportional to V:

$$V \propto n \qquad (1)$$

From the definition of propylene yield,

$$Y_{propylene} = \frac{n_{propylene}}{n} \qquad (2)$$

where

$n_{propylene}$ = molar flow rate of produced propylene

From Faraday's law, the current I achieved during the process is:

$I = 2 * n_{propylene} * 96485$

So the current density i is:

$$i = \frac{I}{S} = \frac{2 * n_{propylene} * 96485}{S} \qquad (3)$$

where

S= effective anode area (in experiment S = 0.7 cm^2)

Combining equation (2) and (3), we can get:

$$Y_{propylene} = \frac{S}{2 * n * 96485} * i$$

So for a given inlet propane molar flow rate n, $Y_{propylene}$ is proportional to i, and note equation (1) we can see that for a specific inlet propane volumetric flow rate V (in experiment V = 10 mL/min), the relationship between $Y_{propylene}$ and i is also linear.

Note: when doing calculation all the units of parameters were converted to SI units.